ALMA MATER STUDIORUM · UNIVERSITÀ DI BOLOGNA

Scuola di Scienze
Dipartimento di Fisica e Astronomia
Corso di Laurea Magistrale in Fisica

NIO1 negative ion beam investigation in view of ITER heating and current drive

Relatore: Presentata da:

Prof. Mauro Bruno   Margherita Ugoletti

Correlatori:

Dott. Gianluigi Serianni
Dott. Pierluigi Veltri

Anno Accademico 2016/2017

Sommario

Negli ultimi decenni, la ricerca e lo sviluppo di nuove fonti di energia sono state oggetto di crescente interesse scientifico. In particolare, la fusione nucleare potrebbe essere la soluzione al problema energetico mondiale.

ITER è attualmente il più grande esperimento di fusione nucleare in via di costruzione. Situato nel sud della Francia, sarà il più grande *tokamak* costruito al mondo con l'obiettivo di produrre 500 MW di potenza dai 50 MW di potenza fornitagli. Diversi metodi di riscaldamento del plasma sono in via di sviluppo per poter scaldare il *core* del plasma a temperature dell'ordine dei 15 keV. Tra questi, l'iniezione di fasci neutri è uno dei più importanti. Il progetto PRIMA, costituito dagli esperimenti SPIDER e MITICA in via di costruzione al Consorzio RFX a Padova, si pone come obiettivo lo studio dei futuri iniettori di fasci neutri di ITER.

L'esperimento NIO1, anch'esso situato al Consorzio RFX, è una relativamente piccola sorgente a radio frequenza RF di ioni negativi, nato con l'obiettivo di caratterizzare la fisica delle sorgenti di ioni nell'ottica dei futuri utilizzi negli iniettori di fasci neutri, quali lo stesso MITICA.

Questo lavoro di tesi, nato da una collaborazione tra i Laboratori Nazionali di Legnaro (LNL) e il Consorzio RFX, caratterizza il fascio di ioni negativi di NIO1. I dati raccolti durante le campagne sperimentali sono stati analizzati e confrontati, per testare le performance della nuova griglia di estrazione installata su NIO1 a maggio 2017. La caratterizzazione è stata fatta in diversi modi: confrontando qualitativamente i dati raccolti dalle varie diagnostiche; ricostruendo tomograficamente l'immagine dei 9 beamlets tramite i dati raccolti dalle telecamere; caratterizzando il plasma formatosi in seguito alla propagazione del fascio nel gas di fondo, tramite il confronto con i dati sperimentali e quelli ottenuti da una simulazione numerica *Particles-In-Cell* PIC.

Abstract

In these last decades, the research and the development of new sources of energy have been the subject of increasing scientific interest. In particular, the nuclear fusion could represent the solution of the world energy issue.

ITER is now the largest nuclear fusion experiment under construction. Located in southern France, it will be the world's largest *tokamak* aiming at producing 500 MW of fusion power from 50 MW of input power. To reach the required performances, various additional heating are under development to heat the plasma core up to 15 keV. Among these, neutral beam injection is one of the most important method. The ITER Neutral Beam Test Facility, called PRIMA, is hosted in Padova at Consorzio RFX, including SPIDER and MITICA experiments.

NIO1, a relatively compact radio frequency RF ion source installed also at Consorzio RFX, is aimed to investigate general issues on ion source physics in view of the full size ITER injector MITICA as well as DEMO relevant solutions.

This work of thesis, developed in a collaboration between INFN Laboratori Nazionali di Legnaro (LNL) and Consorzio RFX, investigates the NIO1 negative ion beam. In particular, the data collected during the experimental campaigns are analyzed and compared, in order to test the performance of the new *extraction grid* installed on NIO1 in May 2017.

The beam characterization has been made in different ways: by qualitatively comparing the data collected in the experimental campaigns by the different diagnostics; by reconstructing by means of computer beam tomography the extracted beam; by characterizing the beam plasma with the comparison between the experimental data and the results of a Particle-In-Cell simulation.

Contents

Introduction

The world energy consumption has grown enormously in the past 90 years, not only because of the population growth but also because of the more energy consuming world life style. To satisfy this thirst of energy, fossil fuel consumption was increasing dramatically, starting a relentless global warming process which is causing the climate to change. In this scenario, renewable energies play a crucial role. Among these, the nuclear fusion is one of the most attractive because of several advantages. At first, it will produce no atmospheric pollution: the fusion reaction produces helium which is an inert gas and no long-lived radioactive waste. It exploits low-cost, abundant fuels available for example from seawater. It exhibits an inherently safe system: even the worst conceivable accident would not have repercussions on the surrounding environment.

ITER, latin word for *the way*, is an international project aiming at realizing a nuclear fusion reactor capable to produce an amount of energy higher than the energy required to be activated. Located in the southern France, it will be the world's largest *tokamak* aiming at producing 500 MW of fusion power from 50 MW of input power and at demonstrating the control of the plasma and the fusion reactions with negligible consequences to the environment. In a tokamak, superimposed magnetic fields confine the plasma by shaping it as a *donut*, with a rotationally symmetry around the vertical axis.

One of the main requirements for achieving fusion is to heat the plasma at very high temperature, in the order of tens of keV. In ITER, three main different heating methods will contribute to plasma heating: the ohmic heating, the radio-frequency heating and the neutral beam heating.

Neutral beam heating is now the most important method for plasma heating in almost all fusion experiments. Accelerated neutral particles when are injected in the plasma vessel are unaffected by the magnetic fields, and travel along straight-line trajectories until they are ionized with the background plasma, with consequently heating of the hit particles.

Neutral beam injections with negative ions NI-NBI, mainly H^-, are much more efficient in producing high energy neutral beams than positive ions, even if their production presents harder issues with respect to the production of positive ions.

The ITER Neutral Beam Test Facility, called PRIMA (Padova Research on ITER Megavolt Accelerator) is hosted in Padova, at Consorzio RFX, and included the two experiments SPIDER and MITICA. Respectively, they aim at developing and testing the full-size ITER negative ion source and the full-size heating neutral beam injectors. In particular, ITER will initially be equipped with two heating neutral beam injectors designed to deliver 33.3 MW of either 1 Mev D or 0.87 Mev H^0 to the ITER plasma for up 3600 s.

In order to investigate the negative ion source and the negative ion beam development, the Negative Ion Optimization phase 1 (NIO1) was installed in 2013-2014 at Consorzio RFX, in collaboration with INFN (LNL). It is a small radio-frequency plasma driven negative ions source. NIO1 goal is the production of an extracted H^- beam of 130 mA and the acceleration of the ions up to an energy of 60 keV. In May 2017, in order to improve the Extraction Grid operation, an upgrade in the magnets configuration was installed. Also the radius of the grid apertures was increased.

This work of thesis aims at characterizing and investigating the negative ion beam extracted and accelerated in NIO1 experiment. In particular, a qualitative comparison between the data collected by the different diagnostics has been made. The principal information have been taken from the currents measured by the acceleration column components and by the carbon fiber composite (CFC) tile, from the Beam Emission Spectroscopy and from the images collected by two cameras. The data collected by the cameras have also been used to reconstruct the beam by means of computer tomography reconstruction.

Finally, two electrostatic probes have been used to characterize the beam plasma, generated as a result of the accelerated negative ions interaction with the background gas: a Langmuir and a Retarding Field Energy Analyzer (RFEA) probes. The information about ionic and electronic density and temperature, collected by these probe, has been compared with the results of a Particle-In-Cell (PIC) simulation. The PIC code is implemented in a C++/CUDA language [1], in order to exploit the GPU parallelization to simulate a great number of particles representing the plasma beam formed. Some additional information about this secondary plasma obtained from the simulated model, which cannot be directly achieved by the experimental data, are also shown.

This work of thesis will proceed as follows:

- *Chapter 1* gives an overview about the main features of nuclear fusion and the future ITER project. The main aspect of neutral beam injectors and negative ions production are also described. To conclude, a brief description of PRIMA facility is provided.

- *Chapter 2* describes the NIO1 experiment. In particular, a detailed description of the diagnostic system is provided.

- *Chapter 3* presents and compares the experimental data collected during the experimental campaigns. Different sets of experimental data, collected when one of the main parameters which characterizes the extraction and the acceleration of the negative ions was changed, are analyzed.

- *Chapter 4* analyzes the data collected by the visible cameras. After the description of the calibration of the two cameras, a computer beam tomography is shown. The results obtained are compared with the experimental data.

- *Chapter 5* explains the plasma beam formation and evolution. A description of the PIC code used is provided and the results are compared with the experimental data collected by the Langmuir and RFEA probe. Finally, the results obtained from the model are used to achieve additional information about the plasma beam properties.

Chapter 1

Controlled nuclear fusion and the ITER Project

1.1 Why fusion?

Nuclear fusion is the process by which two or more atomic nuclei join together, or "fuse", to form a single heavier nucleus. During this process, matter is not conserved because some of the mass of the fusing nuclei is converted to energy which is released.

Energy from fusion reactions is the most basic form of energy in the Universe: our Sun and all other stars produce energy through thermonuclear fusion reactions. The fusion of two nuclei with lower masses than iron, the nucleus with the largest binding energy per nucleon, generally release energy, while the fusion of nuclei heavier than iron absorbs energy; the opposite is true for the reverse process, *nuclear fission* (Figure 1.1). There are extreme astrophysical events that can lead to short periods of fusion with heavier nuclei: this is the process that gives rise to *nucleosynthesis*, the creation of the heavy elements during events such as *supernovae* [2].

From the point of view of producing energy, fusion offers several advantages over fission. One advantage is that the reserves of fusible isotopes are much larger than those of fissionable isotopes, at a reasonable price, available in all locations of the Earth. Deuterium, one of the two main ingredients of nuclear fusion, is present in the water of the oceans in a concentration of 33 g per ton, practically limitless with respect to the needs for the future fusion reactors. Another advantage is that the products of fusion reactions are less radioactive than the products of fission reactions. Alpha particles are the last nuclear fusion products, which are stable nuclei; only fusion reactor structural components remain radioactive following neutron collisions but with lifetime shorter than 100 years. The last advantage of fusion
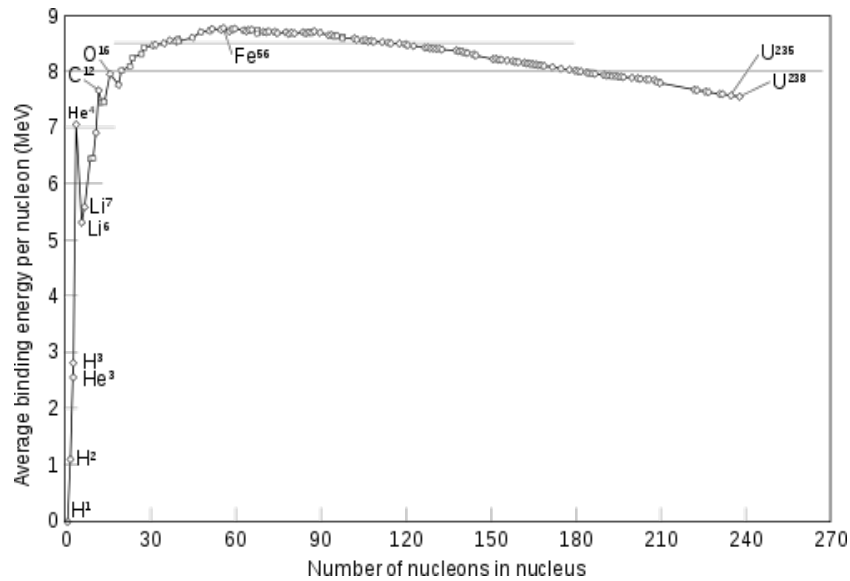
Figure 1.1: *Average binding energy per nucleon as a function of the mass number A.*

lies in its inherent safety. There would be very little fusible material in the reactor and the likelihood of a runaway reaction would thus be very small. Furthermore, the reaction is so hard to achieve that small perturbations in reactor conditions would probably terminate it.

Building upon the nuclear transmutation experiments by Ernest Rutherford, carried out several years earlier, the first step toward nuclear fusion was the study of heavy hydrogen isotopes obtained for the first time by Mark Oliphant in 1932. Research into fusion for military purposes began in the early 1940s as part of the Manhattan Project, but it was not obtained until 1951, and nuclear fusion on a large scale in an explosion was first carried out on November 1,1952, in the Ivy Mike Hydrogen bomb test [3]. Research into developing controlled thermonuclear fusion for civil purposes also began in the 1950s, and it continues to these day. Two projects, the National Ignition Facility [4] and ITER [5] are in the process of reaching *breakeven* after 60 years of design improvements developed from previous experiments.

ITER history and development will be described in the following paragraphs.

1.2 How does fusion work?

The key concept behind the release of energy in nuclear fusion (and fission) is the *binding energy*, the energy released when a nucleus is created from a couple of

nuclei; the greater the binding energy per nucleon in the atom, the greater the atom stability. Fusing two nuclei of very small mass, such as hydrogen, will create a more massive nucleus and the process releases energy. From the plot of the binding energy as a function of the mass number (A) it can be seen that helium (with A=4) is particularly stable (Figure 1.1); it is therefore of interest to pursue a fusion reaction that will have this atom as product.

A fusion reaction between two nuclei, such as for instance between deuterium (D) and tritium (T) which are both isotopes of hydrogen (H), will only occur when the nuclei are very close ($\approx 10^{-15}$ m), such that the strong interaction dominates. For larger distances, the electromagnetic interaction dominates and since both nuclei are positive there is a large repelling force (Figure 1.2). For a fusion reaction to occur, the products must overcome the repelling electro-static force or, in other words, they have to overcome the Coulomb barrier. This means that, in order for a reaction to occur, the nuclei must have a large initial energy, such that they can approach each other closely and overcome the barrier. The whole problem of fusion research becomes the generation of the conditions under which a sufficient amount of fusion reactions occur.
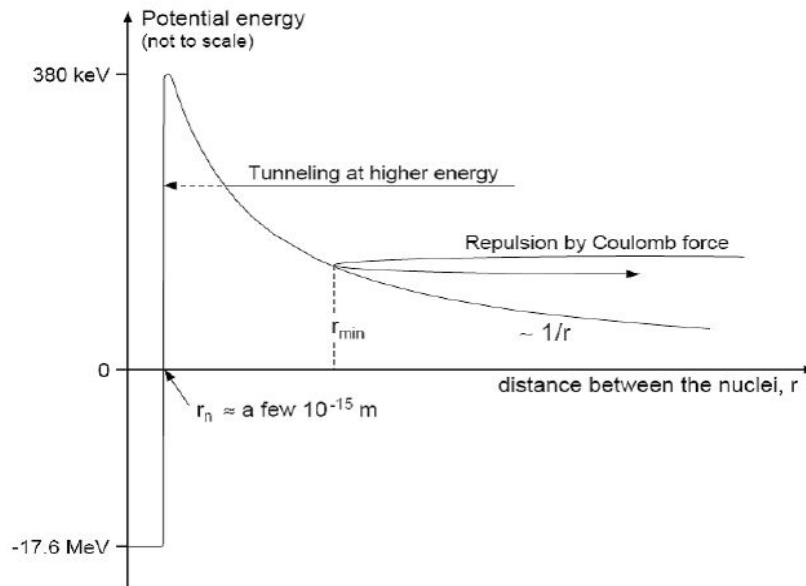
Figure 1.2: *Potential energy schematic representation of a Deuterium-Tritium reaction as a function of their relative distance.*

The fusion reactions most analyzed are

$$
\begin{aligned}
{}_1^2 D + {}_1^3 T &\longrightarrow {}_2^4 He + {}_0^1 n + 17.6\ MeV \\
{}_1^2 D + {}_1^2 D &\longrightarrow {}_2^3 He + {}_0^1 n + 3.3\ MeV \\
{}_1^2 D + {}_1^2 D &\longrightarrow {}_1^3 T + {}_1^1 H + 4.03\ MeV \\
{}_1^2 D + {}_2^3 He &\longrightarrow {}_2^4 He + {}_1^1 H + 18.3\ MeV
\end{aligned}
\tag{1.1}
$$
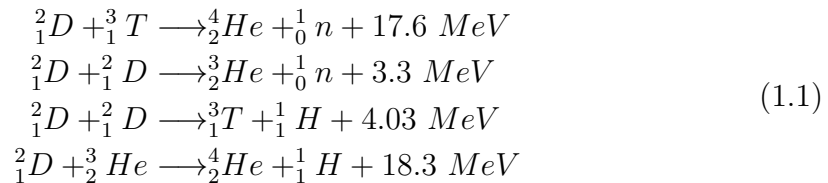
where the energy released follows from the mass difference between the nuclei on the left and the right hand side of equation [6].

As shown before, deuterium and tritium are the main ingredients in most fusion reactions. Deuterium is a stable form of hydrogen which is found in ordinary water. Tritium is a radioactive form of hydrogen, not found in nature. It can be obtained from lithium, a relatively abundant metal found in mineral ores and also extractable from seawater by the following reactions [7]

$$
\begin{aligned}
{}_3^6 Li + {}_0^1 n &\longrightarrow {}_2^4 He + {}_1^3 T + 4.8\ MeV \\
{}_3^7 Li + {}_0^1 n &\longrightarrow {}_2^4 He + {}_1^3 T + {}_0^1 n - 2.5\ MeV.
\end{aligned}
\tag{1.2}
$$
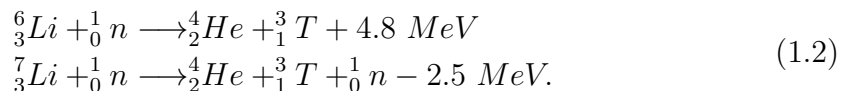
A simple calculation shows that if only 1% of the deuterium in world's oceans, equivalent to 10^{40} atoms of deuterium, is used to produce lithium, this would be equivalent to using up all the world's fossil fuel reserves 500,000 times.

Here it is also worthwhile to note that the energy released in a fusion reaction greatly exceeds that of a typical chemical reaction (eV range). Burning 1 kg of a deuterium/tritium mixture would lead to an energy release of $3.4 \cdot 10^{14}$ J; this can be translated in 3.9 Giga Watt during a period of 24 hours [8]. An ideal very large reactor would therefore burn an amount of fuel in the range of one kg per day.

The likelihood of a fusion reaction is expressed in terms of a cross-section. It is of interest to operate a fusion reactor at the lowest possible reagent energy, and it can be seen that there is a large difference in cross section for these reactions in the lower energy range (up to 10 keV). Figure 1.3 shows the so called *reactivity*, defined as the probability of reaction per unit time per unit density of target nuclei [9]. It is evident that the reaction between deuterium and tritium is the one with highest reactivity at lower energy and for this reason is the most investigated; from here on the reaction between deuterium and tritium will be considered.

The main contribution to the fusion reactions comes from an energy somewhere between the energy with the largest particle density, assuming a particle Maxwell distribution, and the energy for which the maximum cross section is reached: there are many particles at low energy, but the cross section is too small to give a significant contribution, the opposite for high energy.

The temperature at which the current fusion reactors are supposed to operate, 5-12 keV, is low when compared with the energy at which the maximum cross
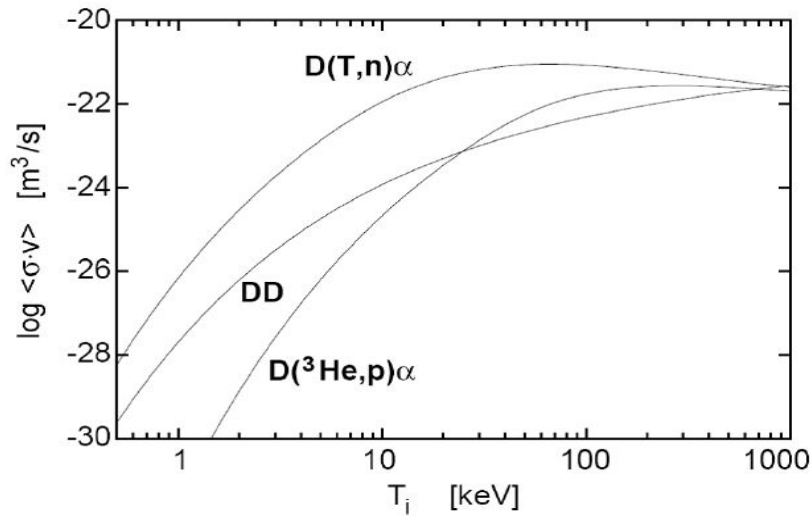
Figure 1.3: *Fusion cross section for the principal nuclear reactions as a function of temperature.*

section is obtained, but it must be noted that energies of 10 keV correspond to a temperature of roughly 100 million Kelvin. At these temperatures matter is fully ionized, a state of matter called plasma. Because of the large energies, the charged particles would leave any vessel in a very small amount of time. An idea of the timescales involved can be obtained by considering that the thermal velocity for a 10 keV particle is around 10^6 m/s for deuterium nuclei, and $6 \cdot 10^7$ m/s for an electron; this means that, if the reactor would had a typical size of 10 m, all the material would be lost to the wall in 10 μs.

For this reason, thermonuclear fusion reactors require a special scheme of operation in which one either tries to prevent the rapid loss or finds a way to generate enough fusion reactions within this short time.

In the next section two different approaches under investigation to obtain this goal will be illustrated.

1.2.1 Ignition and confinement

There are two different lines of research that try to exploit the high energies and velocities of the particles involved in fusion processes. One of them is based on the rapid compression and heating of a solid fuel pellet through the use of laser or particle beams: this is the *inertial confinement*, a method which tries to obtain a sufficient amount of fusion reactions before the material moves away [10].

The other approach, known as magnetic confinement, uses a magnetic field to

confine the plasma. The Lorentz force connected with the magnetic field will in fact prevent charged particle from moving over large distances perpendicular to the field. Charged particles will gyrate around the magnetic field in an orbit characterized by the Larmor radius

$$\rho = \frac{mv_{th}}{ZeB}.$$ (1.3)

For a magnetic field of 5 Tesla and a temperature of 10 keV, the Larmor radius is 4 mm for the deuterium nuclei and 0.07 mm for the electrons. Even if these scales are small compared to the size of any feasible reactor, the problem is more complicated. The particles are free to move along the magnetic field lines, and the currents in the plasma can, furthermore, influence the magnetic field. It is important to note that only charged particles are confined by the magnetic field: the neutrons generated by the fusion reactions leave the plasma on a time-scale of micro-seconds, resulting in a large flux on the material walls.

The ignition is the ideal operation condition for a fusion reactor, in which it would produce more fusion energy compared with the energy required to keep the reaction going. A criterion, called Lawson criterion from the name whom formulated it, provides a threshold for the product of density and the confinement time, the length of time for which particles are confined within the plasma. The Lawson criterion is also known as the *break-even conditions*, defined as the condition for which the total generated fusion power is equal to the power that heats the plasma. Considering a plasma containing a mixture of deuterium and tritium and assuming that the two densities are equal n, one obtains a total fusion power per unit of volume [11]

$$P_{fusion} = \frac{1}{4}n^2\langle\sigma v\rangle_{DT}E_{fus}V,$$ (1.4)

where $\langle\sigma v\rangle_{DT}$ is the reaction reactivity ans E_{fusion} the energy released. This power must be compared with the power that heats the plasma P_{heat}. In P_{fusion} definition important plasma parameters are contained, like density and temperature, through the cross section; in the temperature range of interest (5-15 keV), the reactivity can be well approximated by $\langle\sigma v\rangle_{DT} \approx 1.1 \cdot 10^{-24}T_K^2 m^3/s$, with T_K temperature in keV. Introducing the confinement time τ_E, the characteristic time on which the plasma loses energy W, one can write

$$\frac{\partial W}{\partial t} = -\frac{W}{\tau_E} + P_{heat},$$ (1.5)

where the stored energy can then be expressed as $W \approx 3nTV$ with T expressed in elettronvolt.

In a steady state $(\partial W/\partial t = 0)$ the ratio of total fusion power P_F and total heating power of the plasma is

$$\frac{P_{fusion}}{P_{heat}} = 0.16 n_{20} T_K \tau_E, \tag{1.6}$$

where τ_E is in second.

It is now possible calculate the break-even condition, by setting $P_{fusion}/P_{heat} = 1$: the equation above then directly gives

$$n_{20} T_K \tau_E > 6 \ m^{-3}s \ keV. \tag{1.7}$$

The condition for plasma ignition can be derived by assuming that there is no external heating power and, since only the alpha particles heat the plasma, it can be assume that $P_{heat} = P_{fusion}/5$, which yields

$$n_{20} T_K \tau_E > 30 \ m^{-3}s \ keV. \tag{1.8}$$

The product $nT\tau_E$ has become the measure of the progress in fusion. The future experiment ITER is supposed to reach values very close to ignition (Figure 1.4) [12].
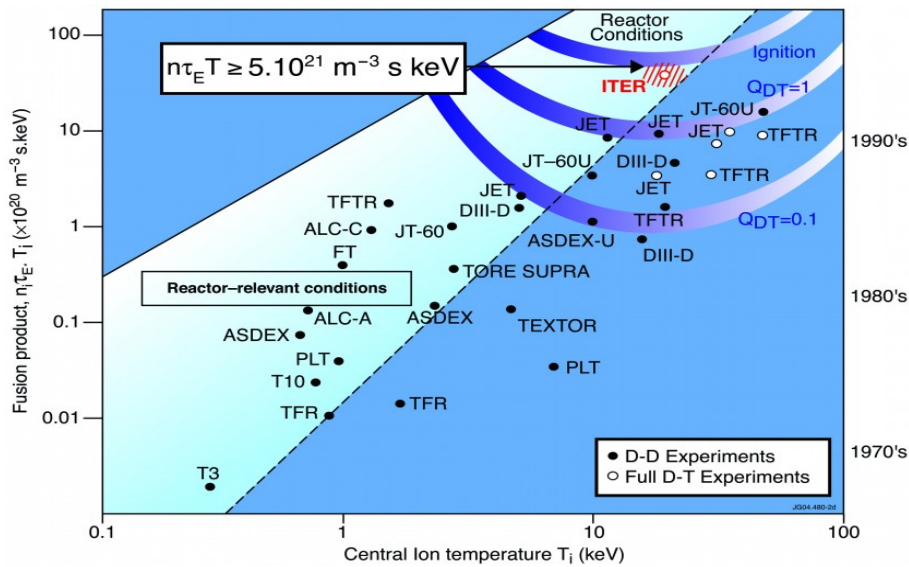
Figure 1.4: *Graphic of $n_{20} T_K \tau_E$ achieved on different magnetic fusion facilities.*

1.3   The ITER Project

ITER (Latin word for *the way*) is an international nuclear fusion research and engineering project. Nearly 30 years ago, the European Union (Euratom), Japan, the Soviet Union and the USA decided to develop a new, cleaner and more sustainable source of energy. What was born as an inspiration has became reality on 21 November 2006 by way of an international agreement signed in Paris to establish "The ITER international Fusion Energy Organization for the Joint Implementation of the ITER Project" [13]. Nowadays in southern France, at the ITER site in Saint Paul-lez-Durance, 35 nations are collaborating to build the world's largest tokamak, one of the most explored configurations for magnetic confinement. From 50 MW of input power, the ITER machine is designed to produce 500 MW of fusion power (Q=10), the first of all fusion experiment to produce net energy. A computer view of ITER is given in figure 1.5.
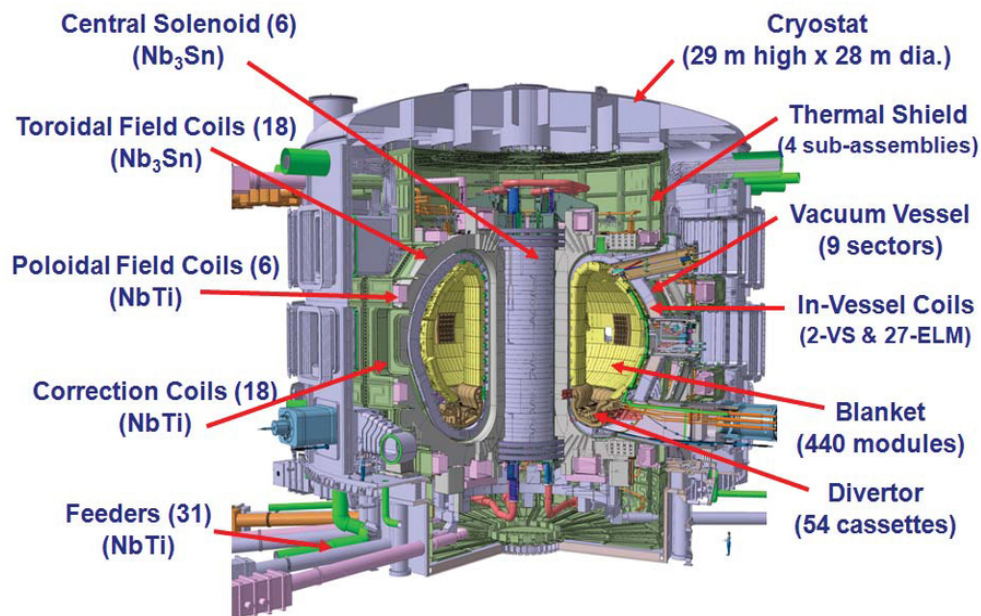
Figure 1.5: *Principal ITER components.*

1.3.1   The tokamak

Most of the fusion devices in the world today are of the tokamak type: it is the most investigated configuration and it is the one which comes closest to the ignition conditions. Tokamak was invented in the 1950s by Soviet physicists Igor Tamm and Andrei Sakharov, inspired by an original idea of Oleg Lavrentiev [14].

In a tokamak, three superimposed magnetic fields enclose the plasma: a ring-shaped field produced by plane external coils, the field produced by the current flowing in the plasma and a vertical field which fixes the position of the current in the plasma. The field lines of the first two combined field run helicoidally around the torus centre. In this configuration the plasma has the shape of a donut, with rotational symmetry around the vertical axis (Figure 1.6)[15].
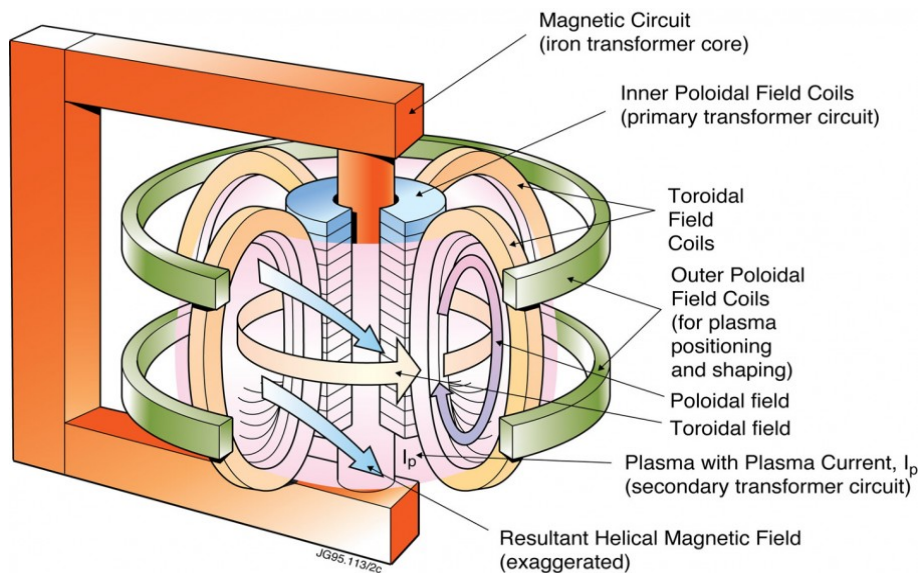
Figure 1.6: *Magnetic field in tokamak configuration.*

To lowest order, the particles gyrate around the field lines while moving freely along the field, ignoring the drift motion due to the inhomogeneous magnetic field. Because of the divergence-free nature of the magnetic field, it can be proven that such a configuration is the simplest possible topology in which a field line can remain in a finite volume of space. This is also possible since the product between current density and the magnetic field $j \times B$ balances the kinetic pressure.

The ITER magnet system will be the largest superconducting magnet system ever built: composed of thousand tonnes of magnets (51 GJ of stored magnetic energy), it becomes superconducting when cooled with supercritical helium in the range of 5 Kelvin. The toroidal field is produced by eighteen "D"-shaped toroidal field coils, placed around the vacuum vessel, designed to produced a total magnetic energy of 41 GJ and a maximum magnetic field of 11.8 T. The poloidal field system instead is composed by six ring-shaped coils situated outside of the toroidal field magnet structure, aimed to shape the plasma and to contribute to its stability by keeping it away from the walls. With the largest diameter of 24 meters, these are designed to produce a total magnetic energy of 4 GJ and a maximum magnetic field of 6 T [16].

1.3.2 Plasma heating

One of the main requirements for achieving fusion is to heat the plasma to very high temperature (ten of keV). In ITER, three main different heating methods will contribute to bring the plasma in the core of the machine to the temperature of 150 million degrees (Figure 1.7).
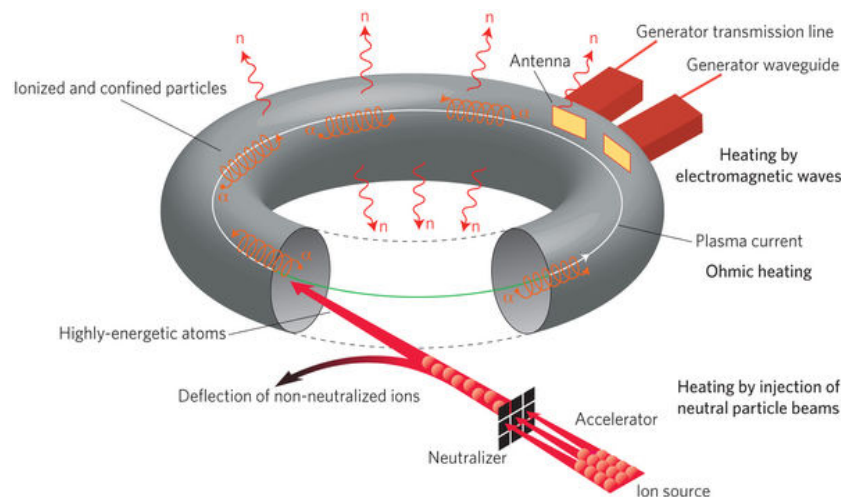
Figure 1.7: *Different plasma heating methods.*

- *Ohmic Heating.* The plasma current which is induced in order to provide the poloidal magnetic field, produces heat just like a wire warms up when an electric current flows through it. As this current travels through the plasma, in fact, electrons and ions become energized and collide. Because of these collisions, a resistance is created and results in thermal energy of the particles. However as the temperature of the plasma rises, this resistance, and therefore the heating effect, decreases. It can be shown that obtaining ignition only with ohmic heating is extremely difficult, if not impossible, for typical engineering and plasma physics constraints [17]. The biggest difficulty in fact arises from the fact that the resistivity decreases with temperature $\eta \sim 1/T^{3/2}$. Thus, as the plasma is heated, its resistivity decreases, implying a corresponding reduction in heating efficiency.

- *Radio-frequency heating.* Launching RF waves into a plasma is a successful technique for raising the temperature to the level required for ignition, in the same way as using a microwave oven to cook food. In the case of fusion, if the launching frequency is carefully chosen, the RF waves resonate with one of the natural frequencies of the plasma, leading to a large absorption of power

that appears in the form of heat and as a non-inductive current. In ITER the high temperature and current drive inside the vessel will be achieved by RF Heating and Current Drive (H&CD) systems, composed with ion cyclotron (IC), electron cyclotron (EC) and possibly lower hybrid current drive (LH) in a later phase. Each of those are required to couple up to 20 MW heating power to the plasma, which is beyond what has been achieved on the previous tokamaks [18].

- *Neutral beam injection.* One highly successful method of raising the plasma temperature well above the maximum achievable ohmic value is by means of neutral beams. This method will be described later in order to introduce the experiment on which this work of thesis is based.

1.4 Neutral Beam Injection (NBI)

Neutral beam heating was developed in the early 1970's and it is now the most important method for plasma heating in almost all fusion experiments. Consider a beam of high-energy neutral particles, for instance deuterium atoms, where high-energy means a beam energy much higher than the desired plasma temperature of 15 keV. Since the particles are electrically neutral, they are unaffected by the magnetic field and travel along straight-line trajectories until they are ionized by collisions with the background plasma. Once ionized the neutral beam particles are magnetically confined, they become part of the plasma, contributing to the high-energy tail of the deuterium distribution function.

The neutral beam particles H_b^0 are trapped into the plasma through the following reactions:

$$
\begin{aligned}
H_b^0 + H_p^+ &\longrightarrow H_b^+ + H_p^0 \ (charge\ exchange) \\
H_b^0 + H_p^+ &\longrightarrow H_b^+ + H_p^+ + e^- \ (ionization\ by\ ions) \\
H_b^0 + e^- &\longrightarrow H_b^+ + 2e^- \ (ionization\ by\ electrons)
\end{aligned}
\tag{1.9}
$$
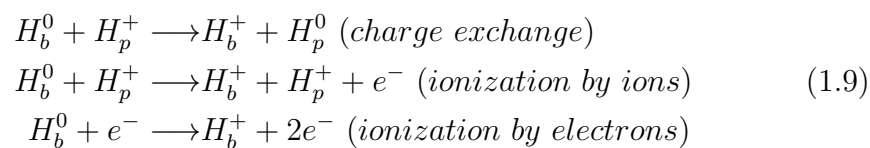
where the subscript b and p stand for *beam* and *plasma* [19].

Fast neutral atom beams are generated with charge exchange neutralization of high energy ion beams. Neutral beam injections with negative ions (NI-NBI), mainly H^-, are much more efficient in producing high energy neutral beams than positive ions, because of higher neutralisation efficiency at energies higher than 100 keV (Figure 1.8) [20]. For the next generation tokamaks, like ITER, a beam energy of 1-2 MeV is required, and this is a major reason
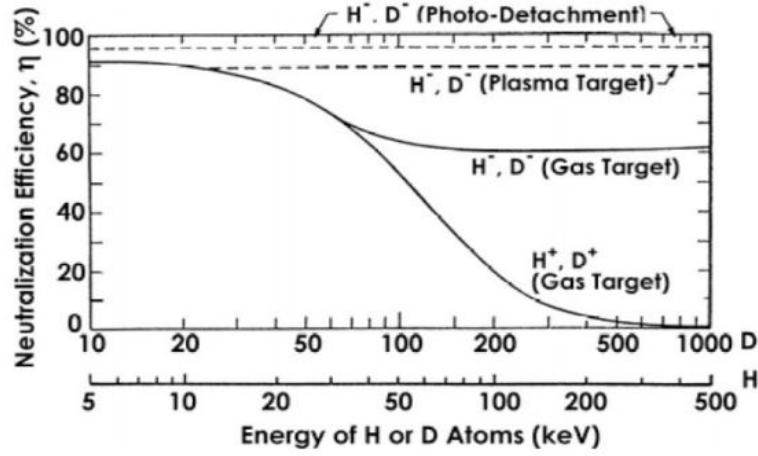
Figure 1.8: *Neutralization efficiency of positive and negative beam sources for different targets as a function of energy.*

why NI-NBI is being developed, although there are a lot of harder problems in producing negative ion beams than positive ones.

NI-NBI system consists in a beam source with negative ions, an accelerator and a neutralizer. In ITER (50 MW of power) D beams of 1 MeV will be injected in the plasma using two injectors (with the possible addition of a third injector): to obtain this goal the beam source has to produce 40 A for 3600 s.

Negative ions are produced in the plasma source. After the extraction they are accelerated to a high energy before crossing a charge exchange cell where they are neutralized. The neutralization is only partial and the remaining ions are deflected magnetically and sent to a dump. Considering the linear density expected for ITER, the exit of the neutralizer will be composed for the 60% of neutral atoms, 20% of negative hydrogen ions H^- and 20% of positive hydrogen ions H^+. The neutrals can cross the magnetic field and reach the plasma where they get ionized, transferring their energy to the plasma bulk by collisions with electrons and ions (Figure 1.9).

Because of the very low affinity of the hydrogen ion H^- A=0.75 eV, ions can easily lose the electron and become neutral. H^- ions, similarly for D^-, can be destroyed mainly by three processes:

$$H^- + e^- \longrightarrow H + 2e^- \; electron \; stripping$$
$$H^- + H^+ \longrightarrow 2H \; mutual \; neutralization \tag{1.10}$$
$$H^- + H \longrightarrow H_2 + e^- \; or \; 2H + e^- \; associative \; detachment.$$
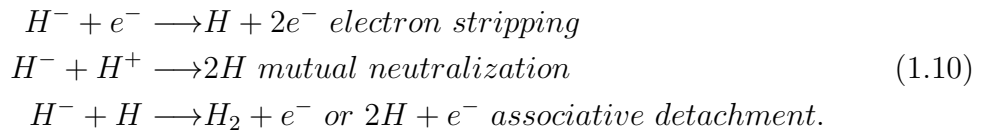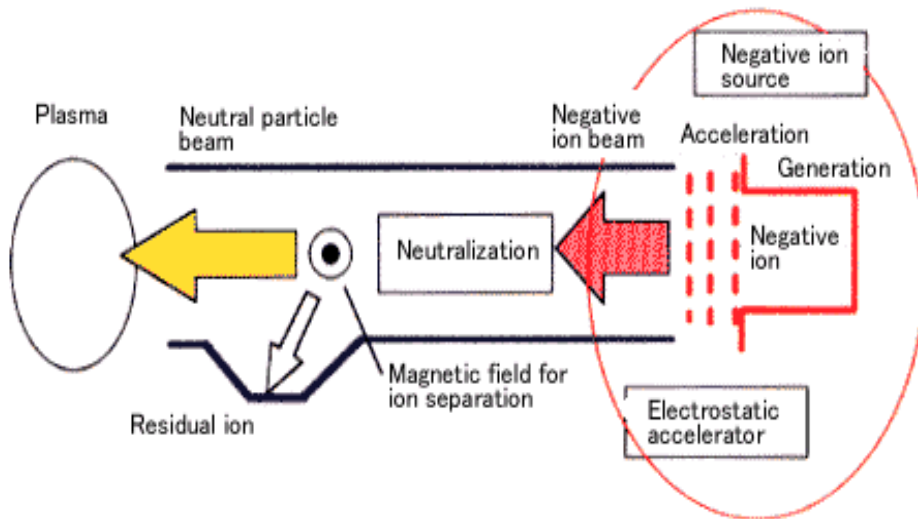
Figure 1.9: *Principle behind the neutral beam injector.*

In order to increase the production of negative ions, cesium is added inside the source. Covering with cesium the internal source walls decreases the negative ion extraction potential with consequent improvement in ions production. In addiction to this, thanks to its very low ionization potential (E=3.894 eV) it can relatively easy lose electrons which are bound to D.

For all ion beams, the simplest neutralization cell is a box filled with gas; at energies around 1 MeV, the maximum efficiency of gas neutralizers is about 60% for negative ions, but they can reach an efficiency of up 85% if the plasma in the cell is fully ionized [21].

1.4.1 Negative ion production

Negative ion production in the source region can be achieved through two main ways: surface and volume production.

- – *Surface production.* In surface production the ions are produced when hydrogen atoms bounce off walls coated with cesium, which serves as source of electrons. The probability of electron capture during backscattering from surface of hydrogen atoms or hydrogen ions depends on the work function Φ of the surface, on the electron affinity A and also on

the perpendicular velocity of the escaping ion [17]:

$$\gamma(H^-, H) = exp(\frac{\phi - A}{Cv_\perp}),$$
(1.11)

where C is a constant and $\phi - A$ represents the energy difference between the Fermi level of the surface and the electron affinity level.

In general it can be said that negative ions are made in reactions

$$H^0 + e^- \longrightarrow H^-$$
$$H^+ + 2e^- \longrightarrow H^-.$$
(1.12)

Sources optimized for negative ion surface production must have as many atoms as possible in contact with surface, the atom and positive ion energy in the tens of eV range to maximize the negative ion yield and the path of the negative ions in the source must be minimized to avoid destruction before extraction and subsequently acceleration.

— *Volume production.* In volume production one tries to maximize the production of negative ions by dissociative attachment of electrons on high vibrational states of hydrogen molecules. When the hydrogen molecules are in high vibrational states, they are prone to dissociating and attaching to a low energy electron.

Fast electrons excite H_2 molecules with collisions (T_e about 5-10 eV) to high vibrational levels. Then the excited H_2 molecules drift to the second chamber where the lower electronic temperature (T_e about 1-2 eV) maximizes the dissociative attachment reaction rates and minimizes the neutralization probability of H^- by electronic and ionic collisions [22].

Negative ion extraction and acceleration has many features which make it much more complex than that of positive ions, not only because they are harder to create. The negatively charged ions are accompanied by co-accelerated stray electrons originating mainly from the source plasma (because of their negative charge); furthermore the fragile negative ions may be neutralized or may acquired a positive charge during the acceleration. In addition to this, electrons created in the extractor and accelerator can impinge on the extraction and acceleration grids, leading to high power loads on the grids. Finally the positive ions created in the accelerator by ionization of the background gas are back-accelerated into the ion source creating a massive power load to the ion source.

1.4.2 Negative ion extraction and acceleration

The plasma in large volume devices can be generated by hot cathodes (heated filaments or bow discharge) or radio-frequency (RF) antennas (inductively coupled plasma) standing either inside or outside the discharge. Ion sources for fusion are devices with the so called *expansion chamber*, juxtaposed next to the discharge region. The expansion chamber is often magnetized with magnetic field lines perpendicular to the electron flux exiting the discharge. The magnetic field strength is typically of the order of ~ 0.01 T. It is generated either by permanent magnets along the lateral walls of the ion source or via a large current flowing through the plasma electrode, which is also called *plasma grid* [23]. The plasma grid (PG) separates the ion source plasma from the accelerator region, where the extracted negative ions are accelerated to high energies. The axial electron mobility is strongly reduced by the magnetic field inside the expansion chamber to significantly decrease electron temperature as electrons loose a large amount of energy through collisions. The magnetic filter reduces the electron temperature down to eV level in the extraction region (close to the PG), increasing the survival rate of the negative ions. The ions produced in the source are then extracted by the Extraction Grid EG through the apertures of the PG.

After the ions are extracted, they are accelerated up to the desired energy by the electric field produced by a series of grids, biased at increasing negative voltages up to the Grounded Grid (GG) which is at 0 V. The voltage drop between the PG and the EG determines the extracted current from the source. The voltage drop between PG and GG determines instead the ions final energy. In order to avoid the back-streaming of positive ions created by ionization of atoms in the background gas by the beam, there can be an additional electrode at a positive voltage, the *repeller* (REP). An example of this structure can be seen in figure 1.10.

In the next section the main characteristics of ITER Neutral Beam Test Facility (NBTF) will be illustrated.

SPIDER and MITICA: ITER heating neutral beam injectors

ITER will initially be equipped with two heating neutral beam injectors, designed to deliver 33.3 MW of either 1 Mev D or 0.87 MeV H^0 to the ITER plasma for up 3600 s. The beam energy needs to be above 300 keV, in order to deposit the power inside the H-mode transport barrier, when ITER is in the so called *H-mode* (High Confinement Mode). The ITER Neutral Beam Test Facility, called PRIMA (Padova Research on ITER Megavolt Acceler-
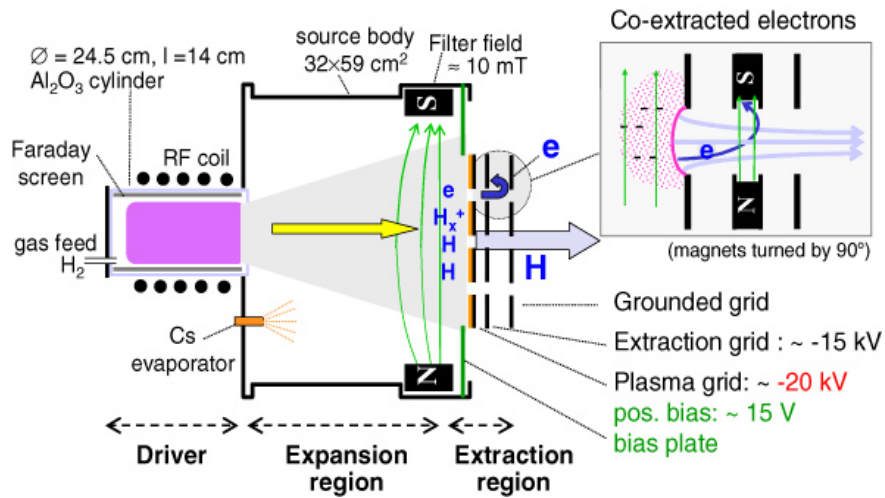
Figure 1.10: *Schematic view of the ITER NBI NI plasma source prototype; x corresponds th the axial beam direction while the y and z axis is in the plane of the extraction grid [24].*
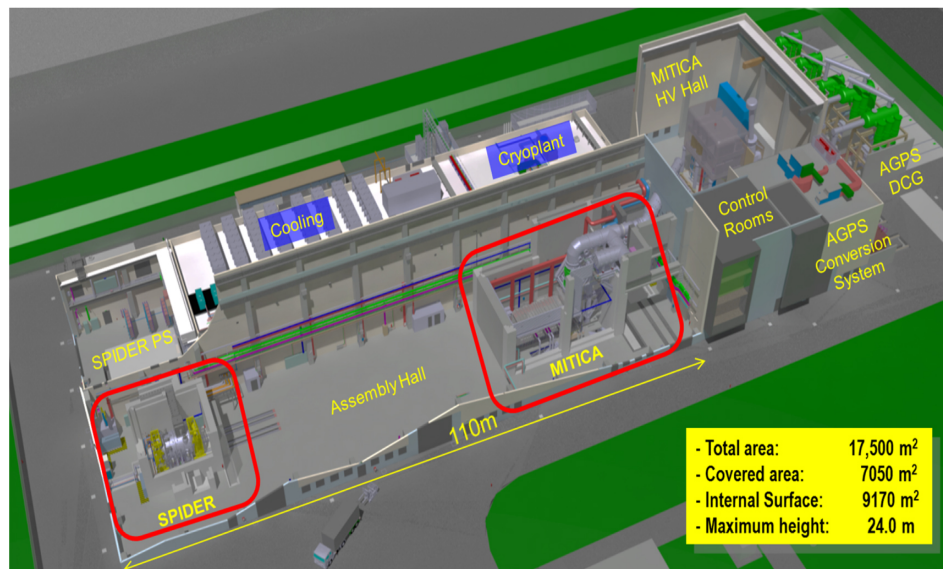
Figure 1.11: *CAD view of the PRIMA facility at Consorzio RFX.*

ator) is hosted in Padova, at Consorzio RFX (Figure 1.11). It includes two experiments: SPIDER (Source for the Production of Ions of Deuterium Extracted from a Radio Frequency plasma) and MITICA (Megavolt ITER Injector and Concept Advancement).

SPIDER (Figure 1.12) is designed to test the full-size ITER negative ion
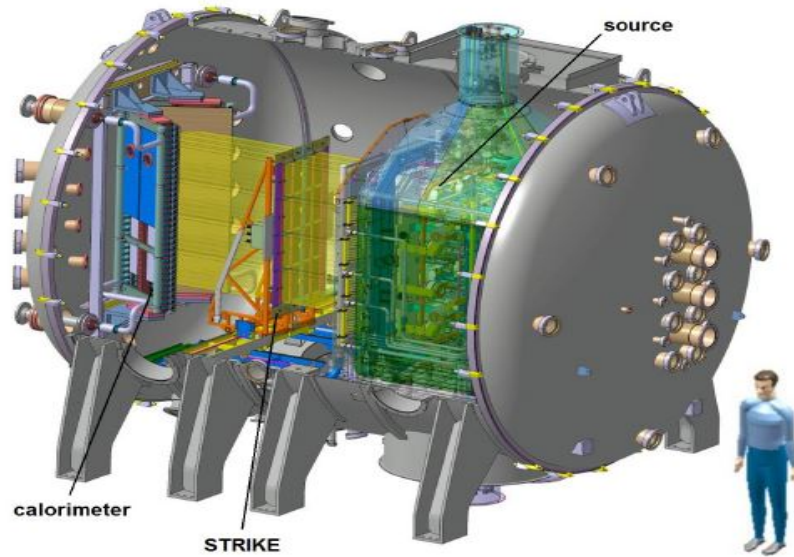
Figure 1.12: *3D view of SPIDER design.*

source which will be twice as large as the largest existing negative ion source (ELISE at IPP Garching in Germany **??**). It will be capable of running pulses of up to 3,600 seconds at maximum power and to demonstrate extraction and acceleration to 100 kV of a large negative ion hydrogen or deuterium beam, with co-extracted electron fraction $e^-/D^- = 1$ and beam uniformity within 10 %. SPIDER also features ITER-like filter field configuration and cesium oven layout and environment. Furthermore thanks to a wide set of diagnostics for beam characterization, it aims to optimize the negative ion source for the ITER Heating Neutral Beams HNBs [25].

MITICA, on the other hand, is a full-size heating neutral beam injector as shown in figure 1.13. MITICA will start operation more than five years before the heating beam will be used on ITER and it will take direct advantage of the design optimization carried out for SPIDER. A huge design and optimization effort has been focused on the critical aspects arising in the multi-stage, multi-beamlet negative ion accelerator and neutralizer, when voltage, current and pulse duration are increased. The main MITICA goals are improving of the high voltage holding capability, in order to reach the target particle energy of 1 MeV; maximizing the ion beam current produced up to 46 A in H^- or 40 A in D^-, minimizing transmission losses so as to deliver the target neutral beam power of 16.5 MW; minimizing the heat loads and thermo-mechanical stresses on all components, in order to guarantee the

required fatigue lifetime [26].

In the next chapter, the ion source NIO1, a reduced-size model of multi-aperture sources used in neutral beam injectors will be illustrated.
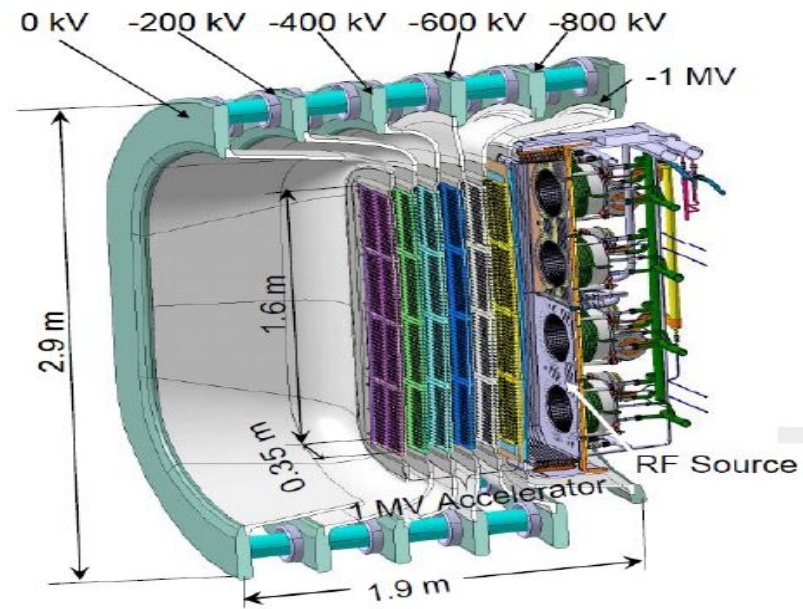
Figure 1.13: *3D view of MITICA design.*

Chapter 2

Negative Ion Source NIO1

The Negative Ion Optimization phase 1 (NIO1) is a small radio-frequency (RF) plasma driven negative ion source (Figure 2.1). It was installed in 2013-2014 at Consorzio RFX in collaboration with INFN (LNL) and in early 2016 it has finally reached extraction of a negative hydrogen beam. NIO1 target is the production of an extracted H^- beam of 130 mA composed by 9 beamlets arranged in a 3x3 matrix. It aims to accelerate the ions up to an energy of 60 keV, operating at an RF frequency of 2±0.2 MHz and a maximum power coupled to the source of 2.5 kW [28].

Figure 2.1: *Picture of NIO1 experiment.*

The NIO1 apparatus can be subdivided in three main parts as shown in figure

2.2:

- *The source.* In the source the plasma is generate by the external RF coil inductively coupled.

- *The accelerating column.* The negative ions extracted from the source are accelerated by a voltage drop between the grids in the accelerating column.

- *The diagnostic tube.* Once extracted and accelerated, the beam parameters are studied in the vacuum vessel with a set of different diagnostic techniques.

In the next sections all these components will be briefly described.
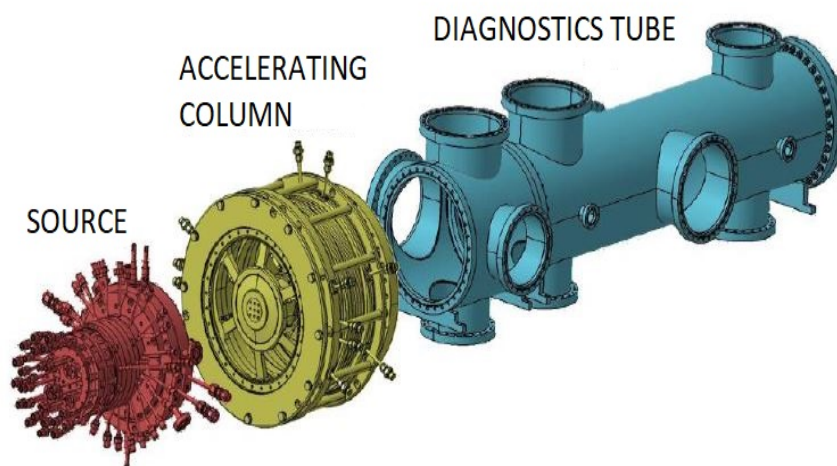
Figure 2.2: *Schematic view of the main NIO1 components.*

2.1   The source

A scheme of the NIO1 source is shown in figure 2.3. The plasma chamber is a cylinder of 50 mm radius and 210 mm length. It is composed by disk assemblies, with permanent magnets on the wall which provide a multipole field (m=7) for plasma confinement. The driver is a radio-frequency coil, connected to the 2 MHz, 2.5 kW RF generator by a simple matching box with the capacitor C_a (40 turn maximum and 60 pF per turn, for a maximum capacitance of 2.4 nF) in series and three capacitors in parallel with the RF coil. The RF window is a dielectric tube part, which is also part of the source plasma chamber wall. The RF power

is inductively coupled to plasma by a 7 turn coil which is wound around this 78 mm long dielectric tube made of Pyrex (R) ; the coil is water cooled while the dielectric tube is air cooled. The rear cover of the source has four ports dedicated to diagnostics: one is covered with a luxmeter sensor of 0.009 sr view angle at a 0.2 m distance, two with telescopes connected to a spectrometer and a calibrated photomultiplier (PMT) and the last one used for gas injection.
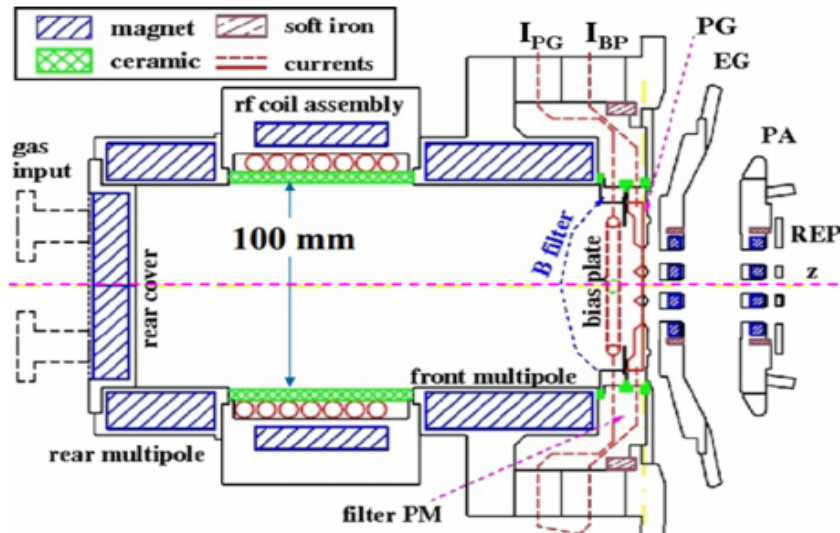
Figure 2.3: *Schematic view of the NIO1 source.*

There are other two notable parts of the plasma source: the Plasma Grid (PG) and the Bias Plate (BP). The plasma grid is the base of the cylindrical source, featuring 9 holes for beam extraction and carrying a filter current I_{PG}. It can also be considered as the first step of the accelerating column. In the PG support there are other six lateral ports, the lower port reserved for cesium injection (not available for the experimental campaigns described herein), the upper one for pressure measurement and the remaining ones are used for optical view lines. The bias plate is a molybdenum Mo collimator inserted in plasma, including cooled conductors which can carry a second filter current. It is placed just before the first grid of the acceleration system and it is composed of two elements: a rectangular frame named *Magnetic Bias Plate* (BP_m) and a round frame exposed to the plasma, called *Electrostatic Bias Plate* (BP_e). The other cylinder base and the lateral walls are electrically connected to each other (WW Wider Walls). In order to reduce the electrons losses during the acceleration, the source pressure is held between 0.3 and 1 Pa. The gas is fed into the source by a feedback-controlled valve. Two turbo-molecular and a rotary pumps, connected with the diagnostic chamber, pump the gas that passed through the electrodes grid and through the

accelerator. The source pressure is measured by a Pirani. A ITR 90 vacuum trans-
mitter consisting of two separate measuring systems: hot cathode Beyard-Alpert
and a Pirani measured the pressure in the vessel instead.

Some diagnostics allow to characterize plasma properties inside the source: the
plasma light detection system and the optical emission spectroscopy. They will be
briefly described in the following.

Plasma Light Detection System

Plasma Light Detection diagnostic is based on the fast response of a photodiode or
photomultiplier. This kind of devices are useful for studying plasma fast dynamics
and for detecting the plasma ignition or quenching. The light in NIO1 source
is collected by optical heads from one of the source ports and it is focused onto
an optical fiber of 0.4 mm of core diameter. The fiber carries the signal to a
Hamamatsu photomultiplier module, model H10722. It has an integrated high
voltage generator, a voltage output signal and it allows to change externally the
gain by a control voltage. The control voltage range is between 0.5-1.1 V, allowing
to amplify the signal by more than two orders of magnitude and it can be adjusted
by a 10 kΩ multi-turn potentiometer with a resolution of 1 mV [29].
A luximeter is also used to measure the photons emitted by the plasma in the
source.

Optical Emission Spectroscopy (OES)

Optical emission spectroscopy is commonly employed in the diagnosis of laboratory
plasma such as gas discharge plasma, inductively coupled plasma or laser induced
plasma. Numerous analytical techniques have been established to determine the
plasma properties such as electron density, plasma temperature, identification and
quantification of elements present in the plasma. These pieces of informations are
obtained from the analysis of the radiation spontaneously emitted by the plasma
source and by the extracted beam when interacting with the background gas.
In NIO1 source a spectrometer is used with a resolution capable to separate lines
whose wavelengths differ down to few nanometers. For this reason, a 16 bit Hama-
matsu mini-spectrometer TM series C10082CAH is used, with an integrated back-
thinned CCD sensor with 2048 pixels; the system has 1 nm resolution and spectral
window from 200 to 850 nm; its frame rate has a maximum of 100 Hz.
Furthermore, a high resolution spectrometer is needed for solving the rotational
and vibrational molecular spectra, with a resolution of about 0.05 nm. It must
cover a spectral range of several tens of nm in the visible spectrum. For this reason,
a Czerny-Turner spectrometer of 0.75 m focal length, mounting a grating of 1200
gr/mm and a 16 bit 2D back illuminated frame transfer CCD camera of 512x512

pixels of 13 μm-size is used. It has a spectral resolution of 0.05 nm, it can work between 350 and 1300 nm but it is capable to acquire a spectral range of only 5-6 nm [29].

The plasma and the beam emitted radiation is carried to the spectrometers by means of 0.4 mm core diameter optical fibers. Their optical heads design is standardized in order to be used not only by OES, but also by BES (Beam Emission Spectroscopy, see next section) and other diagnostics based on visible plasma light collection.

The determination of plasma electron density and temperature can be obtained using the line ratio method applied to the Balmer series [30]. Line emission ϵ_{pk} for atomic Hydrogen is correlated with the population density in the electronically excited state with quantum number p of atomic Hydrogen $n_H(p)$ by:

$$\epsilon_{pk} = n_H(p)A_{pk}, \tag{2.1}$$

where A_{pk} is the transition probability from level p to level k . The population density depends on plasma parameters such as electron density n_e and temperature T_e. They can be calculated with the so-called *collisional-radiative CR models*, which balance collisional and radiative processes for each electronic state and have to be used for non-equilibrium plasmas, such as low pressure or low temperature plasma [31].

An example of an acquired spectrum is shown in figure 2.4. The most intense lines clearly visible in the spectrum are the Balmer lines H_α, H_β and H_γ. Furthermore, the molecular H_2 emission of the Fulcher band is visible, mostly comprised in the wavelength range from 595 to 640 nm [32].
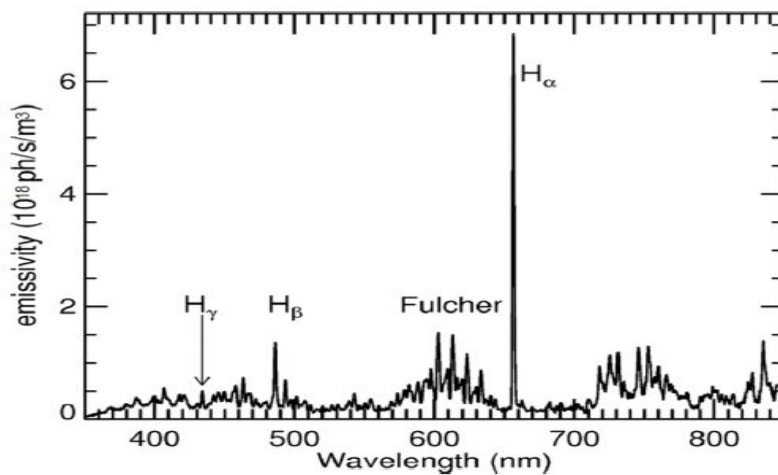
Figure 2.4: *Spectrum recorded by the low resolution spectrometer, in emissivity units.*

2.2   The accelerating column

Starting from the plasma grid, a set of four grids constitutes the accelerating column. Each grid features a 3x3 matrix of apertures equally spaced by 14 mm, with 3.8 mm radius of the PG apertures (Figure 2.5).
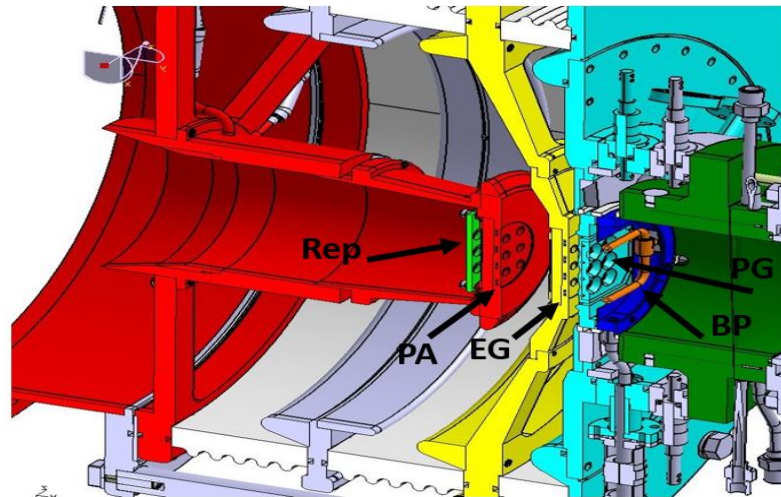
Figure 2.5: *Grids of NIO1 experiment.*

In order the grids are:

- *Plasma Grid PG.* As said before, it is the grid which faces the plasma. It is held at $V_S = -V_{PG} > 0$ which is the source acceleration voltage, with maximum values $V_S \leq 60$ kV.

- *Extraction Grid EG.* It is held at a higher voltage with respect the PG to extract and give a first acceleration to the negative ions. The extraction voltage is defined as $V_e = V_{EG} - V_{PG} > 0$, with maximum values $V_e \leq 9 \; kV$. By changing the extraction voltage one can change and optimize the beamlet optics.

- *Post Acceleration Grid PA.* Namely the grounded grid, it is held at ground potential.

- *Repeller Grid.* It aims to prevent the positive ions from being accelerated back inside the source. For this reason, it is usually held at ground or positive voltage.

In order to minimize the co-extracted electrons from the source, EG and PA feature also some embedded magnets. EG embedded magnets are called Co-extracted

Electron Suppression Magnets (CESM) and they force electrons to impact on the EG upstream face. PA magnets have the double target to suppress electron coming from the stripping process in the accelerating gap and to recover the small deflection angle induced by EG on the negative ion beamlets. To improve the EG grid operation, an upgrade in the magnets configuration was installed in May 2017. A brief description of the main changes will be provided in the next section.

2.2.1 Old and new extraction grids

The old and new extraction grids differ both from electrostatic and the magnetic point of view. The first change in the new extraction grid configuration is the increase of the extraction grid apertures. The new configuration, referring to it as EG_2, has an entrance radius $r_1 = 3.5$ mm (the old, called EG_1, $r_1 = 3.2$ mm), exit radius $r_2 = 5$ mm (EG_1 had $r_2 = 4.1$ mm) and a thickness of 10.3 mm with d_1=4.8 mm and $d_2 = 5.5$ mm (before they were d_1=8.8 mm and d_2=1.5 mm). The new EG is mounted at 5 mm from the PG while in the old configuration the gap distance g between the PG and EG could be adjusted in the range $g = 5 \pm 1$ mm (Figure 2.6) [33].
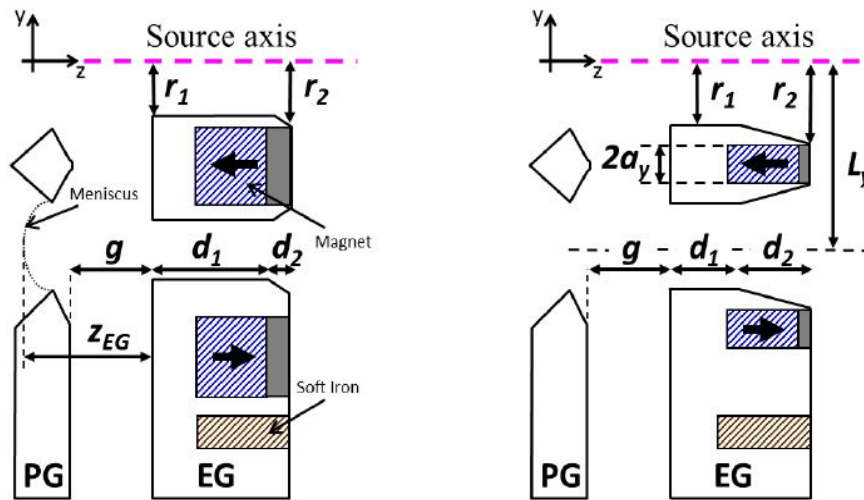
Figure 2.6: *Detailed view of the old (left) and new (right) extraction grid layout.*

Concerning the magnetic configuration, EG_1 features 4 vertical arrays of CESM magnets with magnetization along beam direction, alternatively oriented. The resulting magnetic field deflects the beamlets in opposite directions on the vertical axis (x axis in NIO1) since the B_Y component is stronger than the B_X. In order to compensate for the residual deflection after EG_1, due to the tail of the negative

peak of B_Y, a second set of equivalent magnets was embedded into the PA at a proper distance, with opposite orientation with respect to EG_1 CESM. Since EG_2 has a very different geometry with respect to EG_1 the magnetic configuration and magnets geometry has been changed.

The main CESM goal is to stop electrons co-extracted from source: for this reason the upstream B_Y peak must be large enough to dump electrons on EG face. Furthermore the other condition to fulfill is the zero ion deflection after EG. In the old configuration residual ion deflection recovery was provided by a second set of magnets designed to properly compensate for CESM effect, embedded in the PA. In the new configuration, a new way to fulfill both requirements is through a second set of magnets embedded in the EG, together with CESM, called ADCM (Asymmetric Deflection Compensation Magnets). They are placed in between the CESM array, forming a grid pattern that surrounds the beamlets with magnetization along the y direction. The effect of these magnets is to unbalance the B_Y component of the magnetic field with respect to the EG plane, increasing it on the upstream side and decreasing it on the downstream side (Figure 2.7).

The new NIO1 configuration has the CESM+ADCM configuration plus the old PA magnets contribution.
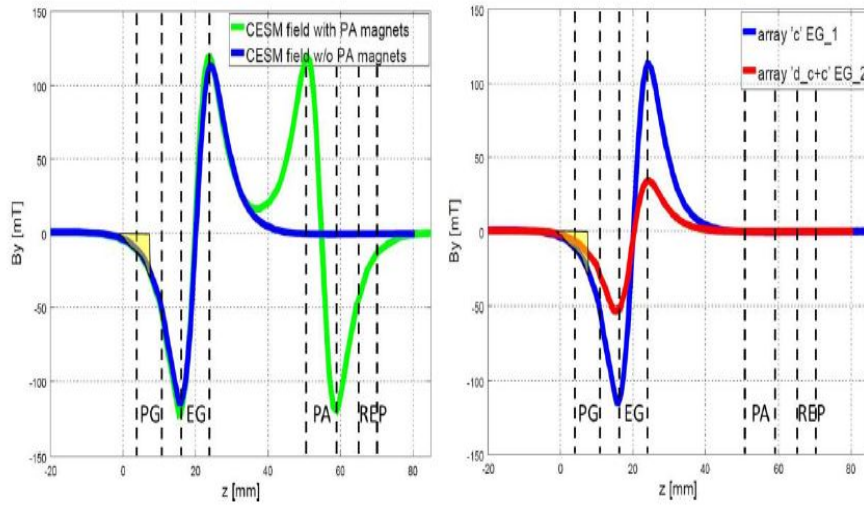
Figure 2.7: B_Y magnetic field in the old EG configuration (left) with or without the PA magnets in addiction to CESM. On the right the CESM+ADCM configuration in the new EG. The yellow area indicates the fraction of B_Y component inside the plasma chamber.

2.3   The diagnostic tube

After acceleration, the beam enters the beam tube, a 84 mm internal diameter tube, until it reaches the pumping cross and then the diagnostic chamber. As shown in figure 2.8 this is a 1.5 m long tube with a 350 mm internal diameter, where various ports allow different kinds of beam diagnostic.
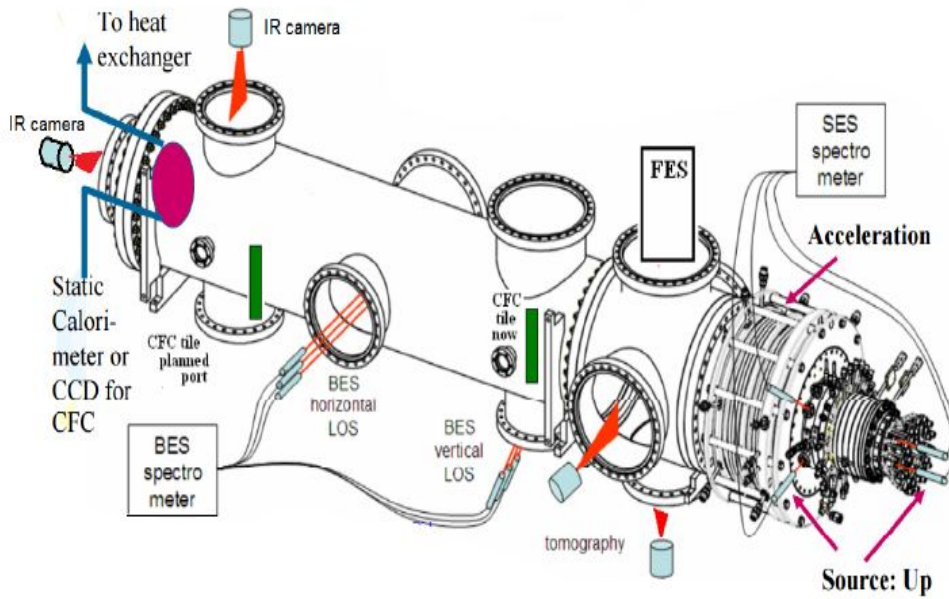
Figure 2.8: *NIO1 components.*

The different diagnostic systems are installed to provide a full characterization of NIO1 plasma in the source and the extracted beam. The aim is also to test them for future SPIDER and MITICA applications.
In the following sections a short description of beam diagnostics system is provided.

2.3.1   Beam Emission Spectroscopy (BES)

As said before, excited neutral particles are produced with the subsequent emission of photons by collisions with the background molecules. Beam emission spectroscopy is based on the study of these radiations produced by the interaction of the energetic ions with the molecules in the vacuum chamber, in front of the ion source grids. It enables to measure the beamlet divergence, uniformity and direction of propagation. It is a non invasive diagnostic which allows to measure

the fraction of ions neutralized in the accelerating system.

The most intense emitted radiation corresponds to the transition between the energetic levels H_α and D_α, namely n=3 to n=2 transition. These pieces of informations are deduced by comparison between the shifted and unshifted H_α components. The wavelength of the beam emitted radiation spectral line λ' is Doppler shifted according to

$$\lambda' = \lambda_0 \frac{1 - \beta \cos\alpha}{\sqrt{1 - \beta^2}} \tag{2.2}$$

in the frame of reference of the laboratory. λ' and λ_0 are the observed and the unshifted 656.2 nm H_α wavelengths respectively; β is the ratio between the speed of the ions and the speed of light and α is the angle between the de-excited neutral trajectory and the observation direction. In Figure 2.9 an example of BES spectrum is shown.
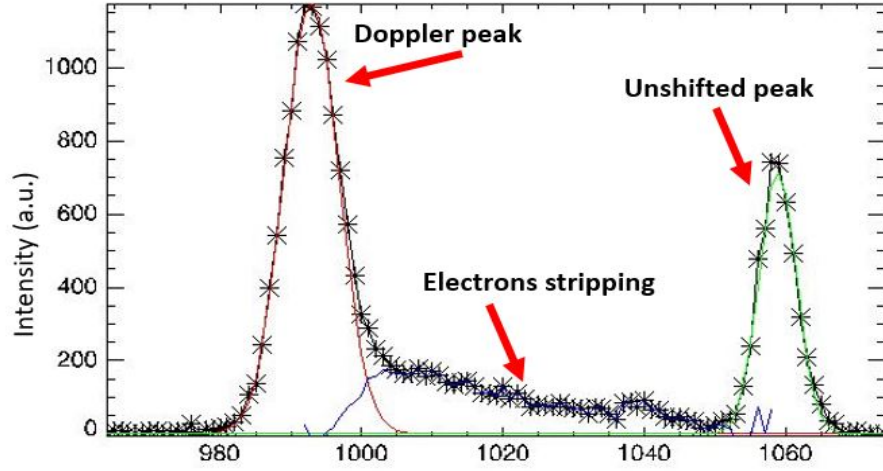
Figure 2.9: *Example spectrum acquired by BES diagnostic.*

Many bean parameters can be inferred by measuring the Doppler shift of H_α and the width of the unshifted H_α peak which is always present due to de-excitation of background gas. The linewidth $\Delta\lambda$ of the shifted H_α component is determined by the quadratic sum of a number of different effects:

$$\Delta\lambda^2 = \Delta\lambda_I^2 + \Delta\lambda_N^2 + \left(\frac{\lambda_0}{\sqrt{1 - \beta^2}}\beta\sin(\alpha)\right)^2 (\omega^2 + \epsilon^2) + \left(\frac{\epsilon\lambda_0}{mc^2\beta}(\beta - \cos\alpha)\right)^2 v^2 \tag{2.3}$$

where the intrinsic width of the line is $\Delta\lambda_I$, v is the voltage ripple of the grids, the broadening introduced by the spectrometer instrumental function is $\Delta\lambda_N$, the

angle ω with which the lens is seen by the emitting particle, namely the optical aperture, the mass m of the atom and the average divergence ϵ of the beamlets are the other parameters [34]. $\Delta\lambda$ allows to calculate the divergence of the beamlets while the uniformity of the beam can be measured by comparing the integral of the Doppler shifted component from the spectra of different Line of Sight (LoS). In NIO1 the H_α radiation emitted by the beam is collected by an optic head, whose LoS is oriented about 60° in the horizontal plane with respect to the beam axis (Figure 2.10). The optic head hosts a lens with focal length of 50 mm and clear aperture diameter 6 mm, focusing the collected light on a 400 μm core diameter silica-silica fiber with 0.22 NA. The light is conveyed though the fiber to an Isoplane SCT 320 spectrometer, with entrance slit width set at 50 μm and mounting a 200 gr/mm grating. The spectrometer is coupled with a PIXIS 2K/BUV camera, equipped with a back illuminated CCD of 2048x512 pixels, 13.5 μm x 13.5 μm large.
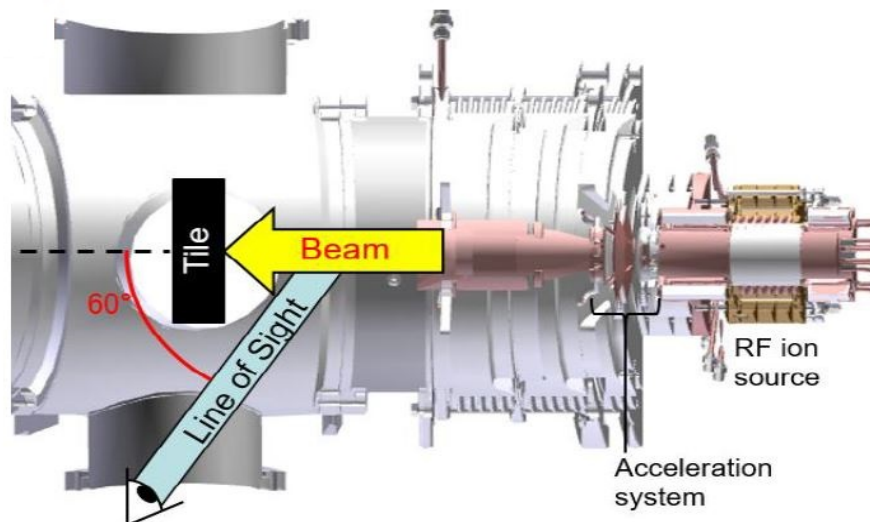
Figure 2.10: *NIO1 experiment and schematic representation of beam and BES LoS directions.*

2.3.2   Thermocouples

Eight thermocouples are installed on NIO1. They are E-type Teflon insulated with twisted wires. Thermocouples have the double aim of diagnostic devices and also to be used to control the temperature in order to avoid damages. The source and the grids as well as many others NIO1 components facing plasma are water cooled and it is important to keep under control their temperature. It is possible to measure the temperature difference between inlet and outlet water of each cooling

circuit; this difference is proportional to the power ceded by plasma or beam to components.

During breakdown, voltage oscillations up to several kV may arise so the thermo-couples are attached to the short metallic pipes (water pipes) between the source and insulated from them; the thermocouple cables run from the source to the High Voltage deck where the thermocouple electronics is positioned.

2.3.3 CFC Tile Calorimeter

The measurement of the energy flux profile of the beam can be achieved using an inertial calorimeter as beam target. The carbon fiber composite (CFC), with dimension 125x91x12 mm^3, has conductivity along z much greater than in the x and y direction: heat flux along z direction propagates 20 times faster than in the other directions. Beam profile and divergence are obtained by the measurement of the backside temperature recorded by infrared thermocamera, with a good spatial resolution. As the tile thickness is small and beam power is low, the profile of the temperature increase on the rear side is not expected to differ much from that on the beam facing side. Unfortunately, at the low energies in which NIO1 is now operating, the energy deposition by the beam on the tile is too slow to allow beam image reconstruction. The duration of the inertial calorimeter at full beam power of 8 kW is estimated to be 20 s, since the temperature is limited mainly by the thermal inertial of the tile.

The tile is held between two C-shaped metallic supports, leaving space for thermal expansion at high temperature, whose basis lays directly on the bottom part of the vessel (Figure 2.11).

Furthermore, the impinging total beam current I_b can be measured thanks to a positive voltage applied to the tile; this voltage has the double aim to cancel the perturbation due to secondary electrons emission following the beam collision with the tile. By rising the voltage, it was observed than I_b reaches a plateau, with $V \cong 50V$, which is taken as the unperturbed value of ion current I_{CFC} arriving to CFC [35].

The total H^- accelerated current can be approximated as the sum of the current measured on the PA and I_{CFC}. For this reason, the distance between the CFC tile and the PA is minimized, allowing for other diagnostic; the distance d is now 40 cm. However, after the installation of the new Extraction Grid, the nine beamlets are still not visible on the CFC tile because of the high beam divergence. In figure 2.12 an example of CFC Tile temperature measurement is shown.
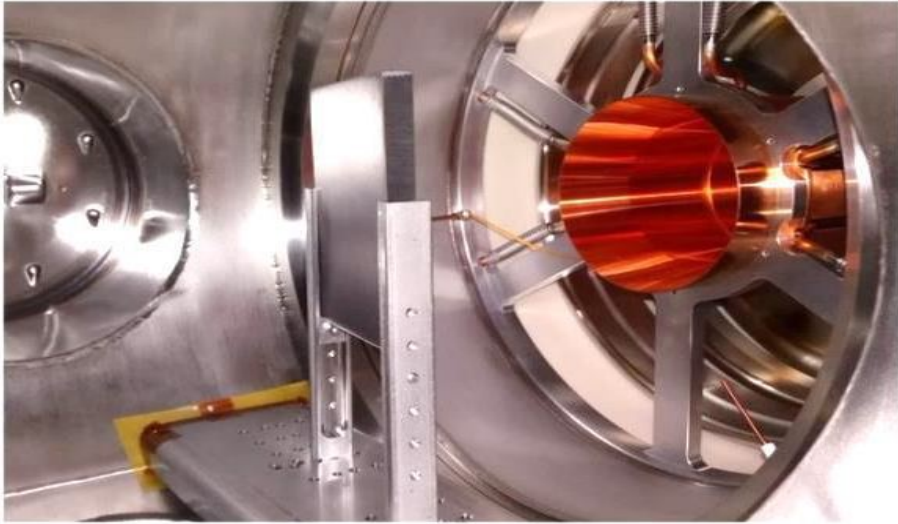
Figure 2.11: *Image of CFC tile inside the NIO1 vacuum vessel.*
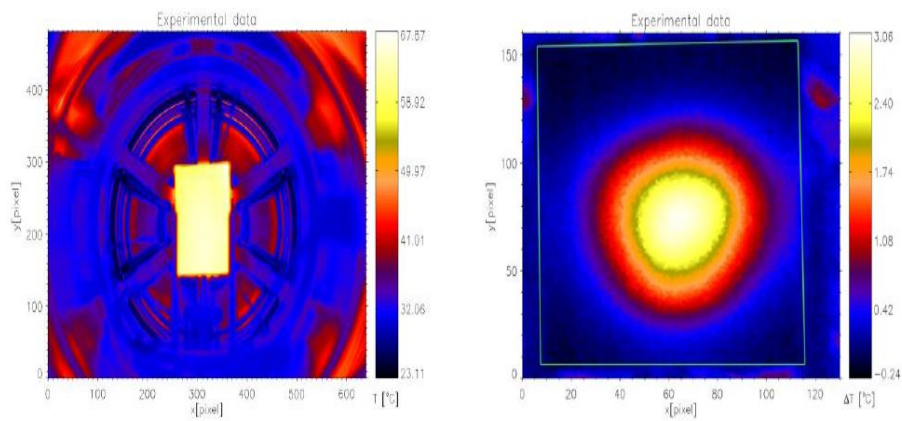
Figure 2.12: *Camera field of view (left) and a map of temperature of the tile rear surface (right).*

2.3.4 RFEA Probe

Once extracted, the beamlets travel in the drift region which is not keep in vacuum but it contains background gas with pressure usually up to some hundreds of mPa. The presence of this background gas is important for the phenomenon of *space charge compensation* [36]: the fast beam particles when interacting with the background gas produce secondary charges which can reduce the coulomb repulsion between the negative charges beamlet. NIO1 ion beam is always transported through the background plasma as it operates in steady-state, which means that the compensation time is negligible with respect to the length of the beam pulse. The four-grid Retarding Field Energy Analyzer RFEA probe placed in the proximity of the ion beam can measure the energy distribution of the particles leaving the space-charge compensation region, from which informations on the parameters of the compensating plasma can be deduced. The probe is composed by four conductive grids on which a potential can be imposed. Depending on the voltage selected, a collector collects a current due to positive ions or electrons.

The RFEA probe used in NIO1 is shown in figure 2.13. The first of the four grids is the *entrance grid*, the only grid exposed to the plasma while the others are held inside a cylindrical conductive case; the entrance grid can be kept at the same voltage as the case, at zero potential or it can be left floating. The second grid, the *plasma electron repeller*, aims to avoid electrons reaching the collector if it is held at a negative potential, the opposite when it is positively polarized to measure electrons signal. Furthermore, the fourth grid, namely the *secondary electron suppressor grid*, collect the secondary electrons eventually produced inside the RFEA. RFEA probe can also be used to collect electrons and negative ions by reversing the configuration described above.

All the grids, the collector and the RFEA case are made of stainless steel AISI304L to resist to plasma temperature. Due to the low plasma density expected, the grid entrance area is very large in order to maximize the collected currents: the RFEA case has a diameter of 18 mm and the particles reach the entrance grid by a 80 mm diameter opening [37].

2.3.5 Langmuir probe

A Langmuir probe is a device used to determine the electron temperature, electron density and electric potential of a plasma [38]. It works by inserting one or more electrodes into a plasma, with a constant or time-varying electric potential between the various electrodes or between them and the surrounding vessel. The measured currents and potential in this system allow the determination of the physical properties of the plasma. During this work of thesis an electrostatic probe is located at the bottom of the diagnostic vessel. The probe is composed by four cylindrical
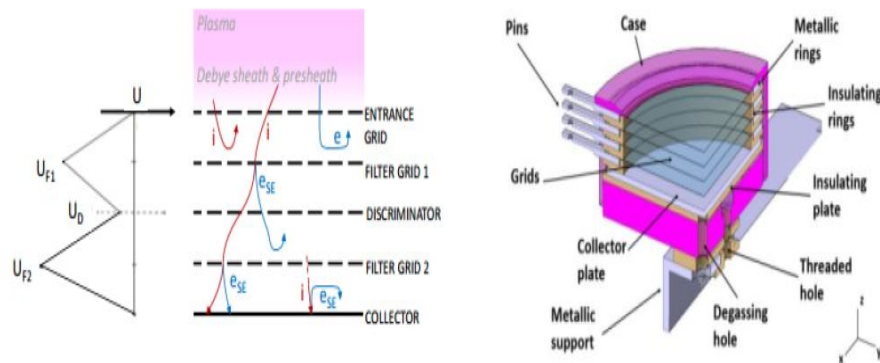
Figure 2.13: *Schematics view of the grid potential (left) and composition of NIO1 RFA.*

electrodes and two planar electrodes, as shown in figure 2.14.
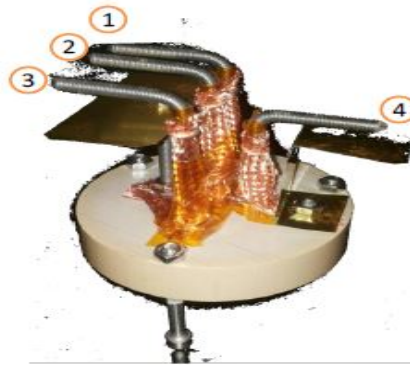
Figure 2.14: *Picture of the electrostatic probe.*

The laboratory computer was connected to the Raspberry operating system so it is possible to set the voltage output, writing the voltage in bit into a dedicated file which was stored into the Raspberry memory, using the CARS interface [39]. The Langmuir probe used during the experimental campaign is situated at almost 10 cm from the center of the beam, with 2 mm radius and 30 mm long.

2.3.6 Visible Tomography

Tomography aims at measuring the emission or the absorption of radiation through a large number of lines of sight (LOSs). Beam tomography aims at measuring beam

spatial uniformity which is found to be one of the most difficult problem to solve. In figure 2.15 the position of the two cameras observing NIO1 beamlets is shown.
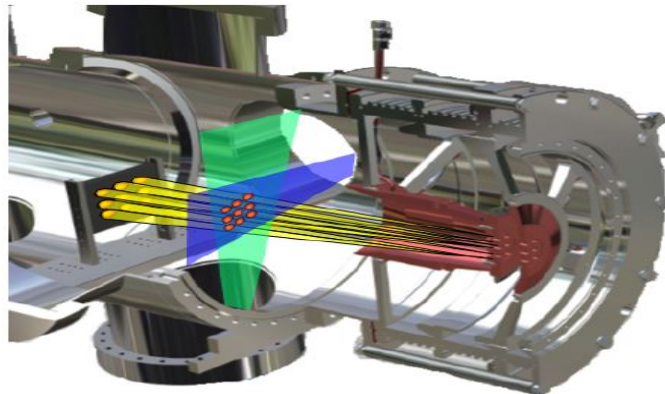
Figure 2.15: *CCD cameras in NIO1 representation.*

The two visible cameras collect the photons emitted by the H_α transition due to the beam interaction with the background gas. The cameras have high quantum efficiency at H_α wavelength and high intensity signal detected by different lines of sight. They are progressive scan CMOS, with a default resolution of 1920×1200 with pixel size of 5.86×8.86 μm and maximum frame rate of 42 fps.

An example of the two cameras 1920x1200 pixel images is shown in figure 2.16, where the three rows of beamlets are also visible.

They are a non invasive diagnostic which allow to reconstruct the two-dimensional intensity profile of the beam. Even if a complete tomography reconstruction with only two camera is not allowed, more information as possible from the data collected by these two cameras in order to reconstruct the beamlets complete configuration have been used, as it will be explained in chapter 4.
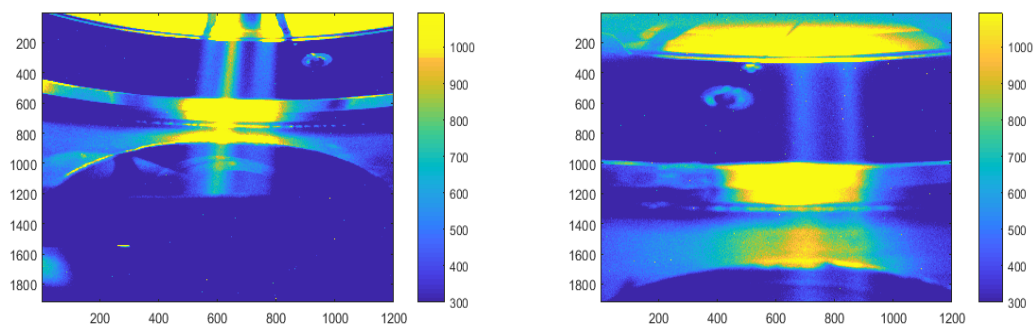
Figure 2.16: *Example of images collected by the inferior camera (left) and lateral camera (right).*

2.3.7 Cavity Ring-Down system

Cavity ring-down method is one of the diagnostics suitable for absolute H^- density measurements, a very useful information for the control of the source. As it can be seen in figure 2.17, the H^- ions must lie in the middle of an optical cavity composed by two high reflectivity plano-concave mirrors. The light pulse emitted by a pulsed laser emitting at 1064 nm entering in the cavity is partially absorbed by the negative ions: each time it hits the second mirror, a small fraction of the light escapes from the cavity and its intensity is measured with a detector. The exponential decay of the light escaping the cavity is proportional on the H^- density. This diagnostic will be installed soon on NIO1.
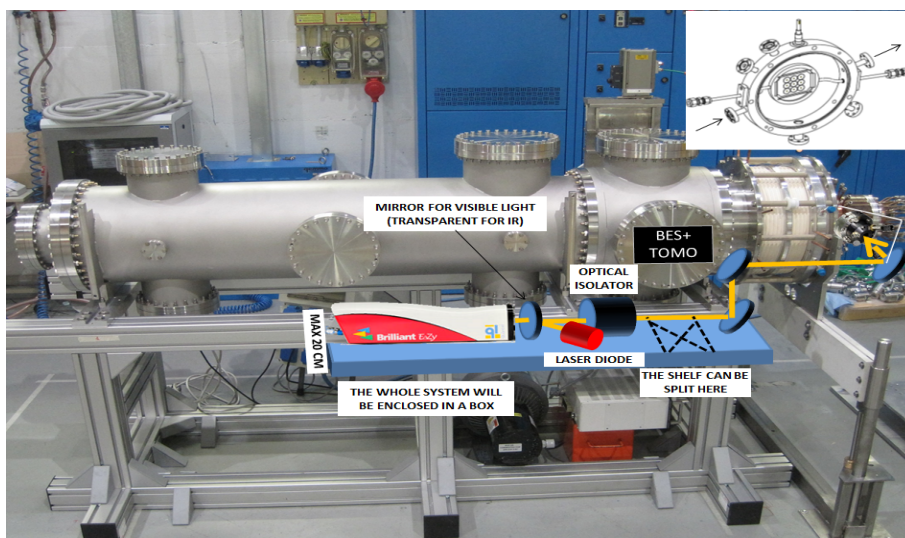
Figure 2.17: *Experimental layout proposed for the cavity ring-down spectroscopy diagnostic.*

2.4 NIO1 management and data collection

NIO1 experiment is composed by several inter-related and simultaneously operated plants, as it is shown in figure 2.18 [40]. The main components are:

- *RF Power Supply (RFPS).* To generate the plasma in the source. It has a frequency of 2 $MHz \pm 10\%$ and it ranges from 0 to 2500 W.

- *High voltage power supplies.* They allow the negative ion extraction and acceleration, respectively they are the Extraction Grid Power Supply EGPS and the Accelerating Grid Power Supply AGPS.

- *Three low voltage power supplies.* They operate the potential of Plasma Grid SBPS, the Filter field Current PGFPS and the potential of Bias Plate BPPS. They aim to increase the negative ion production by changing the electric and magnetic field configuration near the Plasma Grid and the Extraction Grid.

- *Gas Injection System.* It injects the gas into the plasma source. During the period of thesis only Hydrogen was used, but also Oxygen can be injected.

- *Pumping system.* It provides the vacuum conditions during the experiment operation.

- *Cooling Plant.* It aims at cooling the power supplies and the surfaces more subjected to heat loads during NIO1 operations.

- *Control, Safety and Interlock Systems.* They respectively deal with managing the whole system, protecting the operators and the components of the device in case of unexpected conditions.

- *Data Acquisition System.* It acquires and stores the measured data and it will be described in the next section.

2.4.1   Data Acquisition System

In NIO1 control and data acquisition system development some requirements are taken into account:

- the necessity of an easy and rapid integration of new hardware acquisition components;

- the possibility of having a single human-machine interface to monitor, configure and acquire data from the experiment;

- the visualization of acquired data and on-line elaboration during experimental session;

- the possibility of storing plant system configuration data, acquired data and post elaborated data in a single database.

To obtain all these achievements, the choice to adopt the LabVIEW framework and MDSplus software tools was made. The NIO1 data acquisition system adopts the MDSplus interface with LabVIEW and the MDSplus extension for long pulse experiment [41]. The MDSplus LabVIEW interface library allows to store all the
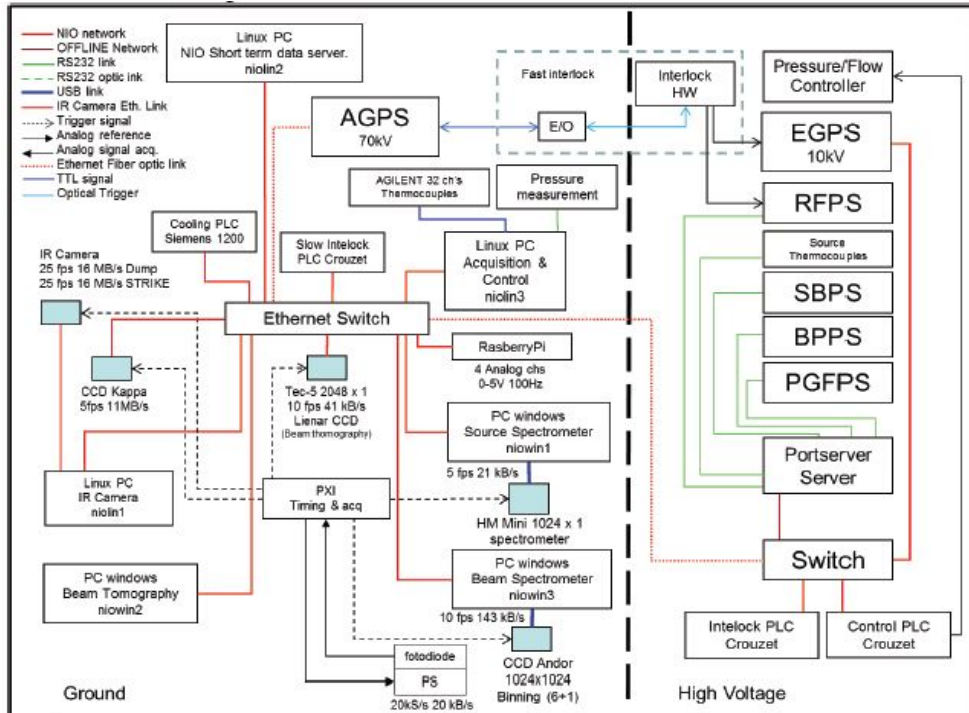
Figure 2.18: *NIO1 components.*

measured data into the MDSplus database. Here, the configuration parameters, data acquired and post elaboration data are stored in so called pulse file. One MDSplus pulse file per experimental day is created, where acquired data and set up parameters are stored as signals tagged with absolute time.

In order to be able to perform parametric searches among the big amount of stored data produced during NIO1 experimental days, a relational summary database was developed. The PostgreSQL server [42] was chosen. It satisfies all main requirements, such as the flexibility and the possibility of using keywords to indicate date and time referenced data. One of the most positive achievements of this data stored choice is the possibility of indicating by one single number, the dataset number, all the parameters and results saved for a single data acquisition. Thanks to an easy-to-read Graphical User Interface (GUI) created for Excel exploiting a PostreSQL query it is possible to easily obtain the experimental data from the database arranging them in Excel sheet columns.

During the period of thesis, one of the main goal has been the analysis of the data collected during the experimental days. In the following sections, the different kind of *scans* that have been made are reported, with a brief description of the results and a first interpretation of data collected by the different diagnostics.

Chapter 3

Experimental data analysis

In this chapter the main sets of experimental data will be shown and described in a qualitative way in view of data analysis by beam tomography and interpretation by Particle-In-Cell (PIC) simulations in the next chapters.

3.0.2 Main NIO1 parameters

Before introducing the scans, it is important to summarize how many and which are the main NIO1 parameters than can been changed. As introduced before, the two high voltage power supplies AGPS and EGPS are fundamental in defining the beam characteristics. In figure 3.1 a schematic view of NIO1 grids power supply is shown: the AGPS determines the total energy of the extracted beam.
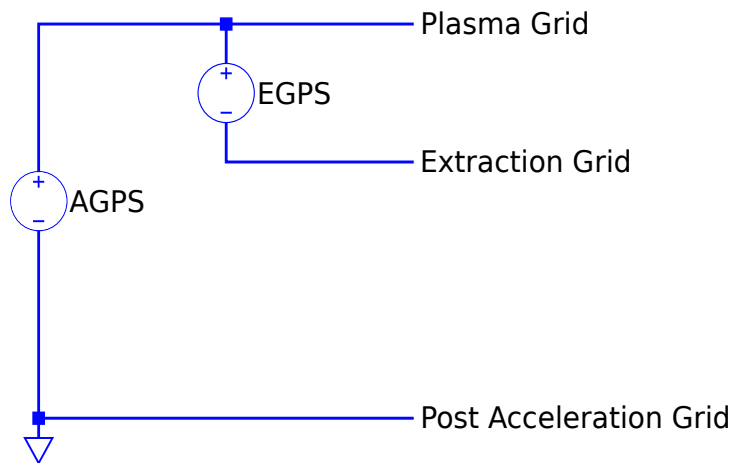
Figure 3.1: *NIO1 power supply schematic circuit.*

The EGPS polarizes the Extraction Grid which extracts the negative ions produced in the source through the Plasma Grid apertures. The current beam density

depends mainly on the negative ion density at the plasma *meniscus*, namely the ideal surface between the plasma region close to the PG and the ion beam region. A useful parameter used to determine the optics between the PG and the EG is the *perveance*, defined as

$$P = \frac{I_{extr}}{V_{extr}^{3/2}}, \tag{3.1}$$

where the I_{extr} is the extracted current which can be considered as the weighted sum of the current measured by the post acceleration grid PA and by the extraction grid EG (the EG current is mainly due to electrons impinging on the grid). The perveance is often normalized with respect to the Child-Langmuir law, which can determine the current extracted through a circular aperture with radius R as function af the system perveance:

$$I_{CL} = \frac{4}{9}\pi\epsilon_0\sqrt{\frac{2eZ}{m_{ion}}}(R/d_{grids})^2 V_{extr}^{3/2} = P_{CL}V_{extr}^{3/2}. \tag{3.2}$$

where d_{grids} is the distance between the grids [43]. Through its dependence on the ion mass ($P_0 \propto m^{-1/2}$), the perveance depends on the isotope used and on the extracted current. However the final beam divergence depends on the whole grid acceleration configuration. For this reason, both AGPS and EGPS voltage are fundamental in determining the beam intensity and divergence, as it will be shown in the following.
Not only the acceleration column plays a primary role in the determination of beam development: the state of the plasma source, governed mostly by the RF power and by source pressure is also fundamental in the characterization of the extracted beam.

Inside the RF source, the electrons are subjected both to static magnetic field and to RF electric and magnetic field, the latter with angular frequency determined by the generator frequency f, $\omega = 2\pi f$. In addiction to this, the electrons are also subjected to collisions, depending on their energy and on the gas density. The plasma luminosity depends directly on the RF power and also depends linearly on the electron density.
Once the negative ions are produced they have to reach the apertures of the Plasma Grid to be extracted. Because of the low electron affinity of the hydrogen, electrons with energy larger than 10 eV can easily destroy the negative ions so the magnetic filter in the vicinity of the PG aims to decrease electron temperature in order to avoid ion neutralization. The plasma filter magnetic field is then another important parameter which can be controlled in order to modify the current extracted and the quantity of electrons co-extracted.
The plasma source pressure plays anyway an important role, mainly regarding

the quantity of particles co-extracted through the plasma grid by the extraction grid. The pressure of the background gas between the grid must be kept as low as possible in order to avoid electron stripping process. For this reason the pressure inside the source is usually kept low, furthermore to avoid a high thermal load on the grids and plasma-facing source components. After the extraction, the beam ions interact with the background gas in the drift tube and in the diagnostic vessel. The vessel pressure depends on the source pressure and on the conductance of the grids. One way to control the vessel pressure is by using the cryogenic pumps.

To conclude, the configuration of the magnetic fields inside the acceleration column can be changed with consequent changes in the beam configuration. As said before, a variable magnetic field is the plasma filter, which is current controlled. In addition to this, NIO1 electrostatic configuration in the extraction zone can be changed by biasing the Plasma Grid and the Bias Plate at higher potential with respect to the source body. In NIO1 it is possible to polarize the Bias Plate with respect to the PG or with respect to the source body; in figure 3.2 the two different configurations are shown. The parameter that can be controlled is the current supplied by the generator connected to the bias plate I_{BB}, keeping the plasma grid at 45 V with respect to the source body, in order to take into account the effect on the polarization of the BP only. By changing the I_{BB} current the potential difference between the PG and the BP also changes in a non-linear way, probably due to a diode effect. As it will be shown in the following, the biasing of the PG with respect to the source body increases the negative ion extracted current, while the co-extracted electronic current decreases.
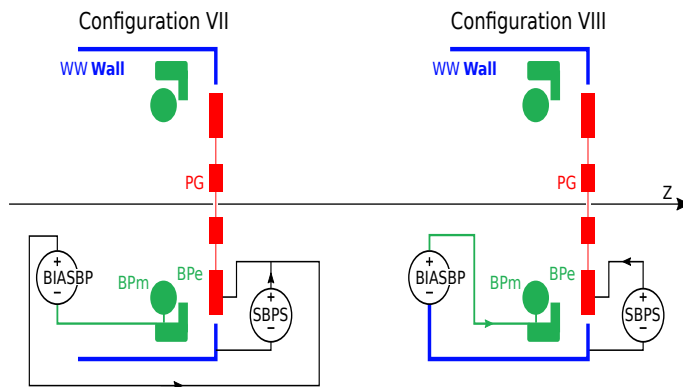
Figure 3.2: *Sketch of PG and BP electrical configuration.*

In the following sections different sets of experimental data when one of these parameters was changed are shown. The results of the different experimental campaigns are analyzed and compared through the analysis by a MATLAB software.

3.1 Scan in AGPS Voltage (V_{AGPS})

Consider the scan inV_{AGPS}, namely the voltage between the Plasma Grid (PG) and the Post Acceleration Grid (PA), which determines the beam acceleration and energy. In figure 3.3 are reported the most representative currents measured during NIO1 operation.
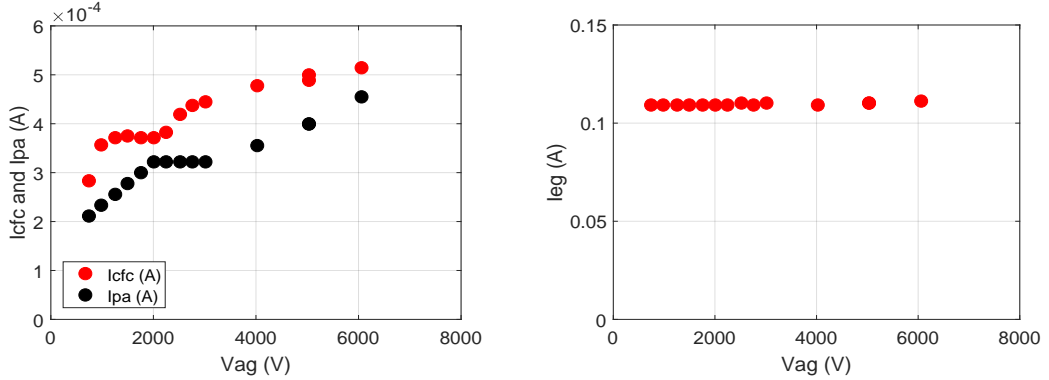
Figure 3.3: *CFC, PA and EG currents as a function of V_{AGPS}. The data refer to: 08/11/2017 V_{EGPS}=300 V, P=0.75 Pa, I_{PGF}=10 A, RF=1.1 kW, I_{BB}=0.1 A, Bias PG=45 V, cryo off.*

The CFC current represents the quantity of negatively charged particles arriving to the CFC detector, the PA current represents the ions lost against the PA and partly the electrons which are stripped between the EG and the PA. The EG current is the current measured on the extraction grid, composed mostly on co-extracted electrons which are deflected onto the EG by the magnetic fields. In the caption of figure 3.3 the main operative parameters of samples are reported, where V_{EGPS} refers to the extraction voltage, namely the voltage between PG and the EG, P refers to the source pressure, I_{PGF} refers to the plasma grid magnetic filter current, RF refers to the RF power of the RF generator, I_{BB} refers to the current of the BP and Bias PG refers to the potential different between the PG and the BP. The RF power value indicated corresponds to the direct RF power generated by the RF power supplies; during NIO1 operations indeed the amount of RF power reflected by the plasma is negligible. In these data an increase in CFC and PA currents with the increasing AGPS voltage is evident. In particular, a sort of plateau in the I_{PA} current can be identified in the range of AGPS voltage between 2000 and 3000 V. In this range of energy instead the I_{CFC} continues to raise. This could be an indication of an optimum of beam optics, resulting in a reduction of losses on the PA. By analyzing the data collected by the other diagnostics this will be confirmed. This will be shown in the following and it will be

confirmed by tomography reconstruction in the chapter 4. The I_{EG} instead does not increase since the quantity of electrons extracted does not depend on the acceleration voltage. However, the current collected by the EG is almost three orders of magnitude higher than the beam currents, with consequently high load of heat on the extraction grid. More information can be obtained by the analysis of BES and visible cameras data. Qualitative information can be achieved from the comparison of BES integrals, namely the integral of the Doppler peak, representing the amount of negative ions accelerated, and the stripping integral, representing the amount of electron stripping produced by the interactions of the accelerated ions on the background gas. BES data analysis is made with an IDL software, which also calculates the full width half maximum (FWHM) of the Doppler peak; this width can be easily compared with a more complete divergence calculated by the equation 2.3.
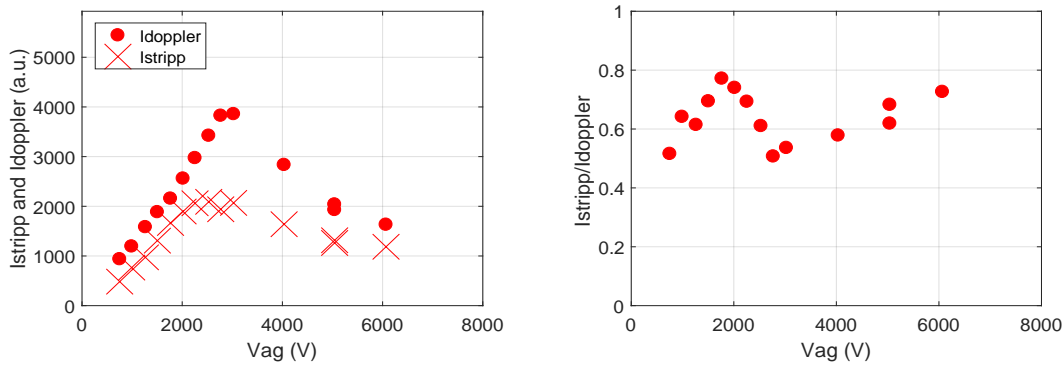
Figure 3.4: *Doppler and stripping integral and their ratio as a function of V_{AGPS}. The data refer to: 08/11/2017 V_{EGPS}=300 V, P=0.75 Pa, I_{PGF}=10 A, RF=1.1 kW, I_{BB}=0.1 A, Bias PG=45 V, cryo off.*

In figure 3.4 Doppler and stripping integral and their ratio are shown. It is evident that, after an initial increase of both the quantities, between 2000 and 3000 V, the stripping integral remains almost constant while the Doppler integral increases. This is more highlighted in the ratio between these two quantities, where a minimum is present for V_{AGPS}=2750 V. It represents an optimum for the beam optics.

This beam optics improvement is also confirmed in figure 3.5. Here, the evolution of the FWHM and divergence of the Doppler peak is reported, where a similar trend is evident. Both quantities show a minimum close to the optimal value previously identified, corresponding to a beam divergence just above 30 mrad. At lowering V_{AGPS} values, the two curves are quite different: the FWHM appears to saturate while the divergence is not. This is probably due to different term in
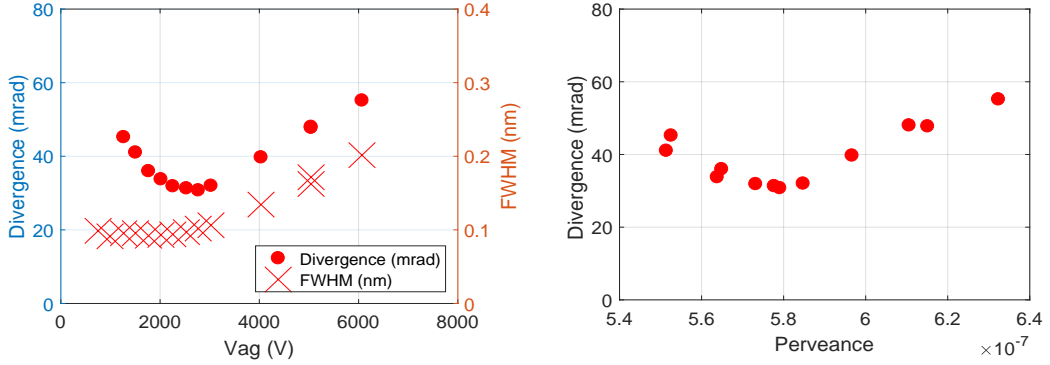
Figure 3.5: *Comparison between peak FWHM and divergence and divergence as a function of perveance when varying V_{AGPS}. The data refer to: 08/11/2017 V_{EGPS}=300 V, P=0.75 Pa, I_{PGF}=10 A, RF=1.1 kW, I_{BB}=0.1 A, Bias PG=45 V, cryo off.*

equation 2.3 which becomes dominant. Finally, the divergence as a function of perveance is reported which confirms previous results.

The beam evolution just described, is also visible in the data collected by the two optical cameras. In figure 3.6 the data collected by the two cameras during this scan are reported. The average values of the image pixel region in which the beamlets are more visible for different V_{AGPS} values are displayed. The pictures are quite different for two reasons. Firstly the images collected by the lateral camera (right pictures) have a double width with respect to the bottom camera (left pictures) in pixel unity. In addition to this, because of the orientation of the permanent magnets in the EG, NIO1 beam particles are deflected in the vertical direction: the right and the left beamlet columns are deflected upward while the central one is deflected downward. The top charts in figure 3.6 show the increase of the signal collected as V_{AGPS} increases. Once the optimal value is exceeded, the images become worse and the beamlets are no longer distinguishable, as shown in the bottom charts. Close to the optimal optics, it is possible to fit with three Gaussians plus a background one the data collected by the bottom camera, because they are not influenced by the magnetic deflection. One example is reported in figure 3.7, where the evolution of the distance between the peaks and the sigma value as function of V_{AGPS} are also reported.

The positions of the beamlet peaks show how the lateral rows approach to the central one as V_{AGPS} increases, showing a better beamlets alignment. Also in the sigma evolution, a minimum for all of them can be identified as V_{AGPS} gets closer to the optical optimum, before starting to grow again. In addition to this, the sigma of the central row of beamlets results to be smaller than the other two.
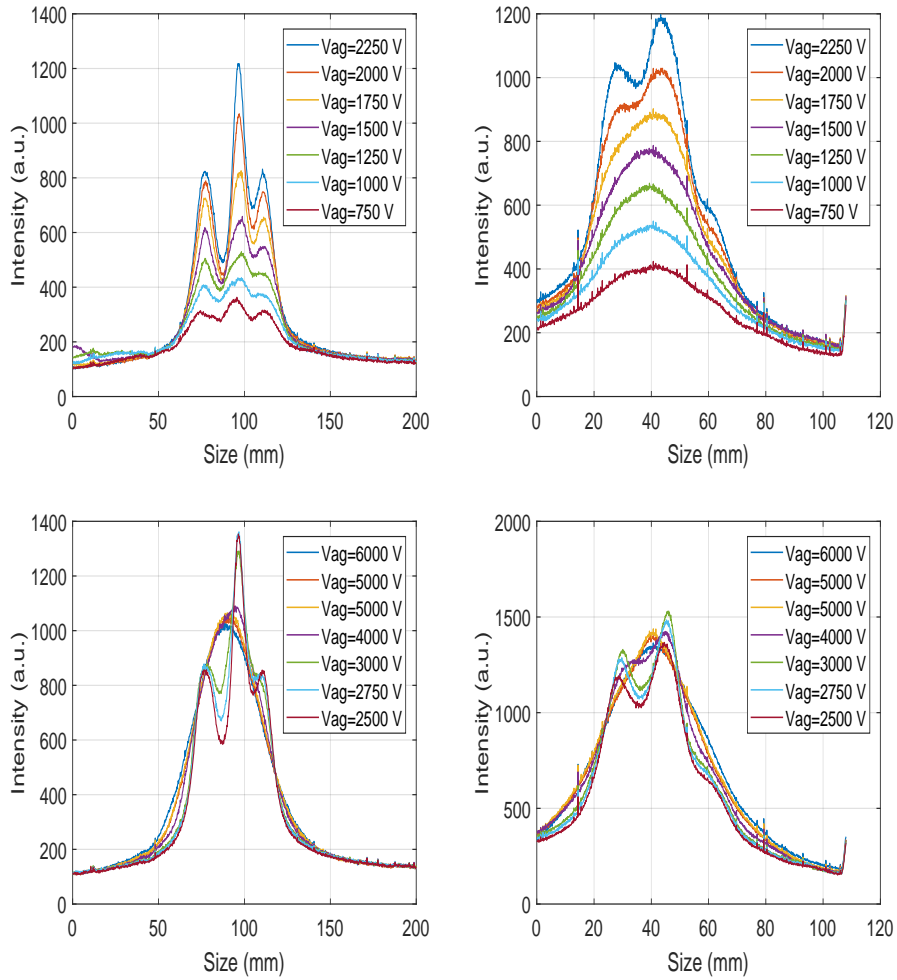
Figure 3.6: *Comparison between a section of the images collected by the two cameras as a function of V_{AGPS}. The data refer to: 08/11/2017 V_{EGPS}=300 V, P=0.75 Pa, I_{PGF}=10 A, RF=1.1 kW, I_{BB}=0.1 A, Bias PG=45 V, cryo off.*
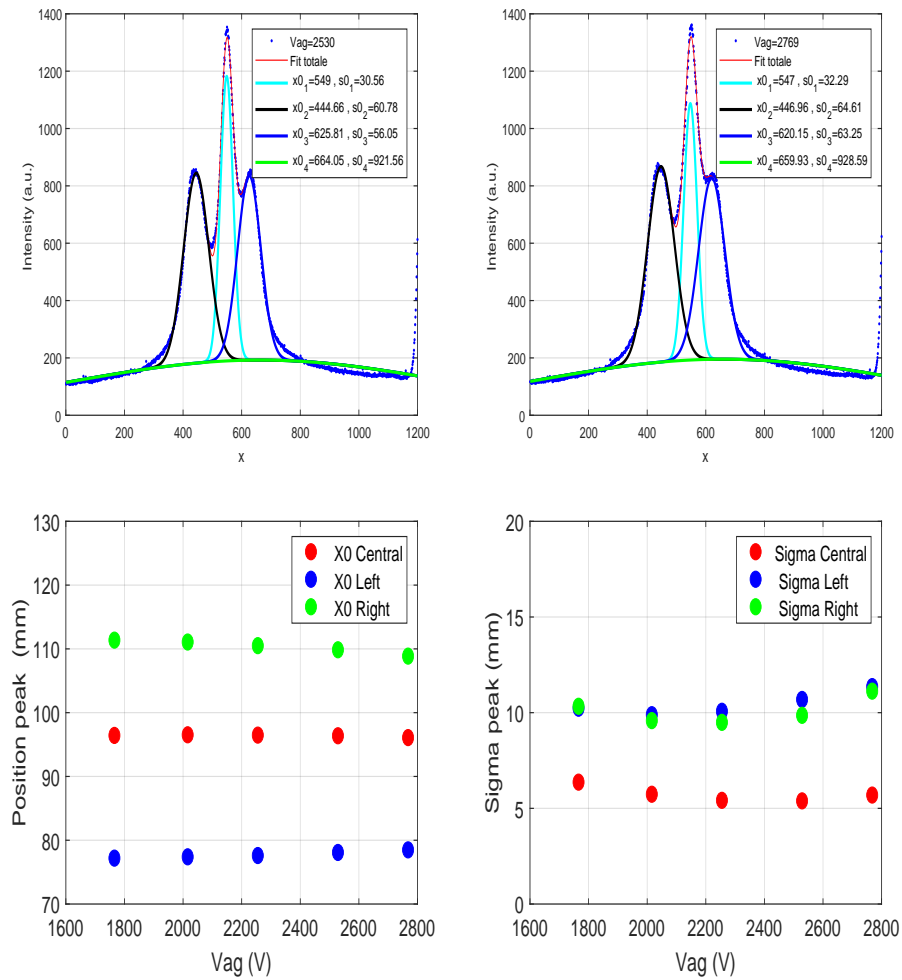
Figure 3.7: *Some 3 Gaussians fit examples and x0 and sigma evolution as a function of V_{AGPS}. The data refer to: 08/11/2017 V_{EGPS}=300 V, P=0.75 Pa, I_{PGF}=10 A, RF=1.1 kW, I_{BB}=0.1 A, Bias PG=45 V, cryo off.*

Other examples of V_{AGPS} scans are reported in Appendix A.

3.2   Scan in EGPS Voltage (V_{EGPS})

In this section some scans in extraction voltage EGPS from which depends the extracted current from the source are reported . In figure 3.8 a scan in V_{EGPS} for a value of V_{AGPS} close to the optimal value identified earlier is reported.
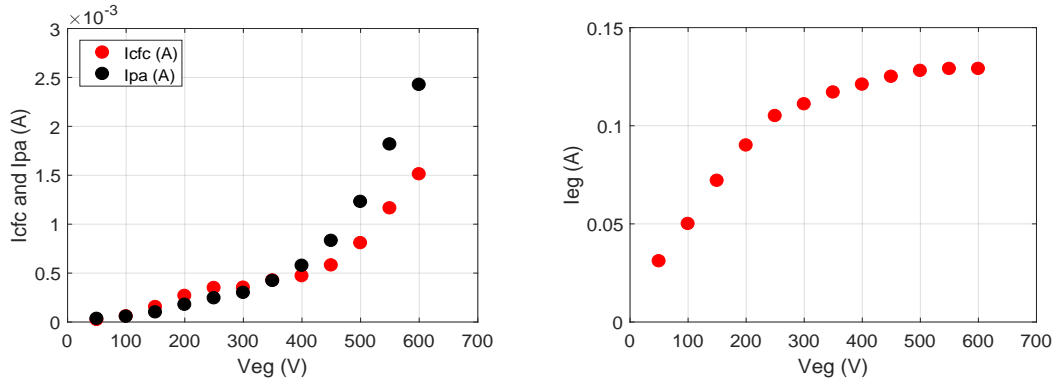
Figure 3.8: *CFC, PA and EG currents as a function of EGPS. The data refer to: 08/11/2017 V_{AGPS}=2 kV, P=0.75 Pa, I_{PGF}=10 A, RF=1.1 kW, I_{BB}=0.1 A, Bias PG=45 V, cryo off.*

The V_{EGPS} is responsible for the amount of ions extracted from the source. As a consequence, also the quantity of co-extracted electrons depends on this voltage. This is well visible in figure 3.8 where the I_{EG} current increases with V_{EGPS} in an almost linear way. This follows from the equation 3.2: a dependence proportional to $V_{extr}^{3/2}$ is expected, even if it is not clearly distinguishable due to the leak of points in this region. However, for the same reason the equivalent rise in PA and CFC currents is present, with an I_{CFC} higher than I_{PA} for values of V_{EGPS} lower than 300 V.

From BES data analysis also the increase of the Doppler peak and stripping integrals are visible. After an initial growth, a little plateau in the two values is identifiable for V_{EGPS} between 300 and 400 V. These values correspond to the minimum in FWHM and beam divergence as shown in figure 3.10.

For the beam divergence, it can be shown how the minimum shifts toward higher extraction voltage values as V_{AGPS} increases. This behavior is shown in figure 3.11, where all the beam divergences are compared, even with very different conditions.

In order to complete the analysis, the data collected by the cameras are reported in figure 3.12. In the two upper charts, the increase in the camera signals are
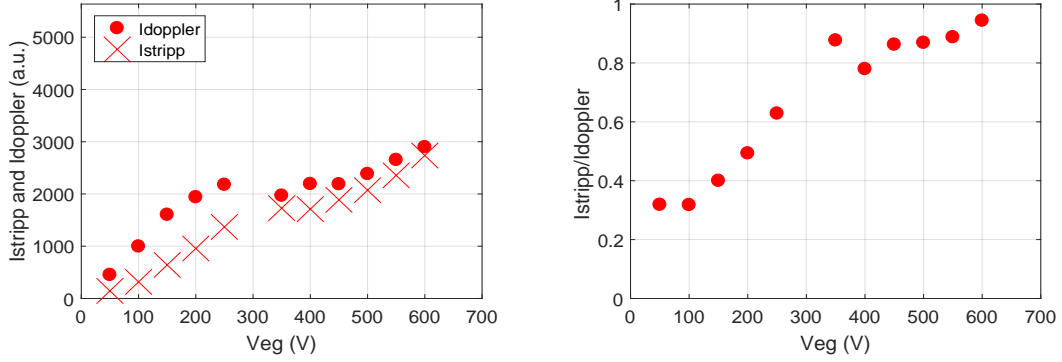
Figure 3.9: *Doppler and stripping integral and their ratio as a function of V_{EGPS}. The data refer to: 08/11/2017 V_{AGPS}=2 kV, P=0.75 Pa, I_{PGF}=10 A, RF=1.1 kW, I_{BB}=0.1 A, Bias PG=45 V, cryo off.*
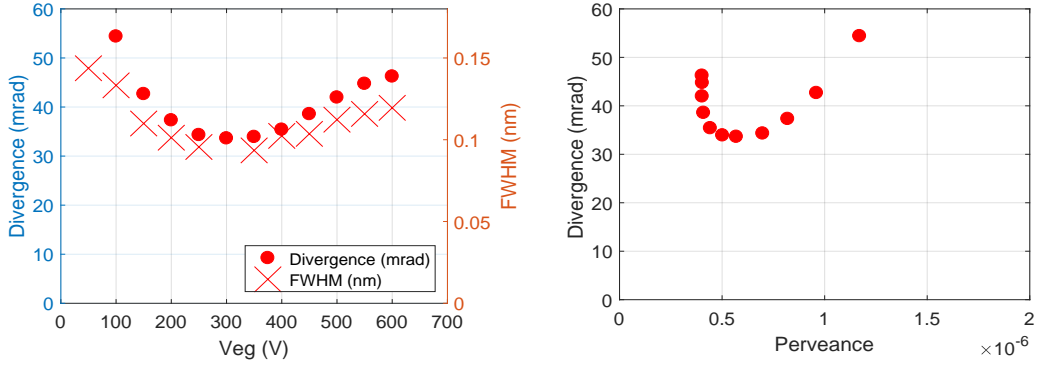
Figure 3.10: *Comparison between peak FWHM and divergence and divergence as a function of perveance when varying V_{AGPS}. The data refer to: 08/11/2017 V_{EGPS}=2 kV, P=0.75 Pa, I_{PGF}=10 A, RF=1.1 kW, I_{BB}=0.1 A, Bias PG=45 V, cryo off.*

evident. In particular, one can see how the signal reaches an optimum where the three rows of peaks are clear distinguishable in the bottom camera before getting worse. The bottom charts show some qualitative information about the amount of signal collected by the cameras. The integral of the curve reported in the upper charts is plotted, which increases with increasing V_{EGPS} as expected. In addition to this, the integral can also be compared with the other diagnostics, such as the total signal collected by the BES. Even if this is just a qualitative information, an increment in both signals with V_{EGPS} is shown. This is mainly due to the increment in the amount of particles extracted, both ions and electrons, which is reflected also in the increase of the background collected by the cameras.
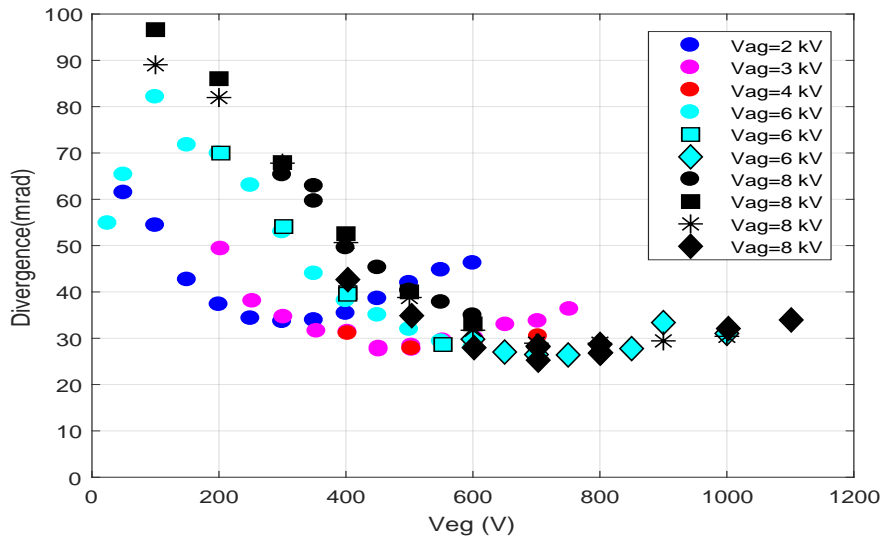
Figure 3.11: *Beam divergence summary.*

To summarize, two conditions for optics optimum have been identified. They correspond to extraction voltage between 250 and 400 V and total voltage between 2000 and 3000 V. These conditions will be analyzed in the following chapter in order to reconstruct the complete 9 beamlet configuration by means of tomography. Unfortunately, these are values very low compared to NIO1 target of accelerating ions up to an energy of 60 keV. This is in part due to the lack of cesium injector in the plasma source and probably to the not yet optimized magnetic configuration. Other V_{EGPS} scans are reported in Appendix A.
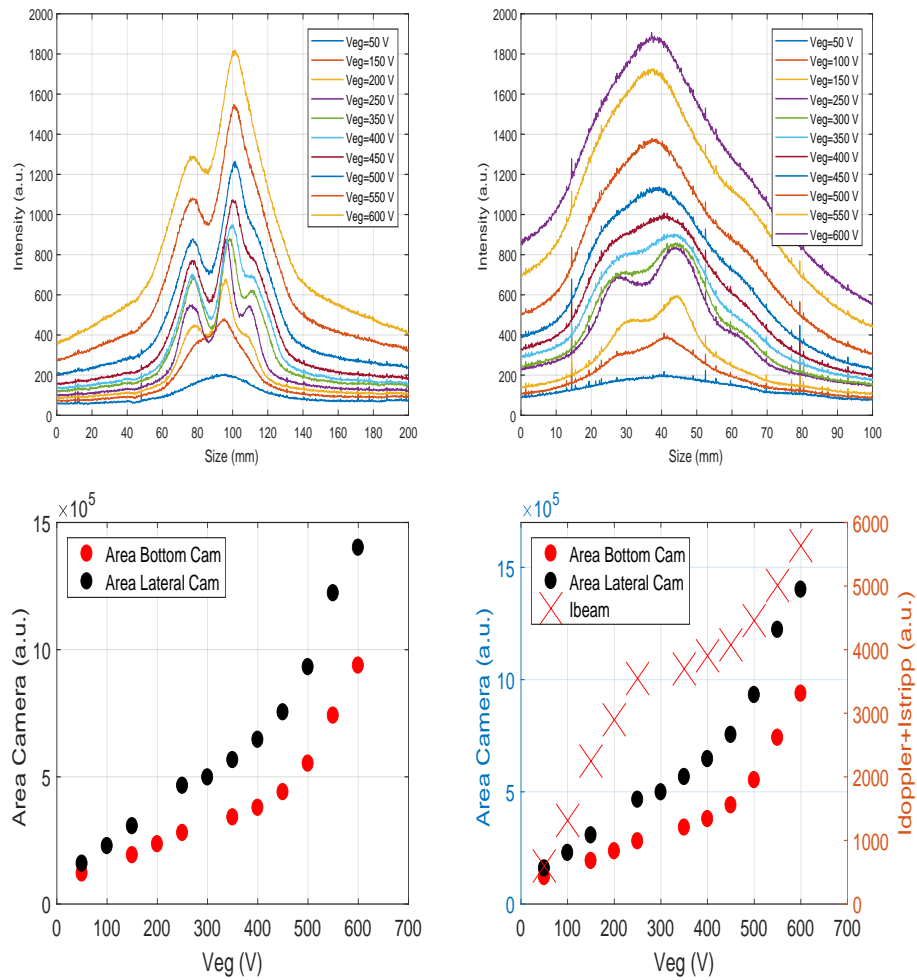
Figure 3.12: *Camera data results as a function of V_{EGPS}. The data refer to: 08/11/2017 V_{AGPS}=2 kV, P=0.75 Pa, I_{PGF}=10 A, RF=1.1 kW, I_{BB}=0.1 A, Bias PG=45 V, cryo off.*

3.3 Scan in source pressure

In addition to varying the acceleration and extraction energies, also changes in source pressure reflect in the extracted ion current.

A comparison between two scans in pressure at different V_{EGPS} and V_{AGPS} will be discussed. In particular, a condition close to the optimum optics value found before will be compared with higher extraction and acceleration energies.
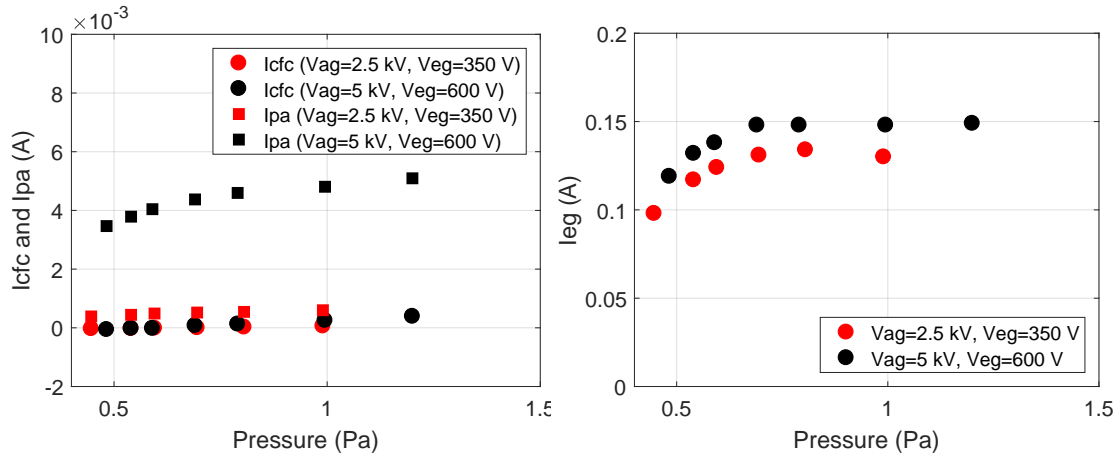
Figure 3.13: *CFC, PA and EG currents as a function of pressure. The data refer to: 06/02/2018 V_{AGPS}=2.5-5 kV, V_{EGPS}=350-600 V, I_{PGF}=10 A, RF=1.2 kW, I_{BB}=0.2 A, Bias PG=45 V, $V_{CFC} = V_{REP}$=0.8 V, cryo off.*

The data reported in figure 3.13 were collected with Repeller and CFC tile grounded. This reflects in the zero or slightly positive current measured by the CFC, due to its electron loss following beam impact. Concerning the other currents measured, the main difference is due to the different range of energies at which the data were collected. The dependence in pressure variation instead is evident in both the currents which increases as V_{EGPS} increasing.

Analogously to the currents, also in the data collected by the BES a difference between the two energetic ranges is presented.
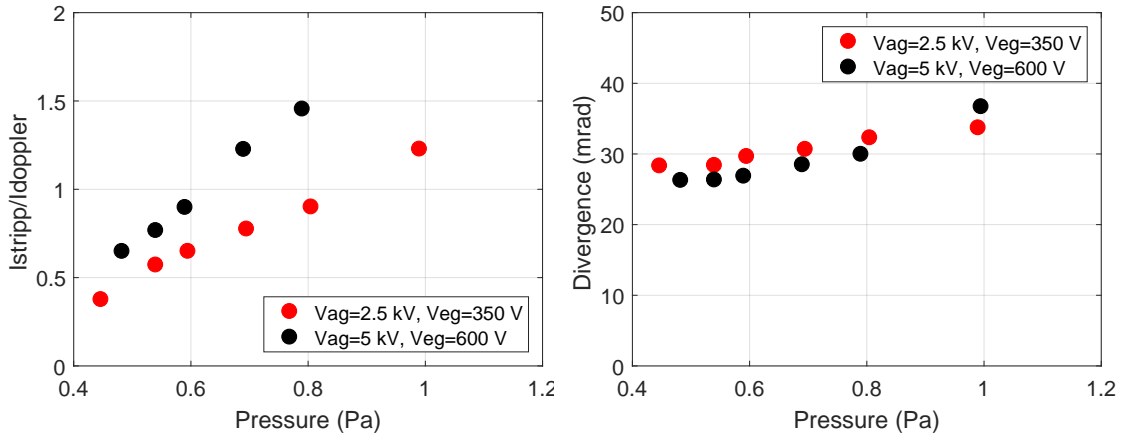
Figure 3.14: *Doppler and stripping integral ratio and beam divergence as a function of pressure. The data refer to: 06/02/2018 V_{AGPS}=2.5-5 kV, V_{EGPS}=350-600 V, I_{PGF}=10 A, RF=1.2 kW, I_{BB}=0.2 A, Bias PG=45 V, $V_{CFC} = V_{REP}$=0.8 V, cryo off.*

In both cases, with the increasing pressure the stripping growth is conspicuous: for higher pressure values it exceeds the quantity of Doppler peak integral measured. Concerning the beam divergence, an increase of about the 30 % as the pressure increases is shown if figure 3.14. Finally, in figure 3.15 the data collected by the cameras are reported. Also in this data, an increment in the integral with the increasing pressure is shown. Here the two different beam optics conditions are also evident. The data collected at lower energies (left side) show in a clearer way the presence of the three rows of beamlets, which are instead less evident at higher energies (right side).
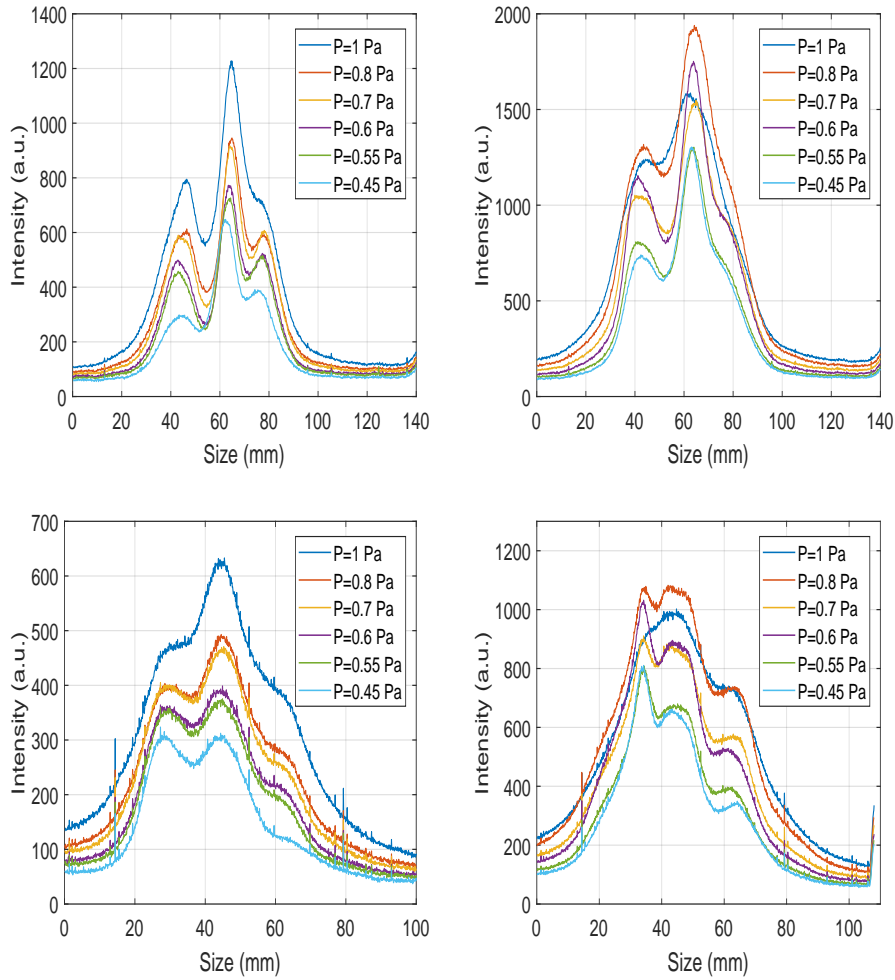
Figure 3.15: *Camera data results as a function of pressure. The data refer to: 06/02/2018 V_{AGPS}=2.5-5 kV, V_{EGPS}=350-600 V, I_{PGF}=10 A, RF=1.2 kW, I_{BB}=0.2 A, Bias PG=45 V, $V_{CFC} = V_{REP}$=0.8 V, cryo off.*

Another sets of experimental data collected at different pressure and with or without the cryogenic pump on are reported in the follows. These data are collected at varying of V_{AGPS}.
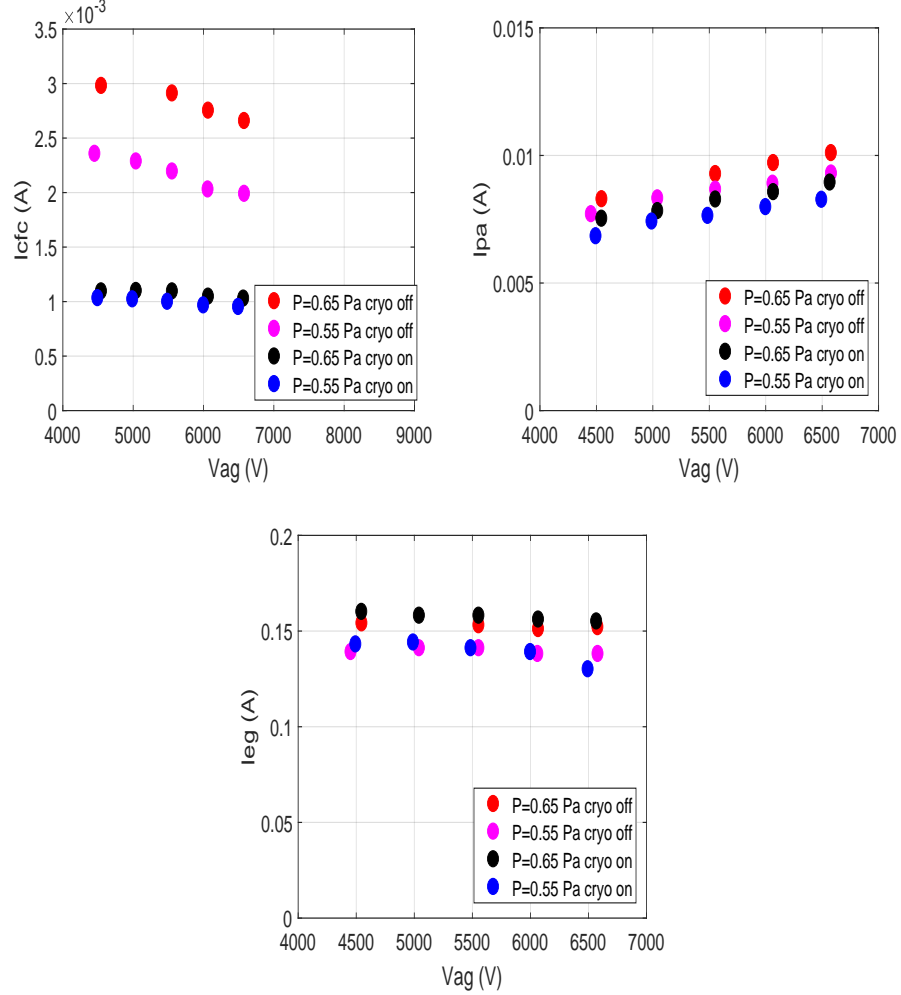
Figure 3.16: *CFC, PA and EG currents as a function of V_{AGPS} for different pressure and with/without cryo. 2017/09/14 V_{EGPS}=500 V, P=0.6 Pa, I_{PGF}=200 A, RF=1.2 kW, I_{BB}=0.3 A, Bias PG=45 V, with and without cryo; 2017/09/19 V_{EGPS}=500 V, P=0.65 Pa, I_{PGF}=200 A, RF=1.2 kW, I_{BB}=0.2 A, Bias PG=20 V, with and without cryo.*

In figure 3.16 CFC, PA and EG currents as functions of V_{AGPS} for different pressure and with or without the cryogenic pumps on are shown. One can see that the magnetic conditions are quite different. As expected, as the pressure increases, the measured current increases. The dependence on the V_{AGPS} rising

is not so relevant, although with the increase of V_{AGPS}, in CFC and PA currents a trend can be seen. The effect of the cryogenics is clear mostly in the CFC current, with a decrease of about 40% when the cryogenics is on; this decrease is mainly due to the difference in the vessel pressure, which varies by a factor of 10 with or without cryogenics; for the EG current, the main difference is due to the change in the source pressure, while the effect of cryogenics and the varying in V_{AGPS} is less relevant. When the cryogenic pumps are on, the pressure in the first acceleration grid gap decreases less with respect to the vessel pressure decrease. Even if the quantity of secondary electrons decreases when the cryogenic is on, the amount of electron co-extracted does not vary at all. For this reason, the only effect which is reflected in the I_{EG} measurements are the differences in the source pressure. Regarding the Beam Emission Spectroscopy (BES), in figure 3.17 the ratio between the integral of the stripping and the intensity of the Doppler peak is shown, where the effect of the cryogenics is considerable, with a decrease in the ratio larger than a factor of 2.5; for the beam divergence instead, also shown in figure 3.17, one can see a sort of minimum for 4 kV of acceleration; the effects of cryogenics and of the change in pressure appear less relevant, even if they are present.
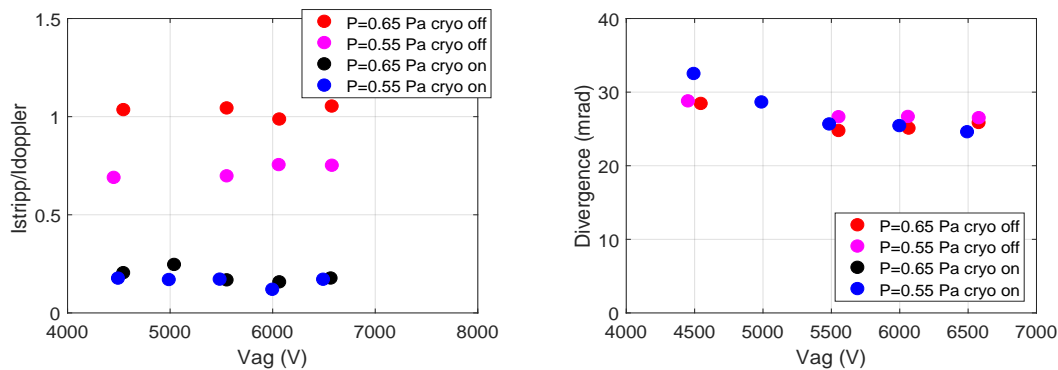
Figure 3.17: $I_{STRIPP}/I_{DOPPLER}$ and beam divergence as a function of V_{AGPS} for different pressure and with/without cryo. 2017/09/14 V_{EGPS}=500 V, P=0.6 Pa, I_{PGF}=200 A, RF=1.2 kW, I_{BB}=0.3 A, Bias PG=45 V, with and without cryo; 2017/09/19 V_{EGPS}=500 V, P=0.65 Pa, I_{PGF}=200 A, RF=1.2 kW, I_{BB}=0.2 A, Bias PG=20 V, with and without cryo.

A scan in pressure is therefore more significant for other diagnostics, like the Langmuir and RFEA probes. In the chapter 5, a comparison between the data collected by these two electrostatic probes and the PIC simulation results will be proposed.

3.4 Other scans

A set of experimental data in which the configuration of the whole magnetic field the region where the beamlets are extracted and accelerated has been varied is presented. The parameters that can be changed are:

- The current of the Plasma Grid filter I_{PGF};

- The biasing of the Plasma Grid with respect the source walls PG Bias Voltage;

- The current which polarizes the Bias Plate with respect to the Plasma Grid I_{BB};

- The polarization of the CFC tile and the Repeller. They do not influence the beam optics directly but their effects in the amount of background particles collected by the diagnostics are evident.

A brief description of the results obtained where varying one by one these parameters follows.

3.4.1 Scan in Plasma Grid Filter Current.

As already mentioned, the magnetic filter is a variable magnetic field present in the plasma source. It aims to reduce the quantity of electrons co-extracted.
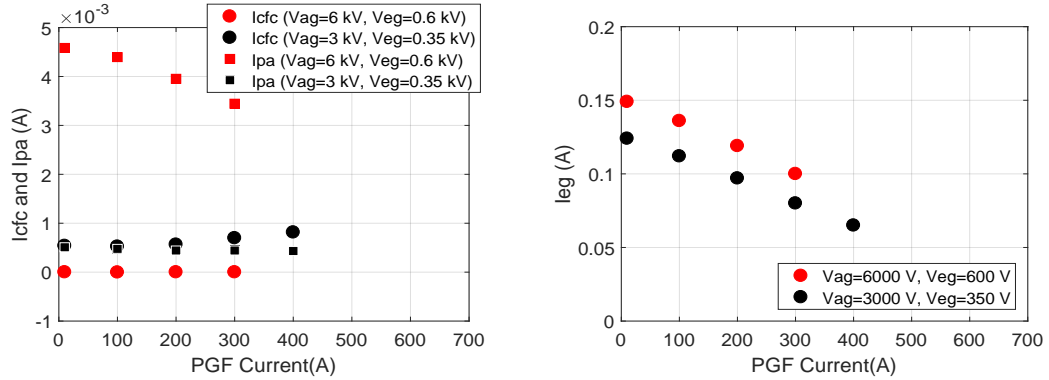
Figure 3.18: *CFC, PA and EG currents as a function of I_{PGF}. The data refer to: 10/11/2017 V_{AGPS}=3 kV, V_{EGPS}=350 V, P=0.75 Pa, RF=1.2 kW, I_{BB}=0.3 A, Bias PG=45 V, V_{CFC}=60.4 V, V_{REP}=0 V, cryo off; 23/11/2017 V_{AGPS}=6 kV, V_{EGPS}=600 V, P=0.55 Pa, RF=1.2 kW, I_{BB}=0.1 A, Bias PG=45 V, V_{CFC}=0 V, V_{REP}=60.4 V, cryo off.*

This is highlighted in figure 3.18 where the I_{EG} decreases with increasing I_{PGF}. The I_{PGF} effect appears also on the I_{CFC} and I_{PA} currents: while the I_{CFC} seems to increase with the I_{PGF} growth, the I_{PA}, mainly for the higher energy case, decreases. An useful parameter which can be used to show the effect on the currents of the I_{PGF} is the ratio between the I_{CFC} and the I_{EG}. It is shown in figure 3.19. Only the data with the CFC Tile polarized are reported. Even if the ratio is very low, it is clear the increase of the ratio between the two current as expected.
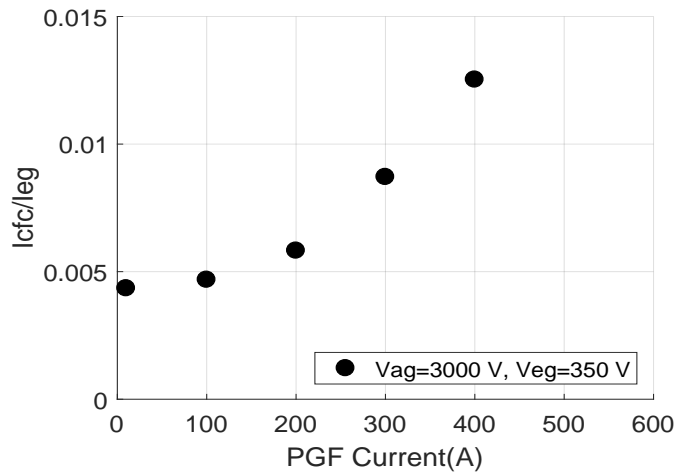
Figure 3.19: *Ratio between the CFC and EG currents as a function of I_{PGF}. The data refer to: 10/11/2017 V_{AGPS}=3 kV, V_{EGPS}=350 V, P=0.75 Pa, RF=1.2 kW, I_{BB}=0.3 A, Bias PG=45 V, V_{CFC}=60.4 V, V_{REP}=0 V, cryo off; 23/11/2017 V_{AGPS}=6 kV, V_{EGPS}=600 V, P=0.55 Pa, RF=1.2 kW, I_{BB}=0.1 A, Bias PG=45 V, V_{CFC}=0 V, V_{REP}=60.4 V, cryo off.*

This leakage decrease is also present in BES data, as shown in figure 3.20.

As I_{PGF} increases, the Doppler peak integral increases too. The stripping integral, as I_{PFG} increases but it grows less than the integral of the Doppler peak. This is shown in their ratio, which decreases at I_{PGF} raising. Unfortunately, also the beam optics depends on I_{PGF} variation: as I_{PGF} grows, the beam optics gets worse, as one can see in figure 3.21.
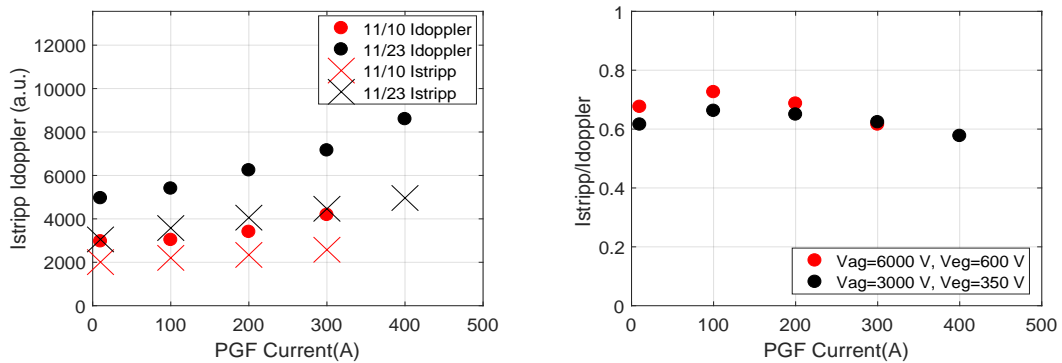
Figure 3.20: *Doppler and stripping integral and their ratio as a function of I_{PGF}. The data refer to: 10/11/2017 V_{AGPS}=3 kV, V_{EGPS}=350 V, P=0.75 Pa, RF=1.2 kW, I_{BB}=0.3 A, Bias PG=45 V, V_{CFC}=60.4 V, V_{REP}=0 V, cryo off; 23/11/2017 V_{AGPS}=6 kV, V_{EGPS}=600 V, P=0.55 Pa, RF=1.2 kW, I_{BB}=0.1 A, Bias PG=45 V, V_{CFC}=0 V, V_{REP}=60.4 V, cryo off.*
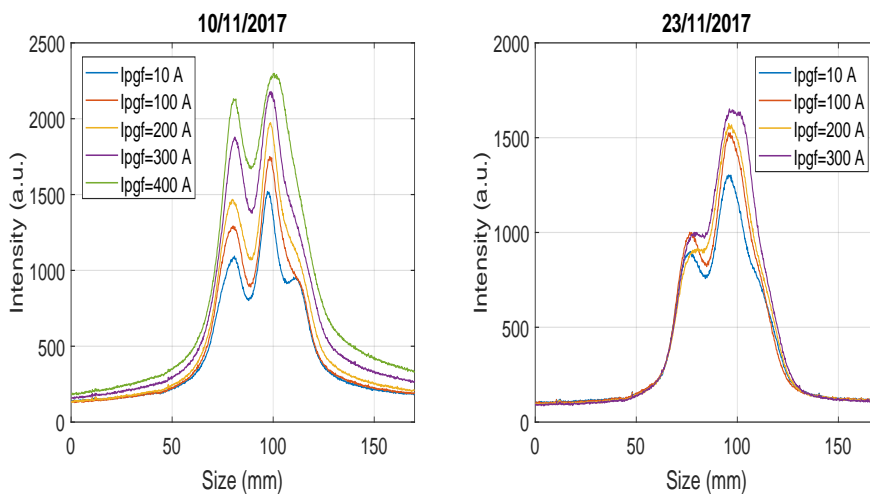
Figure 3.21: *Camera data results as a function of I_{PGF} (low energies on the left side and high energies on the right side). The data refer to: 10/11/2017 V_{AGPS}=3 kV, V_{EGPS}=350 V, P=0.75 Pa, RF=1.2 kW, I_{BB}=0.3 A, Bias PG=45 V, V_{CFC}=60.4 V, V_{REP}=0 V, cryo off; 23/11/2017 V_{AGPS}=6 kV, V_{EGPS}=600 V, P=0.55 Pa, RF=1.2 kW, I_{BB}=0.1 A, Bias PG=45 V, V_{CFC}=0 V, V_{REP}=60.4 V, cryo off.*

Even if the collected signal rises, the images get worse and for the highest I_{PGF} values, the three beamlet rows disappear. For this reason, at present it seems preferable to keep the plasma grid filter off.

3.4.2 Scan in Bias Plate Current
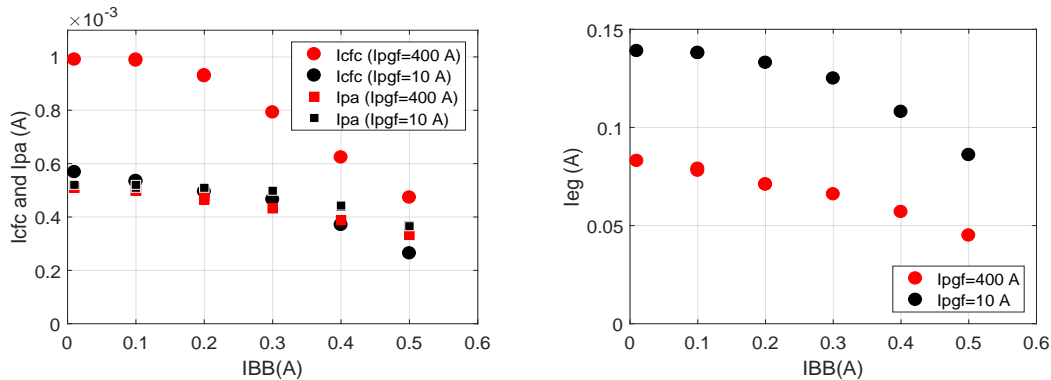
Figure 3.22: *CFC, PA and EG currents as a function of I_{BB} . The data refer to: 10/11/2017 V_{AGPS}=3 kV, V_{EGPS}=350 V, P=0.75 Pa, RF=1.2 kW, I_{PGF}=10-400 A, Bias PG=45 V, V_{CFC}=60.4 V, V_{REP}=0 V, cryo off.*

It is now useful to analyze how the polarization of the Bias Plate with respect the PG acts on the extracted negative ion current and co-extracted electrons. In NIO1, as soon as the I_{BB} current changes, the difference of potential between the PG and the BP also changes. In figure 3.22 the currents collected during two scans in I_{BB} at different I_{PGF} are reported. As soon as the I_{BB} increases it is evident how all the currents reduce, not only the two leakages but also the I_{CFC} current. This happens also in the BES data, where a decrease in the collected integrals appears as the I_{BB} rises.

In figure 3.23 the data collected by the cameras at the two different I_{PGF} values are shown. Here, the effects of both magnetic fields are evident. The data collected with the lower I_{PGF} show an initial better optics, which degenerates as the I_{BB} increases. Considering that the signals collected by the cameras get worse too, the effects of the BP plate biasing have to be deeply analyzed in order to better understand its consequences on the extracted beam current and optics.
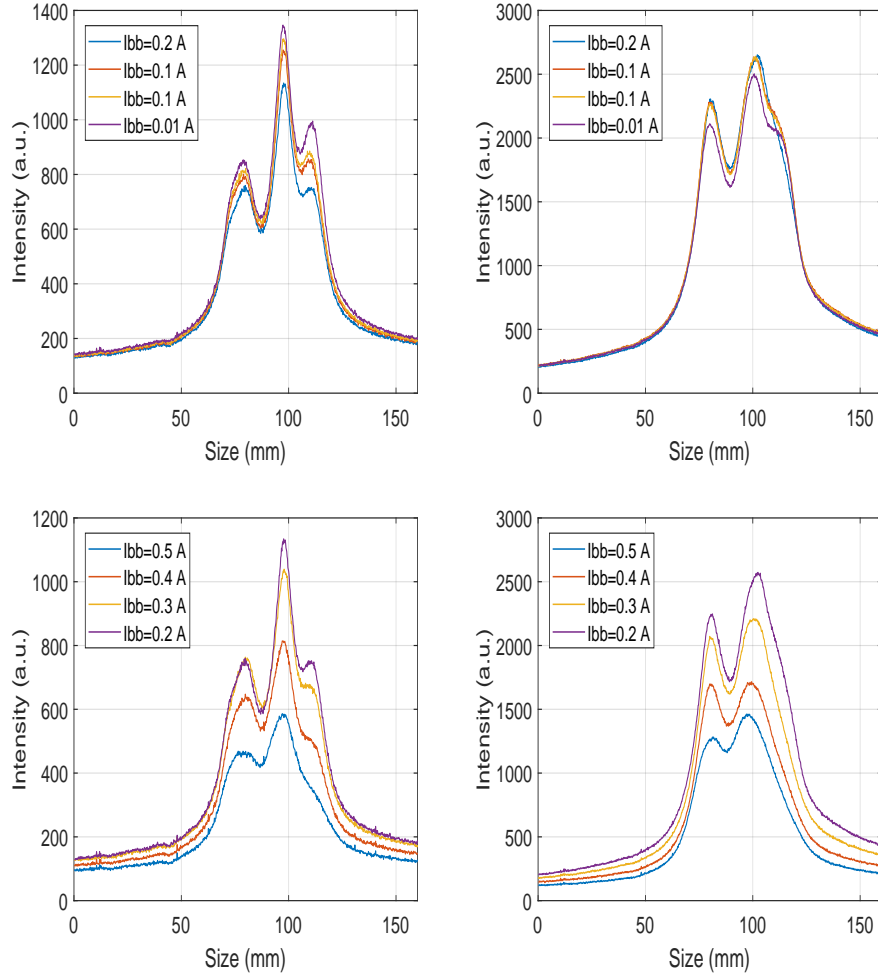
Figure 3.23: *Camera data results as a function of I_{BB}. The data were collected with I_{PGF}=10 A (left side) and 400 A (right side). The data refer to: 10/11/2017 V_{AGPS}=3 kV, V_{EGPS}=350 V, P=0.75 Pa, RF=1.2 kW, I_{PGF}=10-400 A, Bias PG=45 V, V_{CFC}=60.4 V, V_{REP}=0 V, cryo off.*

3.4.3 Scan in CFC Tile voltage (V_{CFC})

To conclude, the effect of the CFC tile polarization is discussed. The tile has to be polarized in order to collect all the secondary electrons emitted when it is hit by the beam. However, a non negligible effect of the tile biasing on the secondary plasma formed during the beamlets propagation is observed. While the polarization is practically irrelevant to the data collected by other diagnostics, its effect on the camera signals collected is important. In figure 3.25 the data gathered by the two cameras are reported. This data were collected with the V_{REP} fixed both at 0

and at 60 V. The first consequence on the CFC Tile polarization is the increase of the I_{CFC} measured, as it is shown in figure 3.24. In particular, the increasing
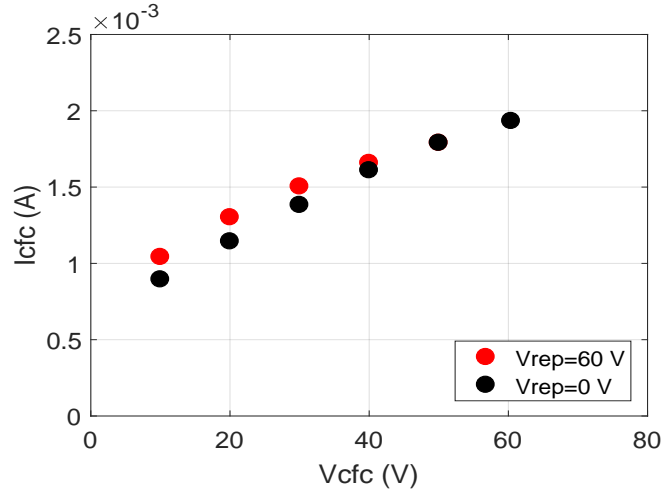
Figure 3.24: I_{CFC} as a function of V_{CFC}. The data refer to: 02/11/2017 V_{AGPS}=8 kV, V_{EGPS}=600 V, P=0.75 Pa, RF=1.1 kW, I_{PGF}=0 A, Bias PG=45 V, I_{BB}=0.1 A, V_{REP}=60.4 V, cryo off; 08/11/2017 V_{AGPS}=8 kV, V_{EGPS}=600 V, P=0.75 Pa, RF=1.1 kW, I_{PGF}=10 A, Bias PG=45 V, I_{BB}=0.1 A, V_{REP}=0 V, cryo off.

background is highlighted as a large Gaussian curve which increases as the V_{CFC} grows. The formation of this secondary plasma and its dependence on the CFC tile biasing will be analyzed in the following chapter by means of PIC simulation and compared with the data collected by the RFEA and Langmuir probes.
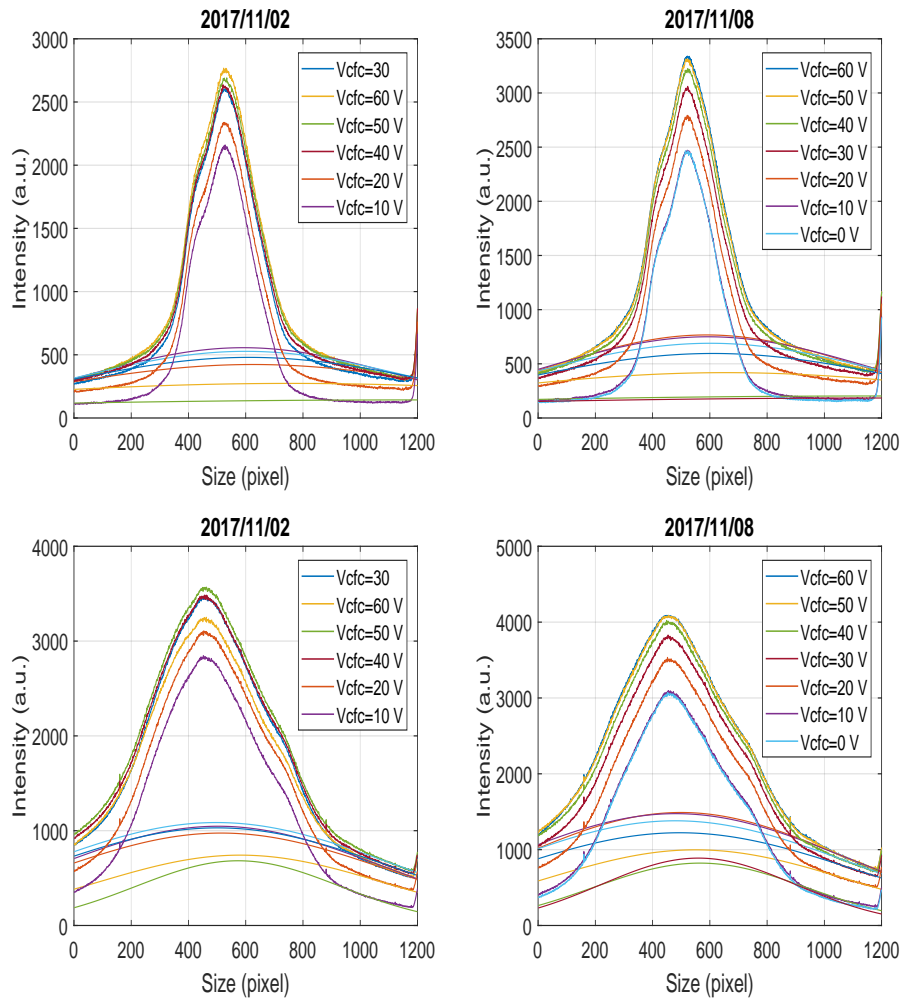
Figure 3.25: *Cameras data results as a function of V_{CFC}. The data refer to: 02/11/2017 V_{AGPS}=8 kV, V_{EGPS}=600 V, P=0.75 Pa, RF=1.1 kW, I_{PGF}=0 A, Bias PG=45 V, I_{BB}=0.1 A, V_{REP}=60.4 V, cryo off; 08/11/2017 V_{AGPS}=8 kV, V_{EGPS}=600 V, P=0.75 Pa, RF=1.1 kW, I_{PGF}=10 A, Bias PG=45 V, I_{BB}=0.1 A, V_{REP}=0 V, cryo off.*

Chapter 4

Reconstruction of experimental data by means of computer beam tomography tecniques

In this chapter the results already presented will be compared with the data obtained as a result of beam tomography reconstruction.

4.1 Camera calibration

On November 2017, a new two dimensional CMOS camera was installed on NIO1, to replace the lateral linear camera already present. It has the advantage of providing a two dimensional image of internal NIO1 vessel and the data collected can easily be compared with the data collected by the other two dimensional camera (the bottom one). Before proceeding to the installation, its performance has been tested and calibrated. To calibrate a camera its response upon varying gain and at the time exposure must be tested. For doing this test, a led is used as light source, and different acquisitions with different gain and exposure time have been carried out. In order to minimize the background, the camera was kept under a black towel.

In figure 4.1 the signal collected as a function of the exposure time is shown. The different gain values and led intensities used during data collection are indicated. As expected, the signal varies linearly with the exposure time variation. The gain dependence, instead, is not expected to be linear. To study this dependence, at first some measures in the absence of the led signal were taken. The data collected with and without the led signal are reported in figure 4.2.
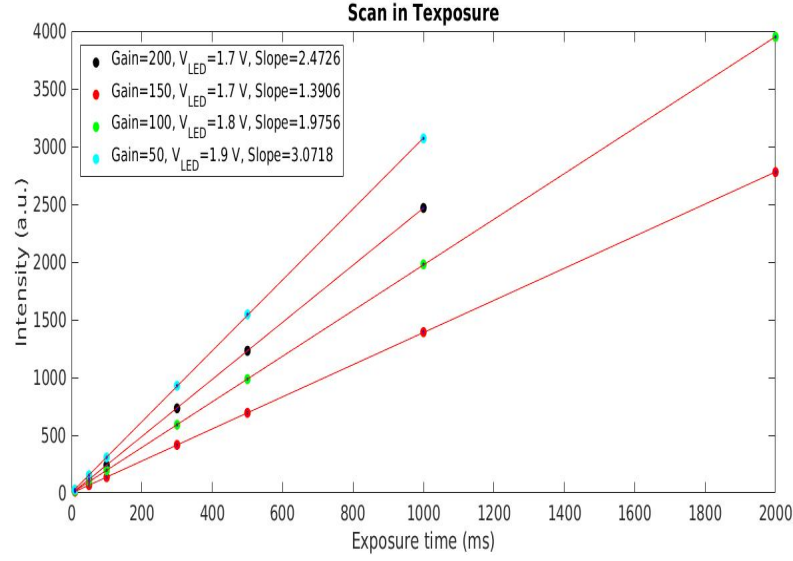
Figure 4.1: *Picture of NIO1 experiment.*
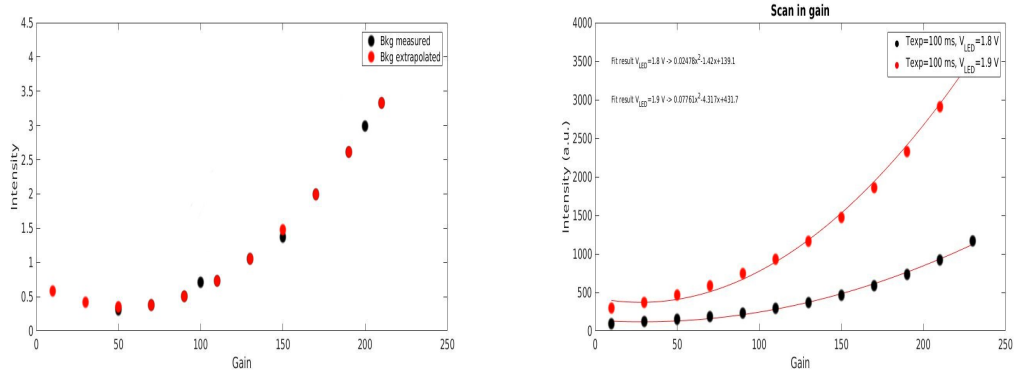
Figure 4.2: *Background data with varying gain (left side) and fit of the data as a function of the gain of the camera.*

The data are well fitted by a second order polynomial:

$$I = 0.02478x^2 - 1.42x + 139.1 \; for \; V_{LED} = 1.8 \; V$$
$$I = 0.07761x^2 - 4.317x + 431.7 \; for \; V_{LED} = 1.9 \; V$$

(4.1)

These results can be used during the experiment to correct the signal collected as a function of exposure time and gain.

Another important goal is the conversion from the camera pixels to millimeters. This study was made after the camera installation in NIO1, in order to determine the conversion pixel to millimeters for both the cameras. Using a chessboard
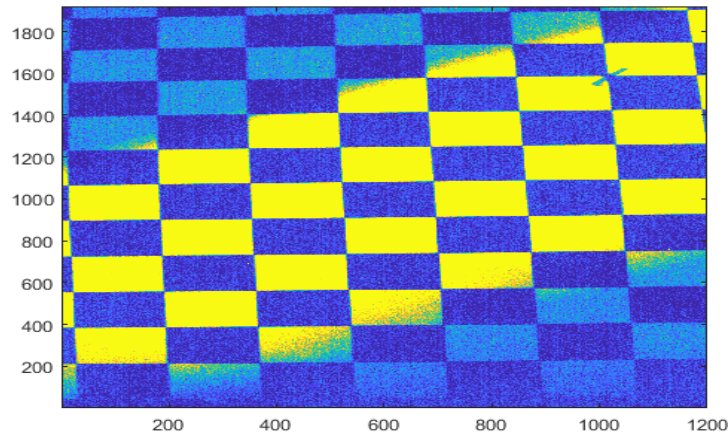
Figure 4.3: *Image collected by the lateral camera with the sheet positioned on the beam propagation plane (x and y in pixels).*

sheet as a reference, images at different distances corresponding to the beamlets propagation plane and to a closer and farther plane with respect to the camera have been taken. In addition to this, also the sheet inclination was varied to study the image deformation due to the camera inclination with respect to the beam propagation plane. The two cameras indeed are not orientated exactly in a perpendicular way with respect to the beam propagation plane. An example of the image acquisition is shown in figure 4.3.
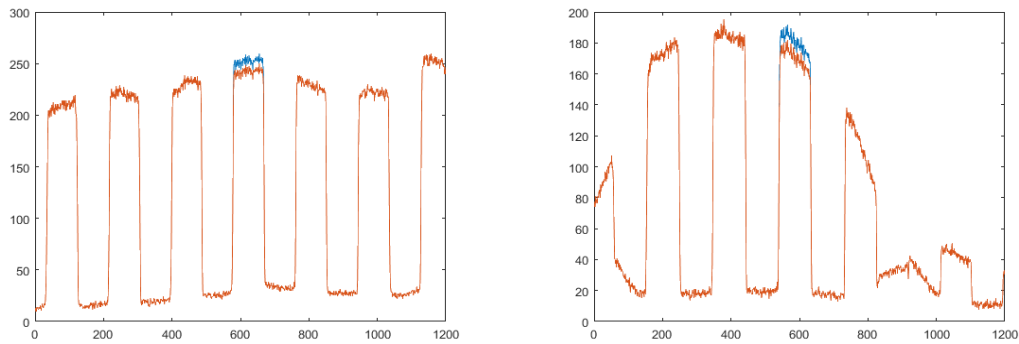
Figure 4.4: *Image sections taken by the inferior camera with the chessboard sheet positioned on the beamlets plane, with the sheet parallel to the beamlets plane (left case) and to the camera orientation (right case).*

In figure 4.4 a section of the image collected by the bottom camera is reported. The data were acquired with the chessboard sheet positioned close to the beam propagation plane, orientated in parallel either with respect to the beamlets propagation plane or with respect to the camera orientation. As a first approximation by measuring the width of the peaks one can prove that the image deformation due to the camera orientation is negligible.

Upon knowing the exact position of the cameras with respect the center of the vessel, assuming this corresponds to the plane of the beam propagation, a conversion from the camera pixel dimension to millimeters is possible. Since the measure of the chessboard sheet position with respect the bottom camera was more difficult to achieve, the conversion is made by using the data collected by the lateral camera. The vessel flange in which the lateral camera is sited has 300 mm radius. By considering the distance of the camera from the vessel approximately equal to 40 mm, a linear fit of the conversion from pixel to millimeters can be achieved. In figure 4.5 the result is reported.
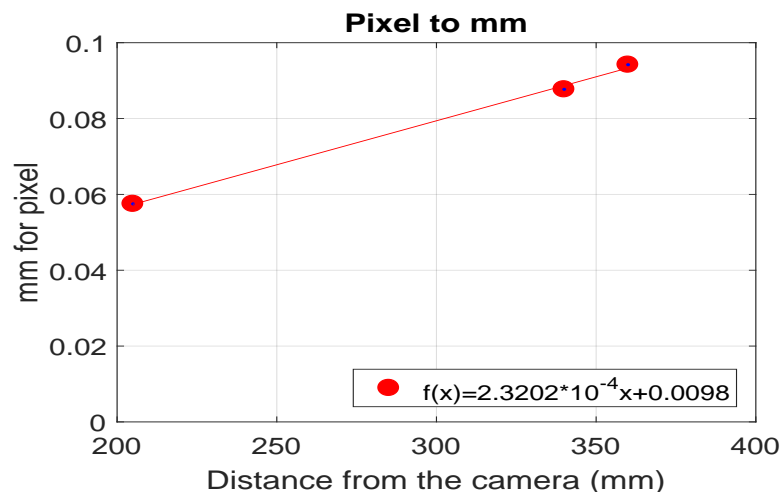
Figure 4.5: *Fit pixel to millimeters.*

From the fit of the data the conversion for images taken in the beamlet propagation plane results:

- *Lateral camera*: 1 *pixel* ~ 0.09 *mm*;

- *Bottom camera*: 1 *pixel* ~ 0.18 *mm*;

by considering the double magnification of optics of the lateral camera with respect to the bottom one. The result is affected by a relatively large experimental error due to the difficult measurement of the distance inside the vessel. Nevertheless

this result can be used as a reference to convert pixel to millimeters as a first approximation. To conclude, the response of the two cameras at the same light intensity has been tested. The results show a good agreement between the intensity collected by the two cameras.

4.2   Beam Tomography

The principal aim of beam tomography is the reconstruction of the beam emission profile by means of a large number of lines of sight (LoSs). The emission tomography measures the brightness f of an emissive source along a set of lines of sight l_j:

$$f_j = \int_{l_j} \epsilon(x, y) dx dy \tag{4.2}$$

where the integral is evaluated along each line of sight, which are considered as straight line. Using a large number of LoSs it is possible to obtain the function $\epsilon(x, y)$ from the brightness measurements. A neutral beam extracted and accelerated from a multi-beamlet negative ion source forms a pattern of small and well-separated beamlets whose identity can be recognized up to a distance of few meters. For this reason, a negative ion source can be simulated and inverted as a matrix of n Gaussians, where n indicates the number of beamlets. By definition, computed tomography makes use of computer-processed combinations of many measurements taken from different angles to produce cross-sectional (tomographic) images (virtual *slices*) of specific areas of a scanned object.

The number of projections and hence the sensors needed for a sufficiently good tomographic reconstruction of the emitting beam can be determined using the Fourier Slice Theorem [45]. It relates the measured projection data to the two dimensional Fourier transform of the projection along a set of LoSs. According to this theorem, this is equal to the two dimensional Fourier transform of the projection along a line perpendicular to the LoSs. The minimum number of ports needed depends in first approximation on the space resolution desired. The number of cameras needed to reconstruct the emitting region can be estimated through

$$N = \frac{\pi D}{\Delta s} \tag{4.3}$$

where Δs is the dimension of the minimum resolvable object and D is the dimension of the emitting plasma region. In NIO1, D is almost equal to 400 mm and if a $\Delta \sim 5$ mm is desired, the number of projection needed for a complete reconstruction without noise in ~ 34. In NIO1 just two point of view are presently available so a complete tomography reconstruction is not possible. However, through the data collected an idea of the evolution of the 9 beamlets can be obtained. In

the following, two different approaches will be described: an analytical and a computational one, the second mainly used to check the validity of the first method. Both approaches are based on the analysis of the integral of signals collected through a set of lines of sight. For this reason, a complete geometrical definition of the system is fundamental. As said before, the two CMOS camera in NIO1 are positioned at 90 degrees with respect to each other. The beam propagation plane is indicatively 340 mm distant from both cameras. As demonstrated with the calibration, the camera angles with respect this plane can be neglected. Hence the two cameras provide two perpendicular images of the beamlet array at a distance of about 30 cm from the PA. The light collected is produced by fast particles of the beam via charge exchange with the background gas, on a plane perpendicular to the beam. Each camera array collects the LoS-integrated optical signals of a set of LoSs. By assuming that the density of the background gas is uniform across the observed plane, tomographic reconstruction allows to estimate the two dimensional beam emission function which is proportional to the beam density. As a first approximation, the LoSs can be considered as simple lines collecting the signal from the beamlets plane to the cameras. Considering one LoS per pixel, both cameras have 1200 LoS for collecting the light. This set of LoSs departing from the cameras forms a fan collecting the light. Inside each fan, each line of sight has an angular aperture depending on the distance of the camera from the beam plane. Since the NIO1 dimension are relatively not very large, with respect to SPIDER dimension for example, they can be well approximated as unidimensional lines. Furthermore, NIO1 optics is optimize to constitute thin lines of sight.

4.2.1 Analytic approach

This method is based on the inversion algorithm: starting from a *phantom*, one tries to reconstruct the signal by means of line integrals through the LoSs. The phantom is the two dimensional emissivity profile of neutral beam which has to be reconstructed. To this purpose, the emission profile of every single beamlet is represented as a 2-dimensional Gaussian surface (see figure 4.6):

$$G_g(x,y) = A_g e^{-\frac{(x-x_0)^2}{2\sigma_{x0g}^2} - \frac{(y-y_0)^2}{2\sigma_{yg}^2}}, \qquad (4.4)$$

where the subscript g indicates one of the 9 beamlets and

$$x_0 = x_{0gg}, \; y_0 = y_{0gg} + \delta_y \qquad (4.5)$$

where x_{0gg} and y_{0gg} are the x and y coordinates of the Plasma Grid (the grounded grid) holes through which the beam is extracted and δ_y the vertical deflection due
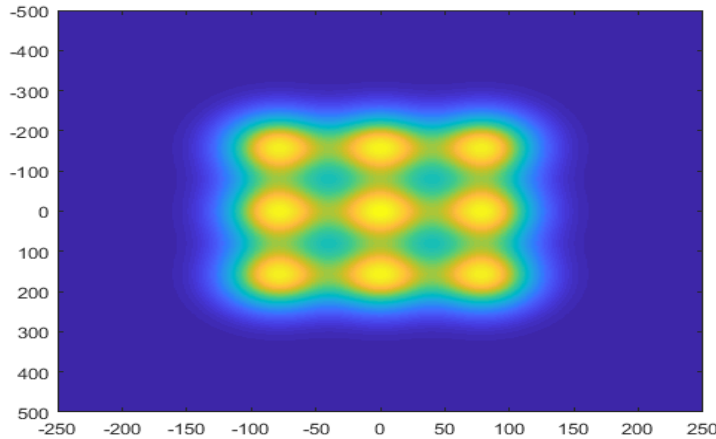
Figure 4.6: *NIO1 9 beamlets representation as 9 bi-dimensional Gaussians.*

to magnetic field configuration. As a first approximation it will be considered $\sigma_x = \sigma_y = \sigma$.

Every beamlets has four free parameters that can be varied for generating different phantoms: the amplitude A, the position along x and y and the width σ. The PA holes are 14 mm away along x and y direction and the deflection can be estimated, according to *paraxial approximation* formula as [48].

$$\delta_y = \frac{v_y, exit}{vz, exit} = \frac{q \int_{z_0}^{z_{exit}} B_x dz}{m v_{z,exit}} = \sqrt{\frac{q}{m}} \frac{\int_{z_0}^{z_{exit}} B_x dz}{\sqrt{2U_{extr}}} \tag{4.6}$$

where q and m are the ion charge and mass, U_{extr} the acceleration potential and z_0, z_{exit} are the initial and final axial coordinates of the ion trajectories.

4.2.2   Line Integral Evaluation

Once the phantom is generated, the line integrated signal of the emissivity along the i-th LoS is calculated (I_i). The line integrated signal is calculated by integrating the emissivity of all Gaussian beamlets along the straight line that define a LoS:

$$y = a_i + b_i x. \tag{4.7}$$

The emissivity of a Gaussian surface is defined as

$$\epsilon(x, y) = A exp\left\{\left(-\frac{x - x_0}{\sigma}\right)^2 - \left(\frac{y - y_0}{\sigma}\right)^2\right\} \equiv A exp\left(-\frac{C}{\sigma^2}\right). \tag{4.8}$$

When it is evaluating along the i-th line of sight $y = a_i x + b_i$ it yields

$$
\begin{aligned}
C &= (x - x_0)^2 + (y - y_0)^2 = (x - x_0)^2 + (a_i x + b_i - y_0)^2 = \\
&= (x - x_0)^2 + ((b_i - y_0) + a_i x)^2 = \\
&= (b - y_0)^2 + a_i^2 x^2 + 2(b_i - y_0)(a_i x) + x^2 + x_0^2 - 2xx_0 = \\
&= x^2(a_i^2 + 1) + 2x((b_i - y_0)a_i - x_0) + ((b_i - y_0)^2 + x_0^2).
\end{aligned}
\tag{4.9}
$$

This can be written as

$$
(\alpha_i^2 x^2 + 2\alpha_i \beta_i x + \beta_i^2) + (\gamma_i - \beta_i^2) = (\alpha_i x + \beta_i)^2 + (\gamma_i - \beta_i^2)
\tag{4.10}
$$

with

$$
\begin{aligned}
\alpha_i &= \sqrt{a_i^2 + 1} \\
\beta_i &= ((b_i - y_0)a_i - x_0)\alpha_i^{-1} \\
\gamma_i &= ((b_i - y_0)^2 + x_0^2)
\end{aligned}
\tag{4.11}
$$

from which the emissivity calculated along a LoS becomes

$$
\epsilon(x, y)_i = A exp\left\{ -\frac{(\alpha_i x + \beta_i)^2 + (\gamma_i - \beta_i^2)}{\sigma^2} \right\}.
\tag{4.12}
$$

Now integrating through the line of sight yields

$$
I_{gi} = \int_{LoS_i} \epsilon(x, y)dl = A exp\left\{-\frac{(\gamma_i - \beta_i^2)}{\sigma^2}\right\} \int_{-\infty}^{+\infty} e^{-\frac{(\alpha_i x + \beta_i)^2}{\sigma^2}} dx
\tag{4.13}
$$

Defining $z = \alpha_i dx \longrightarrow dx = \frac{dz}{\alpha_i}$ the integral becomes

$$
\frac{A}{\alpha_i} exp\left\{-\frac{(\gamma_i - \beta_i^2)}{\sigma^2}\right\} \int_{-\infty}^{+\infty} e^{-z^2} dz = \frac{\sqrt{\pi}A\sigma}{\alpha_i} e^{-\frac{(\gamma_i - \beta_i^2)}{\sigma^2}}
\tag{4.14}
$$

The result obtained must be evaluated for all the 9 beamlets. The integrated line signal collected by a single LoS hence is

$$
\sum_{g=1}^{9} I_{gi}
\tag{4.15}
$$

where the sum is extended to all the 9 Gaussian surfaces representing NIO1 beamlets. Once the phantom has been designed, using equation 4.14 it is possible to evaluate all the line integrated signals representing the experimental signals collected by the camera. Using these results as input for the tomographic inversion it is possible to reconstruct the image seen by the camera and to compare it with the experimental data.

A MATLAB software has been developed in order to achieve the reconstruction just described.

4.2.3 Code Description

The experimental set-up is shown in figure 4.7.
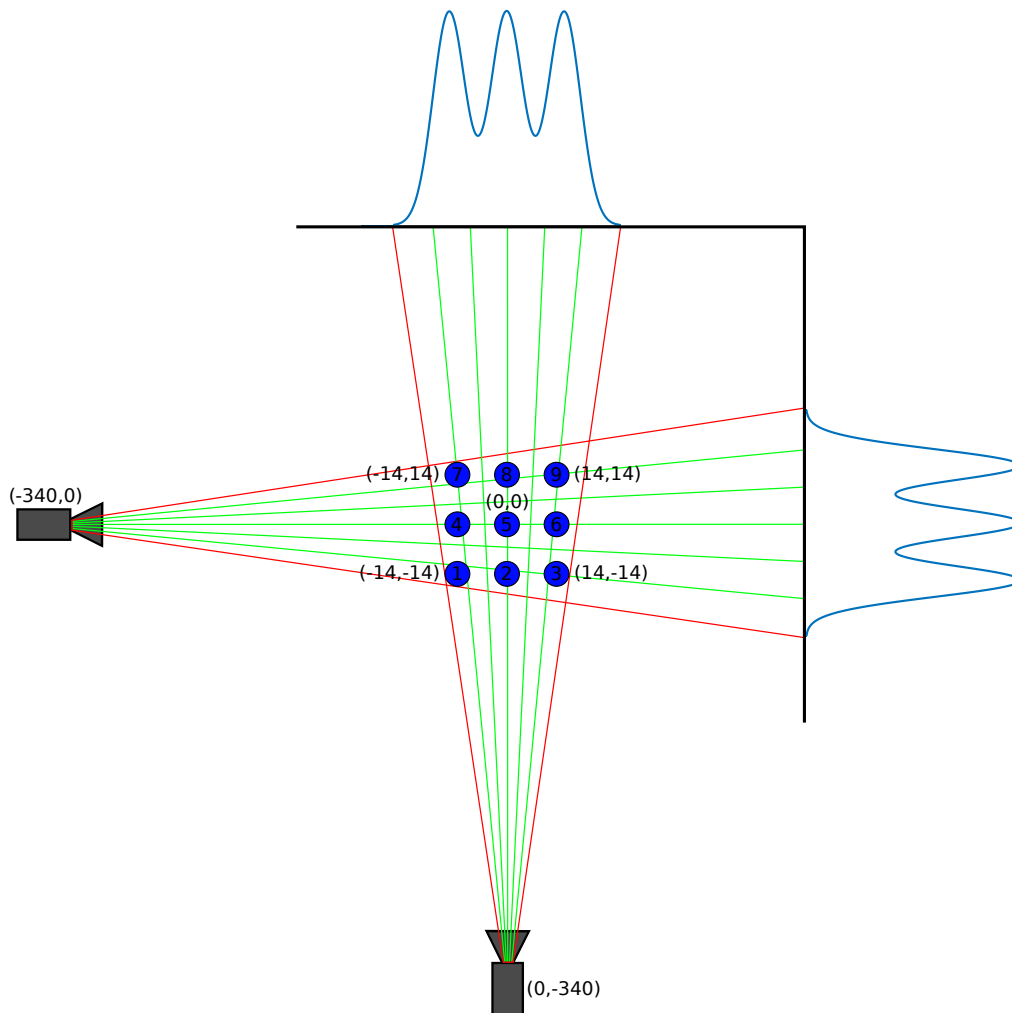
Figure 4.7: *Experimental set-up representation. All the distances are in millimeters.*

In the code all the distances are used in unity of pixel. Since the lateral camera has a magnification double with respect to the bottom one, a double number of pixel has been used to compare the lateral profile with the bottom one. After subtracting the background from the experimental data, the difference between the results of the line integral and the data collected is minimized until a minimum is reached. Hence, the results obtained from the minimization are used to construct a matrix composed by nine Gaussians representing the nine beamlets. The matrix

thus obtained can be used to test the goodness of fit. Using a bi-dimensional interpolation it is possible to integrate along the lines of sight the matrix just built and to check the validity of the results. As an example, the description of the image reconstruction from the data collected during the scan in pressure described in the chapter 3 follows. The data refers to 0.7 Pa as source pressure, V_{AGPS}=2.5 kV, EGPS=350 V, RF power=1.2 kW, I_{PGF}=10 A, I_{BB}=0.2 A and the cryo off. In figure 4.8 the data collected by the cameras are shown.
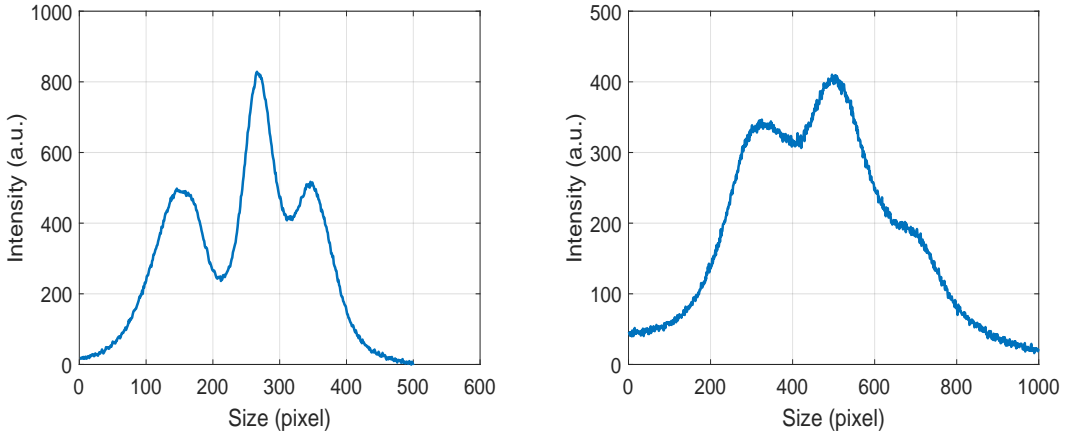
Figure 4.8: *Experimental data collected by the inferior camera (left side) and by the lateral one (right side).*

The two images are normalized with respect to the signal integral collected and merged in a single vector. This normalization is necessary because the absolute calibration of the two systems (optic plus camera) is missing. The free parameters of the fit are 36: 9 x_0 and 9 y_0 of the beamlet positions, 9 amplitudes and 9 sigmas. By selecting the initial values of the minimization in order to be as close as possible to the experimental data, the minimization converges in an easier way. The result of the minimization is shown in figure 4.9.

The results of the fit converted in millimeters are reported in table 4.1 in the frame of reference used in figure 4.7.
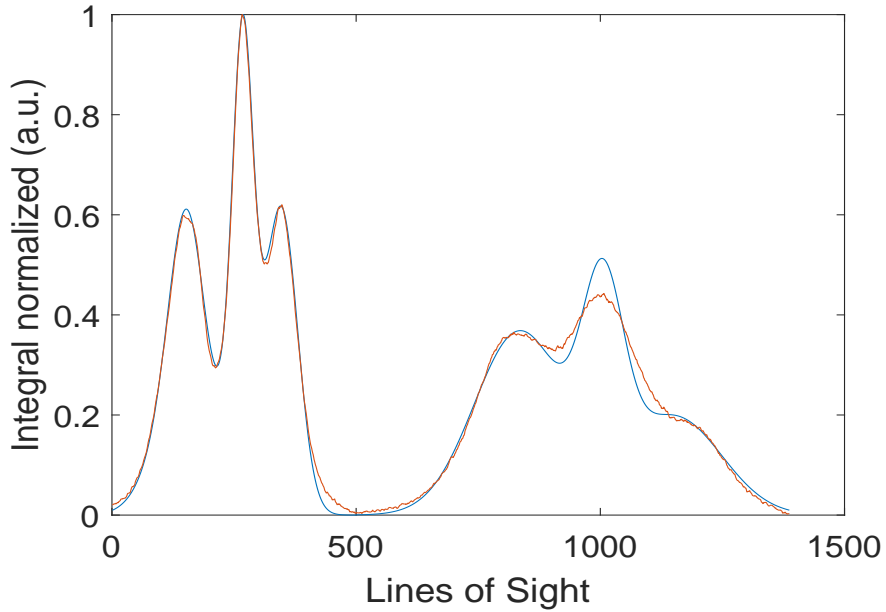
Figure 4.9: *Experimental data (red line) and fit reconstruction (blue line).*

	x_0 (mm)	y_0 (mm)	σ (mm)	A
Beamlet 1.	-19	17	6	13
Beamlet 2.	2	14	12	10
Beamlet 3.	15	17	4	13
Beamlet 4.	-18	0.2	9	15
Beamlet 5.	3	0.5	5	35
Beamlet 6.	17	0.5	6	14
Beamlet 7.	-21	-17	9	14
Beamlet 8.	-2	-13	10	11
Beamlet 9.	13	-17	15	13

Table 4.1: *Example of fit results.*

With these parameters it is now possible to reconstruct a matrix representing the 9 beamlets as 2D Gaussian surfaces. By 2D interpolation, the integral along the lines of sight can be evaluated on the matrix to check the consistence between the data resulting from the minimization fit. All these results are shown in figure 4.10.

The fit in figure 4.9 however does not match perfectly the experimental data, so different approaches have been made. By fixing some free parameters of the fit,
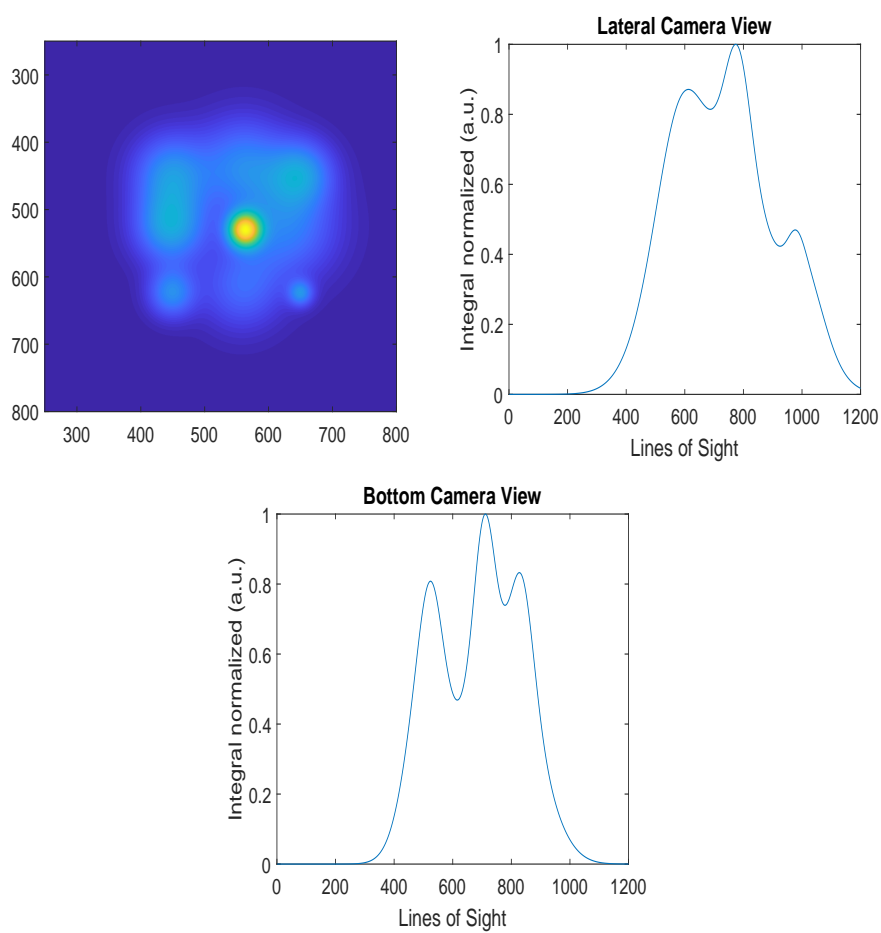
Figure 4.10: *Beamlet representation and interpolations along the camera lines of sight.*

it is possible to improve the fit result. In figure 4.11 the same reconstruction is shown with the sigmas of all the beamlets fixed at the same value.
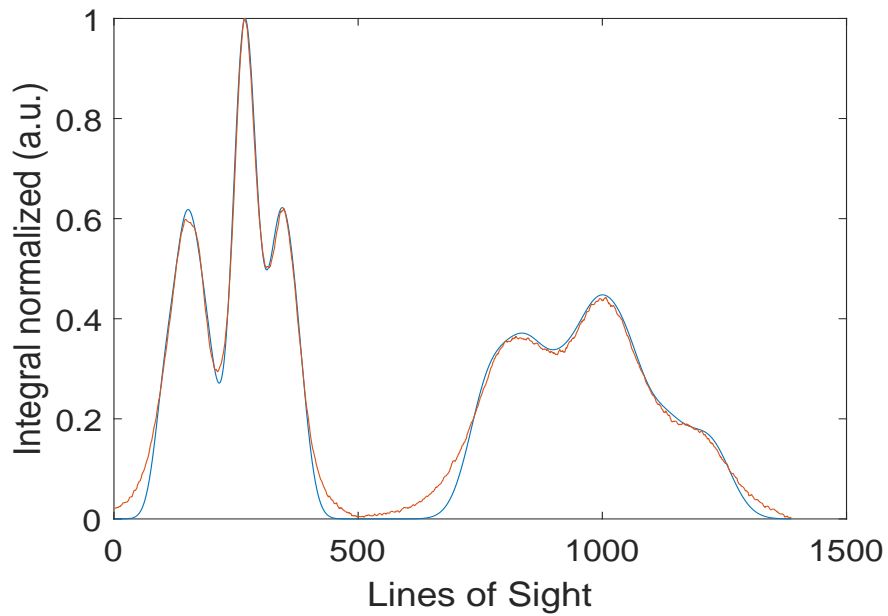
Figure 4.11: *Experimental data (red line) and fit reconstruction (blue line).*

The results of the fit converted in millimeters are reported in table 4.2.

	x_0 (mm)	y_0 (mm)	σ (mm)	A
Beamlet 1.	-11	25	7	5
Beamlet 2.	6	23	7	2
Beamlet 3.	19	20	7	3
Beamlet 4.	-24	9	7	5
Beamlet 5.	1	0.5	7	10
Beamlet 6.	16	1	7	7
Beamlet 7.	-22	-12	7	8
Beamlet 8.	-7	-21	7	7
Beamlet 9.	11	-14	7	3

Table 4.2: *Example of fit results.*
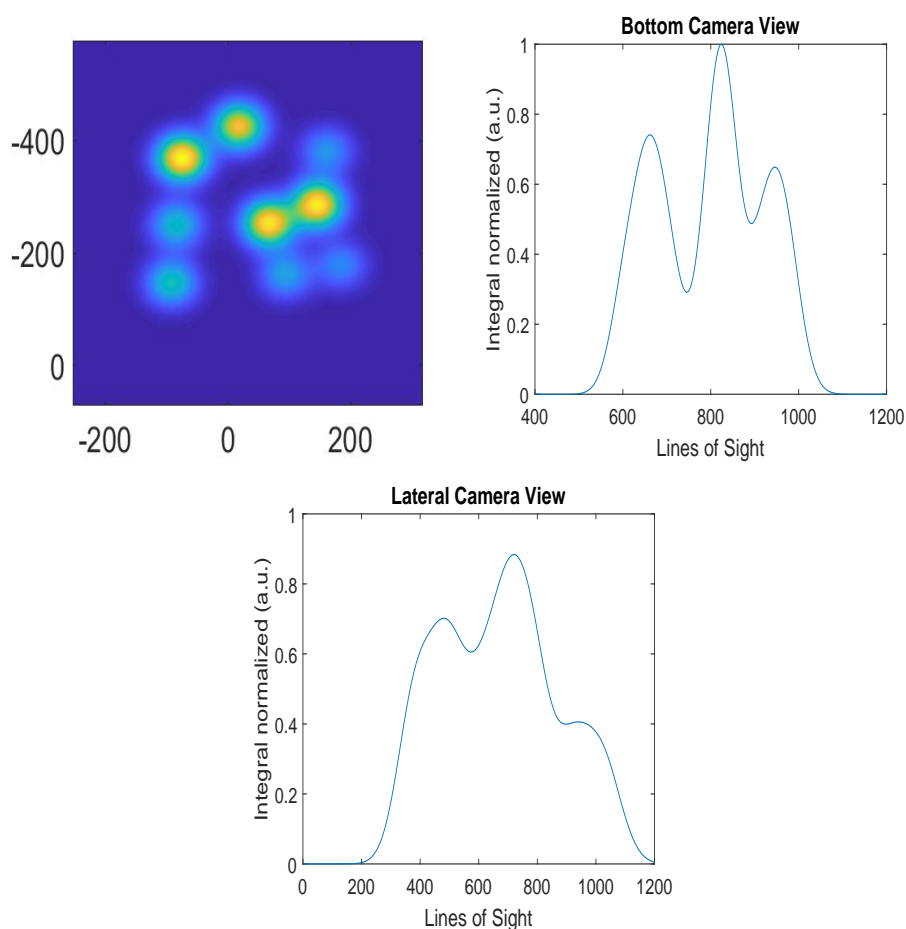
Figure 4.12: *Beamlet representation and interpolations along the camera lines of sight.*

The results of the two fits are quite different, as it can be seen in the reconstruction in figure 4.12.

By fixing the sigmas to a single value, the symmetry of the 3x3 matrix of beamlets exiting from the PA is lost. Indeed, a spread of the rows is visible and the fit of the experimental data has been improved. Unfortunately, it is hard to decide how of these two results well represent the reality, due to the leakage of further point of view inside the NIO1 vessel. As said before, this beam tomography is just an approximation since there are only two points of beam observation. Since there are a large number of free parameters, the fit is not robust. Indeed many beamlets are not directly visible by the two cameras so their amplitude and sigma can easily be misidentified. A more complete reconstruction can be achieved with the addition of extra cameras on NIO1 [46]. However in the following, a first comparison between the experimental data and the fit reconstruction is reported. The results of both fits will be shown and compared.

4.3 Experimental data comparison

Using the method just described, it is possible to study the development of the beamlet configuration in the sets of experimental data acquired. Beam evolution close to the optimal condition described in chapter 3 have been analyzed. At first, consider the scan in V_{AGPS} at 300 V of extraction voltage collected on 08/11/2017. In figure 4.13 the development of the beamlets reconstruction, with all the 36 parameters free, when V_{AGPS} is varying is shown.
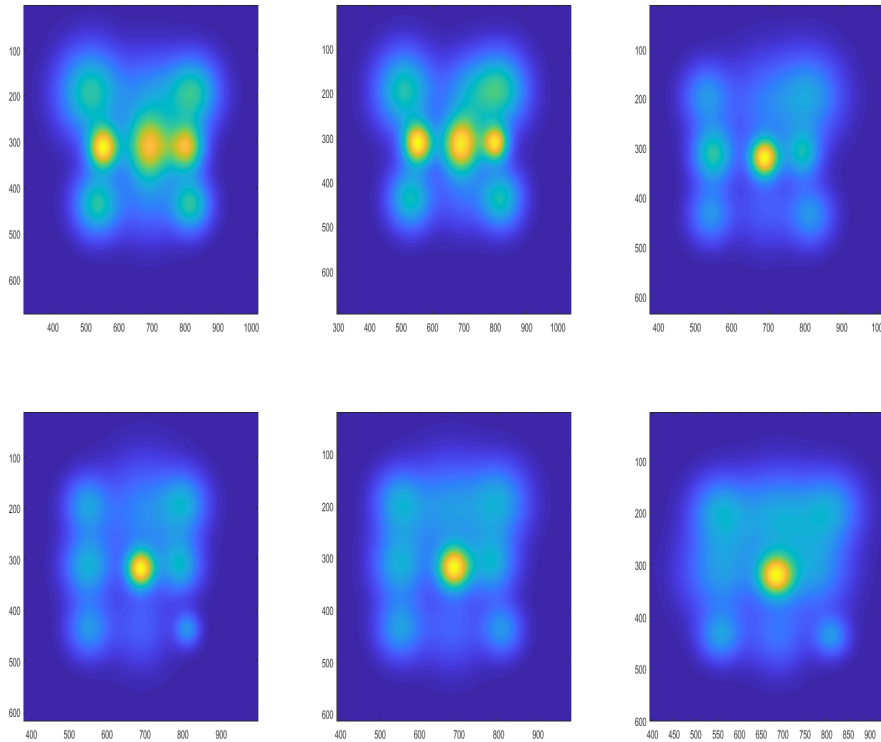
Figure 4.13: *Beamlets development with V_{AGPS} increasing. In the order the images refer to V_{AGPS}=1500,1750,2000,2500,2750,3000 V while EGPS has been kept fixed to 300 V. All the fit parameters are free.*

The best optics configuration is the central one in the lower set where almost all 9 beamlets are distinguishable. It corresponds to V_{AGPS}=2750 V and it confirms the results obtained from the other diagnostics. From this reconstruction, it is possible to analyze the evolution of the x and y beamlet coordinates. These results are shown in figure 4.14 with respect to the beamlet coordinates of the PA (the grounded grid).

When V_{AGPS} approaches to the optimal optics value the x0 peak positions
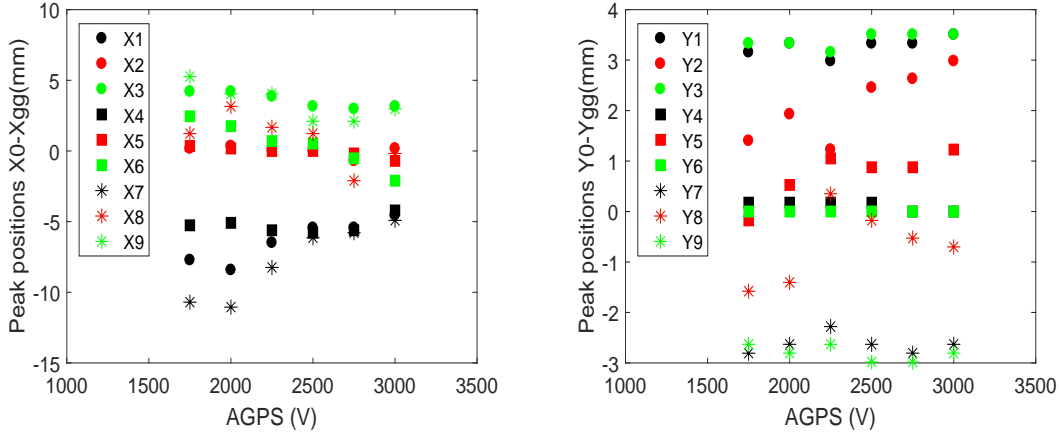
Figure 4.14: $X - x_{GG}$ and $y - y_{GG}$ beamlet coordinates as a function of V_{AGPS}. All the parameters of the fit are free.

are close to the PA coordinates, before getting worse again. It is shown also in figure 4.13 where for V_{AGPS}=2750 V the 9 beamlets are well aligned in an almost symmetric pattern in both directions. The y positions instead appear less dependent by changing in V_{AGPS}. Another useful parameter that can be controlled to study the beamlet evolution is the distance between the central row of beamlet and the two lateral rows. These are shown in figure 4.15. As V_{AGPS} increases, the distances between the rows in the x direction become lower, even if a little displacement remains. Concerning the y differences instead, figure 4.15 confirms the almost invariance of y position as it was seen in the previous images.
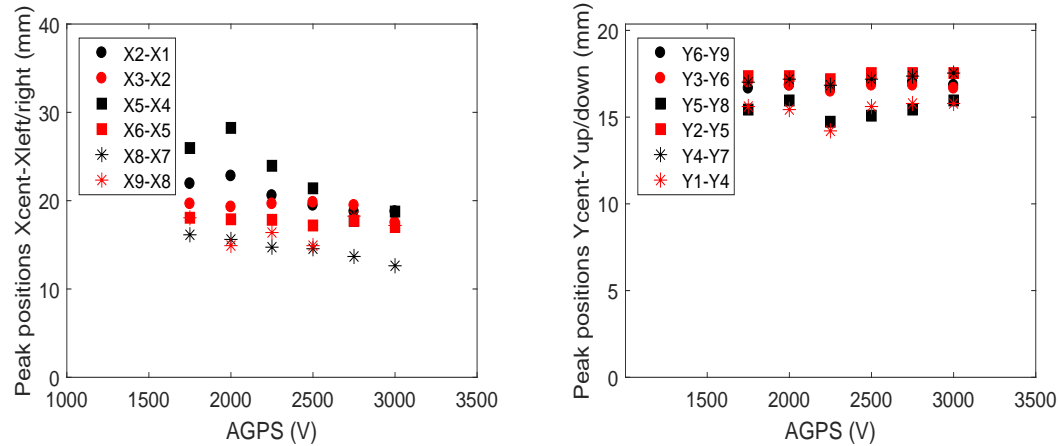
Figure 4.15: Delta beamlets as a function of V_{AGPS}. All the fit parameters are free.

The evolution of the width (sigma) of the nine beamlets as V_{AGPS} increases is shown in figure 4.16. Even if a single trend cannot be identified, all the sigmas appear more symmetric close to the optimum optics value (V_{AGPS}=2.5 kV).
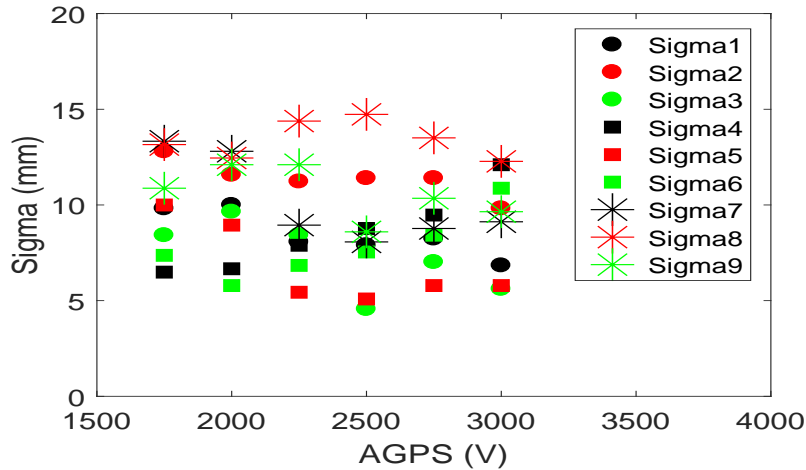
Figure 4.16: *Sigma of the beamlets as a function of V_{AGPS}.*

These reconstruction can be compared with the fit made with the sigmas fixed to a single value. In these fits furthermore, the limits on the range in which the x coordinates can move is limited strictly with respect to the previous case. In figure 4.17 the development of the beamlets reconstruction with one single sigma fixed for all the beamlets is shown.

These images are quite different from the ones shown previously. While the symmetry of the pattern is worst, the 9 beamlets are more distinguishable. Unlike the previous fit, the amplitudes of the 9 Gaussians are better subdivided, even if the amplitude of some of them is considerably reduced as the optics becomes worst.

Due to the strictly boundaries imposed, the information which can be achieved from this reconstruction is less with respect to the first approach. In figure 4.18 the coordinates of the beamlet with respect to the GG are shown. While the y coordinates are almost unchanged with respect to the previous fit, the information on the x coordinate is lost due to the boundary imposed.

Concerning the distances between the beamlets, the results of this fit are shown in figure 4.19. The main difference is visible in the distance between the beamlets in each row: the separation indeed is more evident and asymmetric. As V_{AGPS} increases, the distance between the higher and lower row with respect to the central one is expected to decrease. This is confirmed in figure 4.20, where this decrease is present in both the fits.
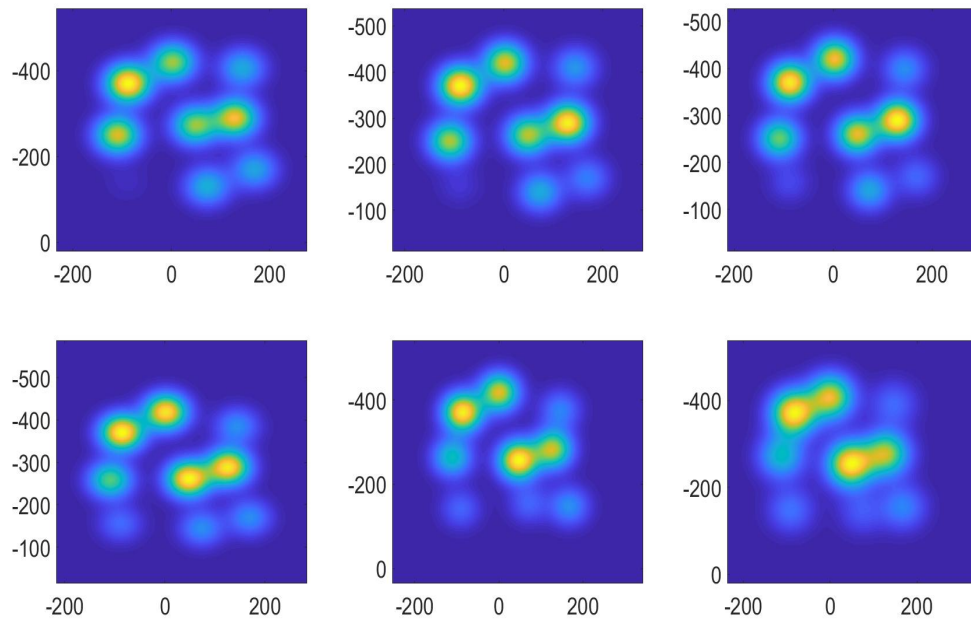
Figure 4.17: *Beamlets development with V_{AGPS} increasing. In the order the images refer to V_{AGPS}=1750,2000,2250, 2500,2750,3000 V while EGPS has been kept fixed to 300 V. All the sigmas are fixed at one single value.*
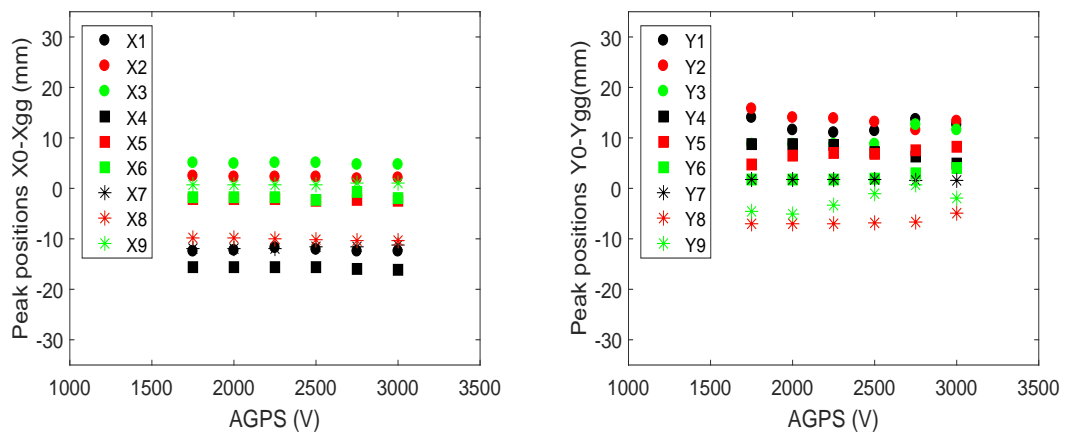
Figure 4.18: *$X - x_{GG}$ and $y - y_{GG}$ beamlet coordinates as a function of V_{AGPS}. The sigmas are fixed at one single value.*
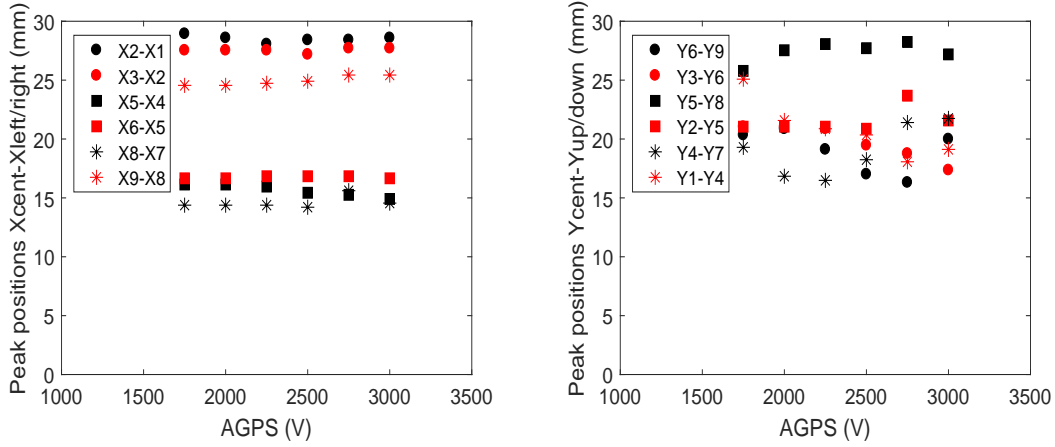
Figure 4.19: *Delta beamlets as a function of V_{AGPS}. The sigmas are fixed at one single value.*
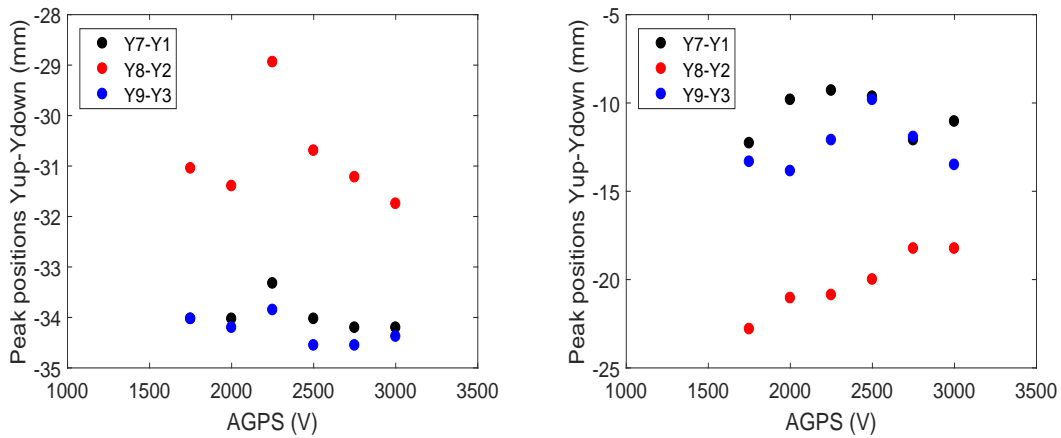
Figure 4.20: *Delta beamlets as a function of V_{AGPS}. All the parameters are free in the left-hand plot while the sigmas are fixed in the right-hand plot.*

The deflection along the y direction is more distinguishable when V_{EGPS} is varying due to its dependence according to the equation 4.6. For this purpose the set of data acquired when varying V_{EGPS} described in chapter 3 has been reconstructed.
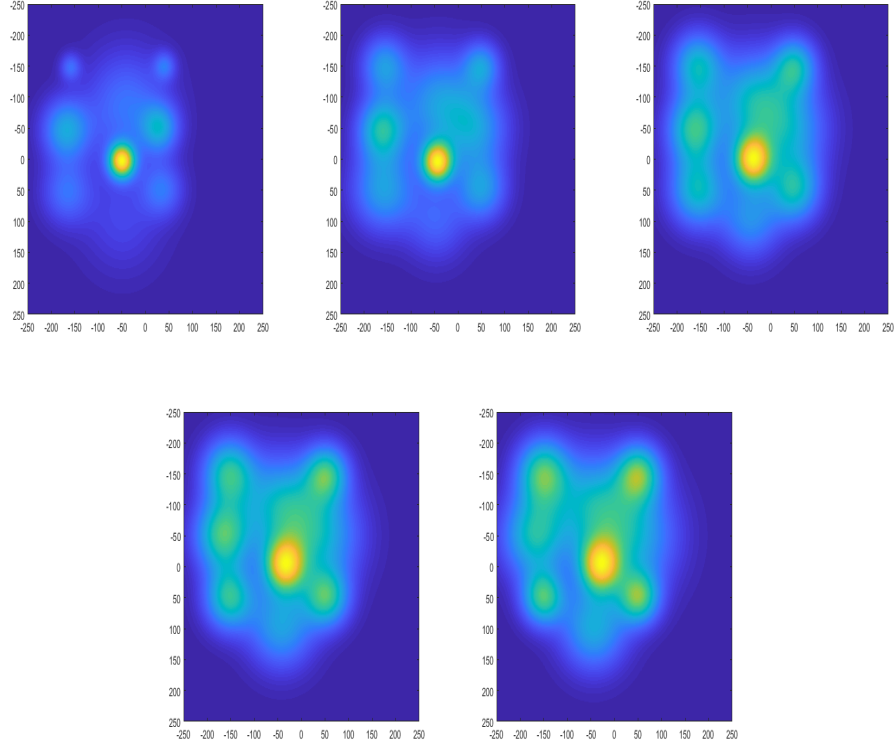
Figure 4.21: *Beamlets development at V_{EGPS} increasing. In the order V_{EGPS} is equal to 250, 350, 400, 450, 500 while AGPS has kept fixed to 2 kV. All the parameters are free.*

In figure 4.21 the evolution of the 9 beamlets with increasing V_{EGPS} is shown. As expected, the beamlets became more energetic since the quantity of particles extracted increases with increasing V_{EGPS}. Also the beamlet deflection along y direction becomes more evident as it is shown in figure 4.22, where the x and y positions of the nine beamlets are plotted.
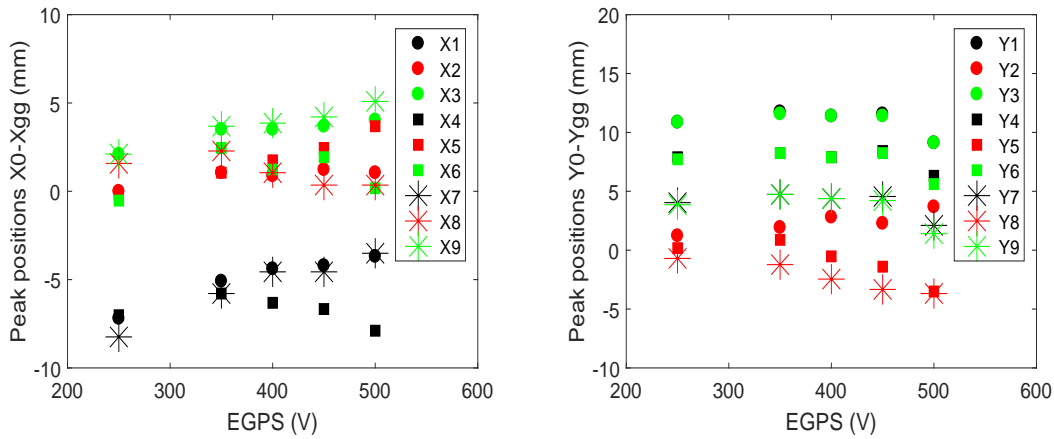
Figure 4.22: $X - x_{GG}$ and $Y - y_{GG}$ beamlet coordinates as a function of V_{EGPS}. All the fit parameters are free.

In both the coordinates, as V_{EGPS} exceeds the optimal value of 350 V, the beamlets are no more aligned. In particular, for the optimal V_{EGPS} value, in the y direction it is evident how the central column has no displacement with respect the Grounded Grid while the lateral ones are at higher y values. This is probably due to the vertical deflection due to the magnetic field configuration. As V_{EGPS} increases, the displacement becomes less evident since all the beamlets appear to lower along y direction except the central beamlet. Concerning the x direction, the different distances between the rows are shown. As it was highlighted in chapter 3, when the beamlets are distinguishable the 3 rows of beamlets are usually not equidistant. The evolution of the sigma of the beamlets as a function of V_{EGPS} is shown in figure 4.23
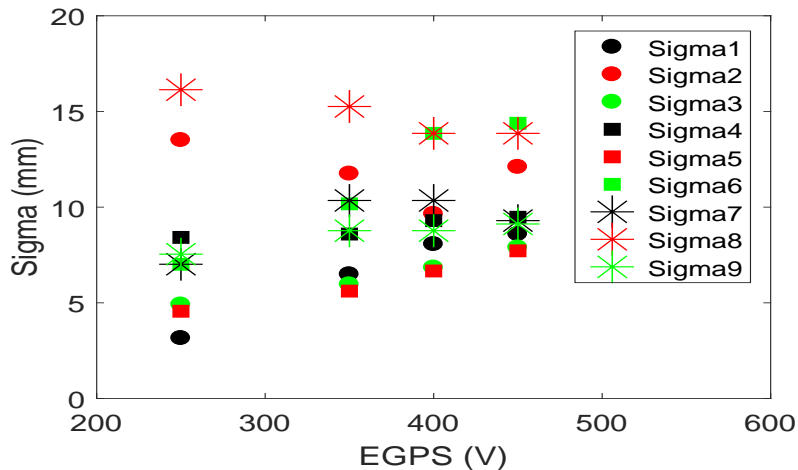
Figure 4.23: Sigma of the beamlets as a function of V_{EGPS}.

With the increasing of V_{EGPS}, the widths appear more similar. Concerning the second approach, the beamlets are clearly distinguishable when V_{EGPS}=350 V while, as the voltage increases, the pattern become less symmetric. The beamlets evolution is shown in figure 4.24.
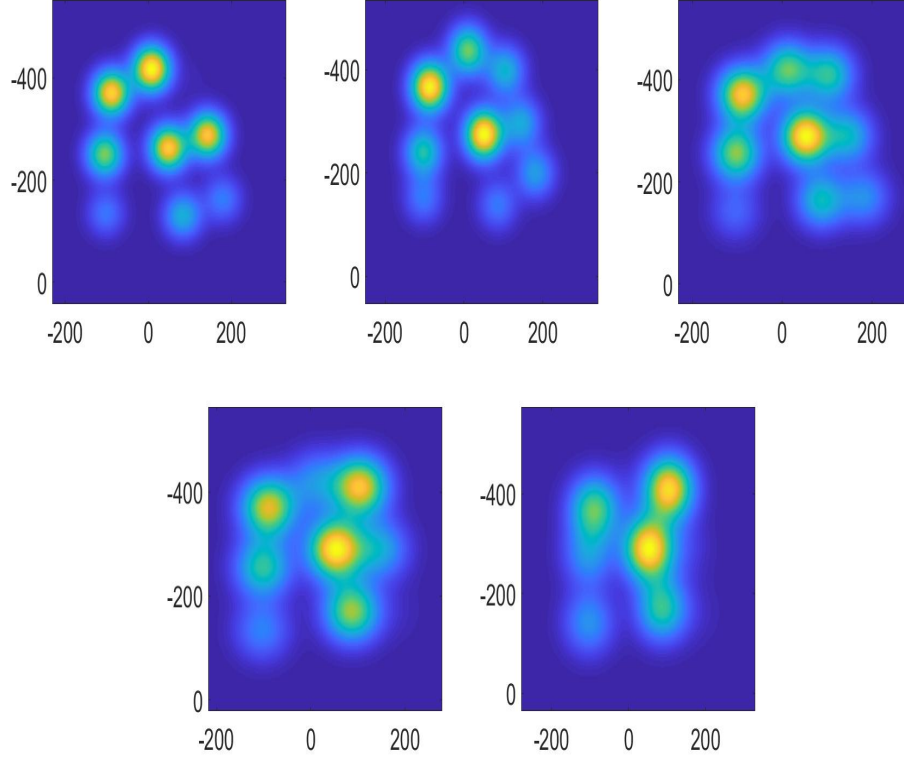
Figure 4.24: *Beamlets development at V_{EGPS} increasing. In the order V_{EGPS} is equal to 250, 350, 400, 450, 500 while AGPS has kept fixed to 2 kV. The sigmas are fixed at one single value.*

Due to the narrower constraints, the information on the x coordinate is partially lost. In figure 4.25 it is shown how, with the increasing of V_{EG}, the distance between the left column from the central one increases, the opposite for the right one. Concerning the y coordinate, the deflection is less distinguishable. For the best optics value however it can be seen how the central column is shifted downward and the opposite for the lateral two.

By summarizing, two different approaches have been compared: the first one leaves all the parameters free while the second one imposes some limitations. The results show how the minimization, when is not subjected to constraints, reconstructs one central Gaussian with the highest amplitude with respect to the others. By imposing limitations on the fit parameters, the pattern reconstructed is more
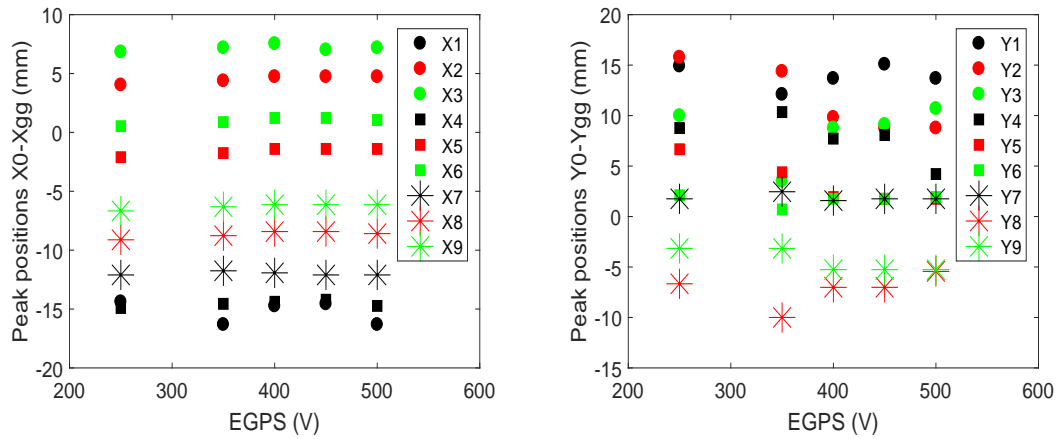
Figure 4.25: $X - x_{GG}$ and $Y - y_{GG}$ beamlet coordinates as a function of V_{EGPS}. The sigmas are fixed at one single value.

asymmetric but the Gaussians are more similar. This lost of symmetry however has been already observed in numerical simulation of multi-beamlet negative ions[44].

Chapter 5

Experimental and numerical investigation of the beam plasma

In this chapter, after a brief introduction of the concept of the beam plasma, its characterization will be obtained through the comparison between experimental data and the numerical simulations. Finally, the results of the simulation will be used to investigate plasma properties which cannot be directly seen by the experimental device.

5.1 Beam plasma formation and space charge compensation

When an intense ion beam propagates, spreading of the beam particle trajectories occurs due to the mutual repulsion of the beam ions. Efficient transportation of a high-current ion beam requires that the space charge of the beam ions is compensated for by electric charges of opposite sign, unless external electric or magnetic field are applied. The space charge effect in a negative ion beam source depends on various parameters. In the first place, it depends on the applied voltage and electrode design, on the uniformity of the ion current density j_{H^-} and on the ratio R_{ij} between the emitted electron current density j_{e^-} and j_{H^-}. When the beam propagates through a neutral gas, the beam ions neutralize the background gas, producing also charges of the opposite sign; in the case of a negative ion beam, the compensating species are the slow positive ions, in the case of a positive ion beam, electrons are the compensating species. In the initial stage of this process, the *anti-compensating* particles are expelled from the ionization region by the radial electric field, while the compensating species are confined in the potential well of the ion beam. Steady-state is reached when the flow of particles of both charges leaving the beam region equals the number of particles generated per unit

time. These can counterbalance on the average the generation of plasma particles, namely electrons and ions, in the axial region of the beam. The space charge distribution that is established in the beam channel depends on the generation rate of plasma particle and their confinement time, and it determines the radial potential drop $\Delta\phi$ from the beam axis to the edge, and within the beam itself.

The specific features of positive and negative ion beam transport are related to the large difference in the masses of the electrons and ions produced by ionization of the residual gas by fast heavy particle impact. The resulting system is essentially a specific *ion-beam* plasma. The space charge compensation process is essentially different for positive and negative ion beams, mainly due to the large mass of compensating particles (positive ions). In the case of a negative ion beam, when heavy positive ions act as neutralizing charge particles, two regimes of radial charged-particle fluxes can be established. These are defined by the compensation parameter $\Delta\phi$. The beam is *under-compensated* when the compensation parameter is negative and *over-compensated* the opposite. The pressure at which the compensation parameter is null is called *critical pressure*. The beam in under-compensated whene the pressure is less than the critical pressure P_{CR}; it is greater than P_{CR} when it is over-compensated. In the former case, the residual radial electric field leads to the expansion of the propagating beam, while in the latter case, it results in beam focusing. Decompensation can be due to different effects. At low gas pressure, it can be caused by ion oscillations in the plasma. In the case of negative ions, when the produced electrons are expelled from the beam by the beam electric field, the electron density becomes much lower than the density of the positive ions. In this case, the system may became unstable against the fundamental mode of ion oscillations with the half-wavelength on the order of beam diameter, preventing the beam channel from being filled by positive ions. Another decompensation factor is beam-current oscillations caused by plasma instabilities in the ion source itself.

At pressure higher than the critical pressure, the electron density is considerably higher and the influence of electron and ion oscillations on the formation of the space charge distribution is insignificant; in fact, even if electron oscillations are dominant in this regime, their effectiveness in terms of decompensating effect is poor. Due to intense generation of positive ions, their quasi-steady distribution corresponds to a positive beam potential $\Delta\phi > 0$. This means that the beam space charge is over-compensated and the radial flux of the positive ions is mainly caused by the electric field. In the following, an estimation of the compensation parameter will be given from the results obtained by the PIC simulation.

The critical density corresponding to the critical pressure at which $\Delta\phi$=0 can be estimated for a single beamlet in cylindrical approximation from the set of balance equations for plasma electrons and ions quasi-neutrality conditions per unit length

[47]:

$$n_{H^-} \upsilon_{H^-} n_{acr} \sigma_i \pi r_0^2 = n_i \upsilon_i 2\pi r_0$$
$$n_{H^-} \upsilon_{H^-} n_{acr} \sigma_e \pi r_0^2 = n_e \upsilon_e 2\pi r_0 \qquad (5.1)$$
$$n_{H^-} + n_e = n_i$$

where n_{H^-}, n_i, n_e and n_a are the densities of the beam ions, plasma ions, electrons and neutral gas particles; σ_i and σ_e are the cross sections, respectively for the production of positive ions and electrons; υ_i and υ_e are the average transverse velocities of plasma ions and electrons produced in collisions of the beam ions with neutral gas particles; υ_{H^-} is the average velocity of the beam ions with respect to the particles of the background gas and r_0 is the beam radius. For the critical density of neutral particles, by assuming $n_e \ll n_i$ or $n_{H^-} \approx n_i$, it yields:

$$n_{acr} = \frac{2\upsilon_i}{\upsilon_{H^-} r_0 \sigma_i \left(1 - \frac{\upsilon_i}{\upsilon_e} \frac{\sigma_e}{\sigma_i} \right)} \approx \frac{2\upsilon_i}{\upsilon_{H^-} r_0 \sigma_i} \qquad (5.2)$$

It must be noted that this cylindrical approximation neglects the presence of boundaries along the axial direction, and it is therefor evalid when radial transport dominates the axial one. This is the case for instance of long drift regions and a relatively small effective radius of the drift tube. It also does not consider the presence of biased boundaries that may influence or even dominate the transport of secondary charges. Furthermore, in the single-beamlet radial approximation recycling of compensating species among adjacent beamlets is neglected. Finally, the drift velocities υ_i, υ_e shall account for differential cross sections describing the initial energy distribution of secondary charges and they shall account for slowing-down by collisions with neutral (plasma diffusion). For all these reasons, a kinetic model will be used to describe the beam plasma formation as described in the following section.

5.2   Model description

The Particle-In-Cell method refers to a technique used to solve the partial differential equations by means of individual particles, or fluid elements, in a Lagrangian frame tracked in a continuous phase space. In this space, densities and currents are computed simultaneously on Eulerian (stationary) mesh points. In order to simulate a real system as efficiently as possible, a large number of particles is needed. For this reason the so-called *macro-particles* are used: these are computational particles that represent many real particles. Since the Lorentz force depends only

on the charge-to-mass ratio, this approximation is allowed and a macro-particle will follow the same trajectory as a real particle would. The name Particle-In-Fields originates in the way that plasma macro-quantities, such as number density and current density, are assigned to simulation particles which can be situated anywhere on the continuous domain, but macro-quantities are calculated only on mesh points, just as the fields are. The time and the domain in which the macro-particles move is discretized. The time is divided in time steps, in which particle motion and consequently changes in the charge density and electric potential are simulated. The space instead is subdivided into cells forming a grid, whose extremes are called nodes. Each particle generated in each cell is characterized by its charge and mass and it is generated with a temperature and a velocity.

In order to calculate the charge density inside each cell, the charge of each particle generated inside the cell is deposited at its extremities as shown in figure 5.1.
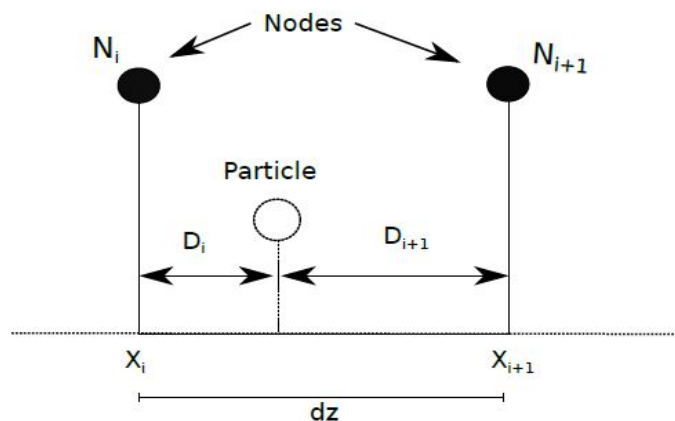
Figure 5.1: *Representation of charge deposition on grid node.The particle charge Q is divided by weighting it on the distances from the nodes. At the node N_i a portion of the charge QD_{i+1} is deposited, while at node N_{i+1} is deposited QD_i charge.*

It is now possible to solve the Poisson equation to compute the electrostatic fields at each node by using the quantity of charge deposited by each particle, generated inside it. By knowing the particle positions and the fields at each node, it is possible to calculate the forces acting on particles. At each particle position the fields are exactly calculated by interpolating the value of the potential. It is now possible to move the particles by using the Boris method [49] to integrate their trajectories.

5.2.1   2D-3V PIC-MCC Code gppic

2D-3V PIC-MCC stands for a 3 dimensional model for the positions and the velocities in which the Poisson equation is solved bi-dimensionally, merged with Monte Carlo Collision. In the model [1] five species of particles are included: H^-, H^0, H^+, H_2^+ and electrons. These move in a background gas of H_2 at a constant density n_g in the domain, determined by the source pressure imposed. At the beginning H^- beamlets are injected from the left at a given energy. To identify the occurrence of collisions with the background gas the null collision method is used [50]. The set of collisions included are reported in table 5.1 while their cross sections are shown in figure 5.2.
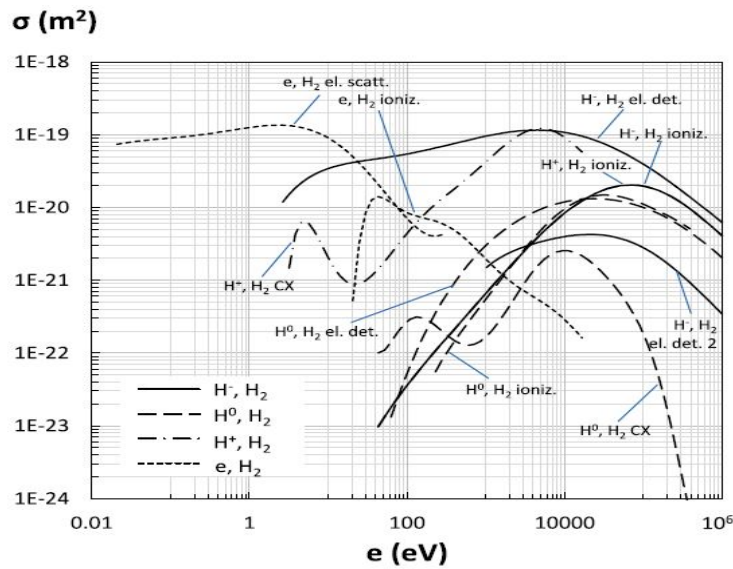
Figure 5.2: *Cross sections for the processes included in the model [51].*

H^-, H_2	H_0, H_2	H^+, H_2	H_2^+, H_2	H_3^+, H_2
$H^+, 2e^-, H_2$	H^+, e^-, H_2	H^+, H_2^+, e^-	H^+, H^0, H_2	H^0, H_2^+, H_2
H^0, e^-, H_2	H^-, H_2^+, e^-	H^0, H_2^+	H_3^+, H^0	H_2, H^+, H_2
H^-, H_2^+, e^-	H^-, H_2^+	H^+, H^+, e^-, H^0	H_2, H_2^+	H^+, H_2, H_2
H^-, H^+, e^-, H^0	$2H^0, H^+, e^-$	H^+, H_2	H_2^+, H_2	H_2^+, H^0, H_2
$H^-, H^+, H^+, 2e^-$	$H^0, H^+, H^+, 2e^-$	$3H^+, 2e^-$		H_3^+, H_2

Table 5.1: *List of the interactions considered in the model.*

The geometry is approximated to a bi-dimensional domain and it is shown in

figure 5.3, where the boundary conditions and region used to approximate the RFEA and Langmuir probes are also reported.
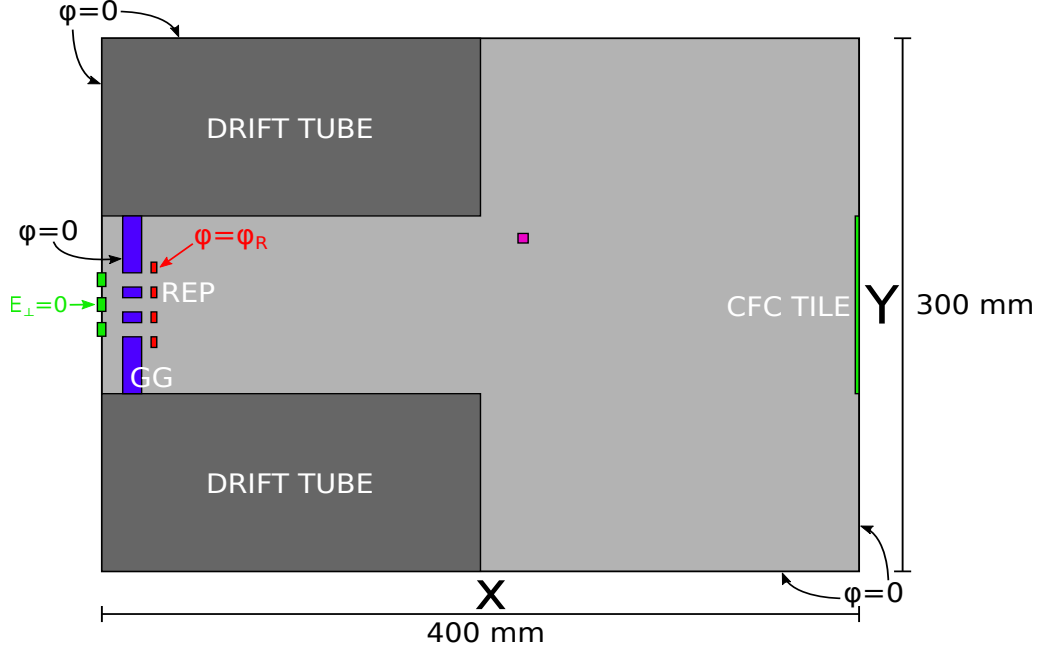
Figure 5.3: *Domain of the model simulated. The pink box represents the region used to approximate the RFEA and Langmuir probes.*

The domain included the Grounded Grid (the PA in NIO1) and the Repeller on the left-hand side and the CFC tile on the right-hand side. The drift tube is also included. The entire domain is 400 mm long and 300 mm high. Neumann boundary condition with zero perpendicular E field is applied on the left-hand where the beam crosses the boundary. This approach neglects the formation of the diverging electrostatic lens usually formed at the exit of the PA. For this reason a correction to the beamlet optics is needed as it will be shown in the following. The PIC is implemented is a C++, CUDA based code in order to exploit the GPU parallelization to simulate dense and regular mesh. It exploits a sparse matrix implementation from cusp library [52] for solving Poisson equation. By modifying the Poisson equation Dirichlet and Neumann conditions are applied. In the simulations shown in the following, a grid uniform spacing $\Delta x = \Delta y = 1\ mm$ and a time step $\Delta t = 1\ ns$ are used. The weight of a macro-particle is $0.5 \times 10^5\ particles$. These choices fulfill the conditions

$$\Delta x < 3.4 \lambda_D$$
$$\Delta t \leq 2\omega_{pe}^{-1}$$

(5.3)

where λ_D is the Debye length and ω_{pe}^{-1} the inverse plasma frequency which define the natural time scale in the plasma. These constraints are fundamental to properly simulate the time and length scale of the real plasma. The 5 species are shown in figure 5.4 at t=50 μs.
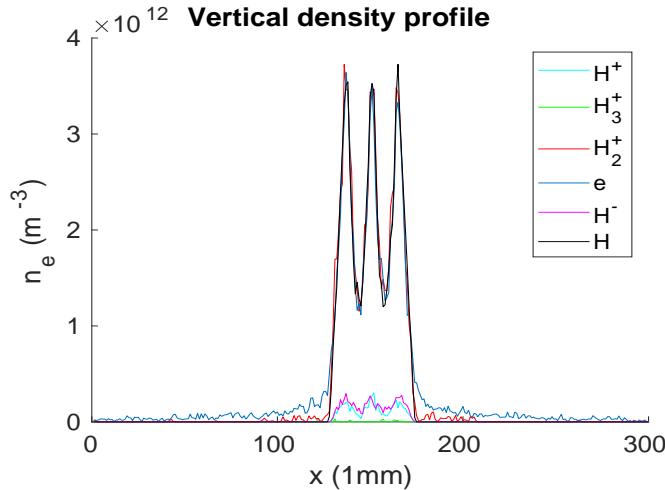
Figure 5.4: *Vertical density profile of the five species simulated at 50 mm from the Repeller.*

5.2.2 Beam optics correction

The left boundary of the simulation domain cuts the accelerator between the EG and the PA. At the cut section, the electric potential is assumed to be constant V_0 and uniform, and it is determined according to

$$V_0 = \frac{V_{EG}}{z_{PA} - z_{EG}} \times z'_{PA} \qquad (5.4)$$

where z_{PA}, z_{EG} are the coordinates of the upstream and downstream surfaces of the PA and EG respectively, and z'_{PA} is the coordinate in the simulation domain of the upstream PA surface. In the simulation, the ion beam particles are therefore injected halfway to full acceleration, and their trajectory shall somehow include the "missing" part of the accelerator. In order to do that, it will be assumed that the transverse ion beam velocity after the accelerator is minimized. The initial velocities will therefore be compensated for by including the diverging effect of the PA apertures. The beam expansion under the influence of the space charge is compensated for by carefully shaping the electrode aperture along the accelerator. In fact, an aperture with different electric fields on its sides can be considered as an electrostatic lens which acts on charge particles crossing it (see figure 5.5).
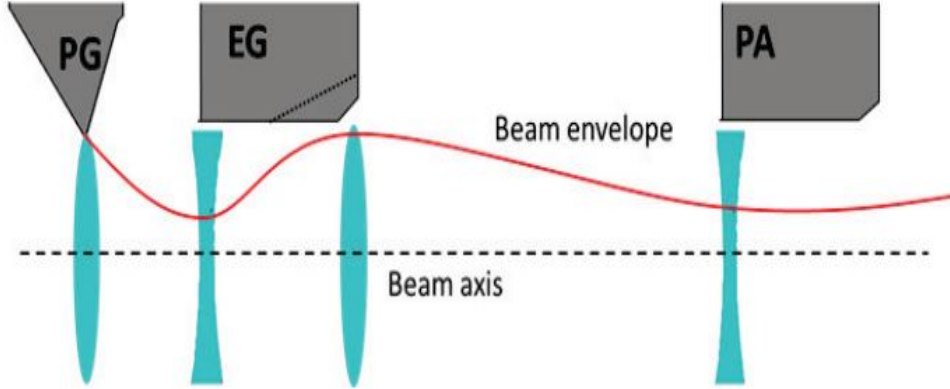
Figure 5.5: *A scheme of NIO1 beam optics assuming cylindrical symmetry with equivalent converging and diverging lens.*

In particular, a divergent lens is formed at the EG entrance and a convergent lens at its exit. The effect of both lenses can be described by using the so-called *thin lens approximation*. For the resultant focal length it yields [53]

$$f = \frac{4V(z_i)}{E_d - E_u} \tag{5.5}$$

where $V(z_i)$ is the potential at the electrode position and E_d and E_u the electric field values downstream and upstream of the electrode respectively. It is clear that the condition $E_d > E_u$ gives a converging lens that is opposed to the beam expansion induced by the space charge. The focal length of the diverging PA lens is calculated and a converging focal length is given to the newly generated beam ions entering from the left boundary. Since accelerators are designed aiming to produce a parallel beam after the PA, the optics of the beam entering in the domain is assumed to be optimized. In addition to this, in view of the nature of the source, there is always a spread in kinetic energy and velocity in a particle beam. Each point on the surface of the source is emitting particles with different initial magnitude and direction of the velocity vector. This intrinsic thermal velocity remains present in the beam at any distance downstream from the source and it may be considerably greater than the ideal thermal limit. Above the parameters that can contribute to it, there are temperature fluctuations in a plasma source, non-linear forces due to external or space-charge fields. The *emittance* provides a quantitative basis, or a *figure of merit*, for describing the quality of the beam. It is a measure for the average spread of particle coordinates in position and momentum phase space. As a particle beam propagates along magnets and other beam

manipulating components of an accelerator, the position spread may change but in a way that does not change the emittance.

In order to improve the beam focus in the model, the way in which the component along the y direction of position and velocity are generated has been changed. At first the y coordinate was generated uniformly between the PA holes of 3 mm radius. The velocity along the y direction v_y instead was generated normally distributed with the Gaussian amplitude determined by the thermal energy spread. The y position is now sampled using the inverse cumulative method. By considering a cosine distribution of the beam particles inside the beam region, the arcsine is used to extract the y coordinate (see figure 5.6).
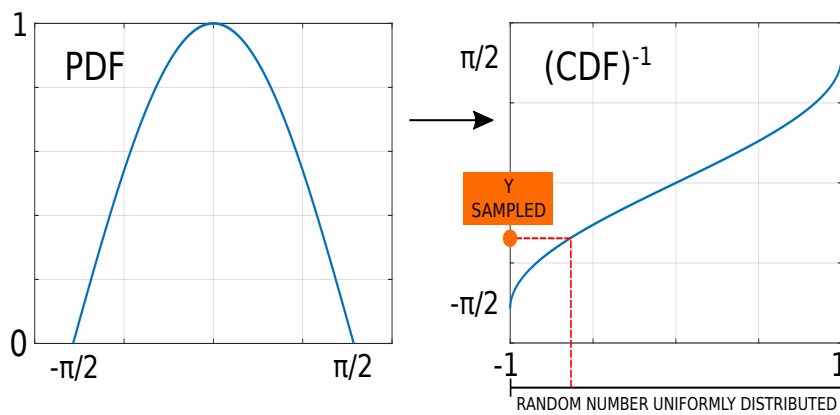
Figure 5.6: *Inverse CDF sampled method.*

This correction has been introduced in order to compensate for the non-uniform radial density of the beam produced inside the accelerator, which is not included in the simulated model. Concerning the velocity along the y direction, an emittance approximated as a straight line is introduced. The slope of the line is determined by the thermal spread plus a corrective factor introduced by considering the thin lens approximation (eq. 5.5). Hence, the i-th coordinate and velocity along the y direction are generated by:

$$y_i = \frac{(y2 - y1)}{2} \times \frac{2}{\pi} \arcsin(-1 + 2U(0,1))$$
$$v_{yi} = K \times y_i \tag{5.6}$$

where y_1 and y_2 are the extremes of each beamlets, $U(0,1)$ is the uniform distribution and $K = div\sqrt{\frac{qE}{mass}}1/y_{max}$ with div determined using the thin lens approximation calculated on the PA:

$$div = \frac{y_2 - y_1}{2} \times \frac{E_d - E_u}{4V_{AG}} \tag{5.7}$$

5.3 Comparison between experimental data and PIC model results

At first the data collected by the electrostatic probes, the Langmuir and the RFEA, will be compared with the simulation results. The first measures the electronic temperature in a region inside the vessel but out of the path of the beam. It can also estimate the plasma ion density. The RFEA probe instead is used both to collect electrons and ions. It gives information about energy distribution of the charges, both electronic and ionic, from which information about the radial plasma potential profile and sheath could be inferred. The data has been collected at different pressure and with different CFC tile and Repeller voltage of polarization. To conclude, an estimate of the radial diffusion coefficient is obtained from the model and compared with the light diffusion profile collected by the visible camera.

5.3.1 Langmuir Probe

As already mentioned in section 2.3.5, the Langmuir probe used during the experimental campaign is situated at almost 10 cm from the center of the beam. The electronic temperature is calculated from the Langmuir probe characteristic using an exponential fit to the electron current in the region between the floating potential and the plasma potential. This method assumes a single temperature Maxwellian which is not always the case. However, it is assumed that the Langmuir probe resolves the dominant low energy electron population which itself is close to Maxwellian equilibrium. The double Maxwellian distribution is a useful model to describe the non-equilibrium population at higher energy where the collisions play a non negligible role, as it will be shown for the data collected by the RFEA probe.

To compare the temperature measured by the Langmuir probe with the data obtained by the simulation, the average kinetic energy of the simulated particles is calculated in a region of the domain, at a distance from the beam proportional to the real distance of the Langmuir probe from the beam. The region considered is shown in figure 5.3.

The comparison has been made at different vessel pressures and at different acceleration voltages. Furthermore, different bias voltages of the CFC tile and of the Repeller have been compared, in order to investigate the effect of this polarization on the beam plasma development. In table 5.2 the estimates of the electronic temperatures from the fit of the experimental data and from the numerical simulation are compared. The region of the domain considered is included between (215:225,165:175).

The data does not match perfectly. By fitting the data collected by the Lang-

Vessel press. (mPa)	V_{CFC} (V)	T_e Langm. (eV)	T_e model (eV)
31	2	6.1	6.9
31	60	7.4	1.2
500	2	3.3	0.9

Table 5.2: *Comparison between the results obtained from the experimental data and from the model.*

muir probe it is possible to achieve the ionic density through

$$n_i = 1 \times 10^{-6} a \times 2 \sqrt{\frac{m_i}{T_e \times 1.6 \times 10^{-19}}} \frac{1}{Area \times 1.6 \times 10^{-19}} \tag{5.8}$$

where a is the so-called ion saturation current (one of the fitting parameters). This fit considers only the contribute due to the ions H_2^+, which indeed forms the majority of the positive ion population. In the numerical simulation the density is estimated by counting the number of macroparticles situated in the considered domain for unit of time and area and by dividing it for the ionic Bohm velocity. Also the ionic density estimated are quite different. In table 5.3 the densities

Vessel press. (mPa)	V_{CFC} (V)	n_i Langm. ($1/m^2$)	n_i model ($1/m^2$)
31	2	1.44×10^{12}	7.9×10^{12}
31	60	7.48×10^{11}	5.9×10^{12}
500	2	1.29×10^{13}	1.32×10^{14}

Table 5.3: *Comparison between the results obtained from the experimental data and from the model.*

estimated from the numerical simulation take into account the contribute of all the positive ions (H_2^+, H_3^+, H^+).

5.3.2   RFEA Probe

The RFEA probe used during the experimental campaign is situated at almost 10 cm from the center of the beam. By polarizing the RFEA probe as shown in figure 5.7, it can attract both positive ions and electrons, depending on the voltage applied to the grid. Since in the simulation the edge of the domain is not polarized, in order to simulate the attraction generated by the probe layer polarization, a comparison between the data collected and the data obtained from the simulation can be achieved by considering the vertical velocity of the particles
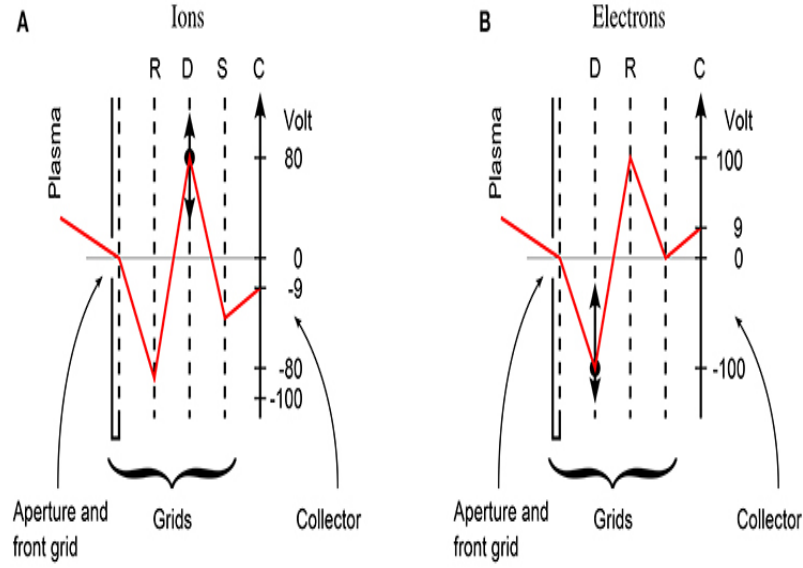
Figure 5.7: *RFEA grid configurations for (A) ion measurements and (B) electron measurements.*

which exit from the domain. Due to the boundary condition imposed however, the domain regions above and below the CFC tile in the lateral wall and the drift tube are grounded. Hence the beam plasma drifts more easily towards these regions with respect to the lateral walls. For this reason, in the following an intermediate region between the lateral wall and the beam region will be considered to compare the data collected by the RFEA with the numerical simulation (see figure 5.3).

Electronic measurements

When the field configuration is in the (B) condition reported in the figure 5.7 a measure of the electron parameters can be achieved. By measuring the current impinging on the collector, an estimation of electronic temperature is obtained. Due to probe structures, only the radial component of the energy can be measured. It is assumed that the electron energy distribution is related to a Maxwellian with characteristic temperature T. The electron temperature can be extracted by plotting the logarithm of the mean current against the retarding potential. The slope is

$$\frac{d(ln(I_{COLL})}{d(V_{RET})} = \frac{e}{k_B T}. \tag{5.9}$$

This behavior is confirmed by the data collected at high pressure, namely when the cryogenic pumps are off. Electrons in plasmas are much more mobile than ions and consequently their fluxes are much greater. Because of this, materials in

contact with plasma will generally charge negatively with respect to the plasma. The region adjacent to the material wall is schematically shown in figure 5.8.
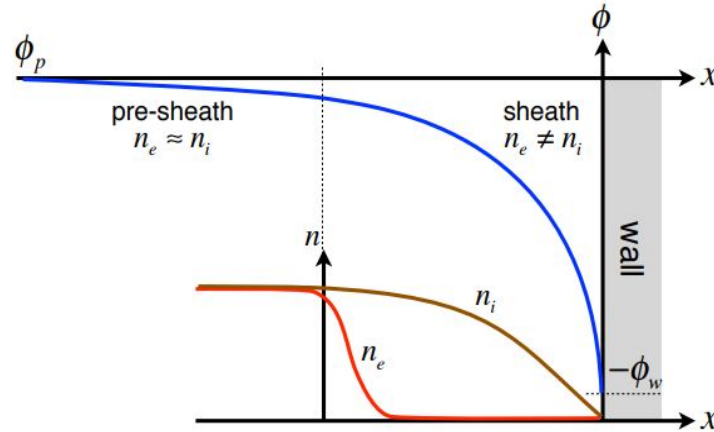
Figure 5.8: *Schematically representation of the plasma region adjacent to the material wall.*

On the order of the inverse of the plasma frequency, the potential reaches an equilibrium as the current densities of electrons and ions become equal. The distribution function of ions is therefore far from uniform in the sheath, the distributions of the electrons can still be considered to be close to a Maxwellian.
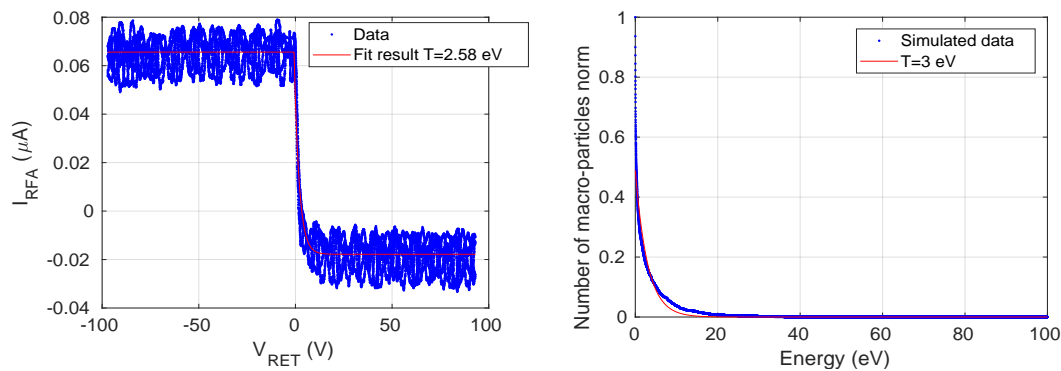
Figure 5.9: *Comparison between electronic temperature estimated from the experimental data collected by the RFEA (left side) and the data simulated (right side) in high pressure.*

An example of Maxwellian electronic temperature is shown in figure 5.9. The data were collected with the cryogenic pumps off and without the CFC tile polarized. In particular, the data were collected with 500 mPa of vessel pressure, 0.8 of

source pressure, V_{AGPS}=2.5 kV, V_{EGPS}=350 , I_{PGF}=10 A, RF Power=1.2 kW, PG Bias=45 V, I_{BB}=0.2 A, $V_{CFC} = V_{REP}$=2 V. As expected, at this high pressure, the electronic temperature is approximatively Maxwellian, due to the high number of interactions with the background gas. Figure 5.9 also reports the exponential fit of the temperature of electrons escaping from the lateral side of the domain considered. Only the component along the y direction of the electronic energy is considered. The two results are in good agreement. A more impressive chart can be obtained by plotting the logarithmic of the current measured by the probe and of the number of particles exiting from the domain of the numerical simulation. These plots are shown in figure 5.10.
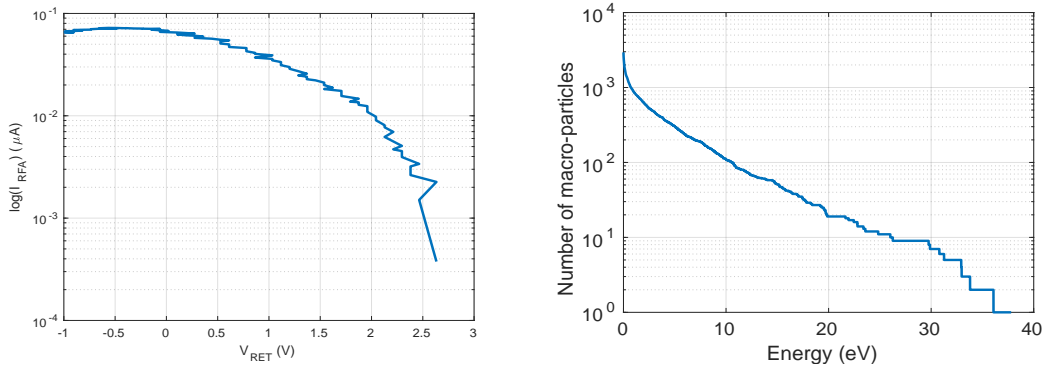
Figure 5.10: *Comparison between electronic temperature estimated from the experimental data collected by the RFEA (left side) and the data simulated (right side) in high pressure in semilogarithmic scale.*

When the cryogenic pumps are on, instead, the number of collisions of the electrons is considerably reduced. In fact, the vessel pressure is reduced by a factor of 10. The beam particles undergo collisions with the background gas, resulting in electronic stripping or also double electronic stripping. At this low pressure, the mean free path of these electrons is higher enough to allow the high energy tail of electron distribution to reach the plasma edge. By a simple calculation, for pressure in the order of 30 mPa and by considering, for collisions of negative hydrogen against molecular hydrogen, the total scattering cross sections $\sim 1 \times 10^{-20}$ in the energetic range of interest (about some keV), it can be shown that the electronic free mean path is $\lambda \sim 1\ m$. Co-accelerated electrons leaking from the accelerator could directly reach the RFEA entrance grid, with only their energy component perpendicular to the RFEA grid being measured. Plasmas at low gas pressures are always in a non-equilibrium state. In particular, electrons might not be in a thermal equilibrium with neutral species and ions. Indeed, the electron temperature is usually much larger than the temperature of ions and of

neutrals. In addition, electrons may not even be in equilibrium within their own ensemble, which results in a significant deviation of electron energy distribution function from the equilibrium Maxwellian distribution.

This behavior is shown in the data collected by the RFEA when the cryogenic pumps are on. In figure 5.11 a fit of the electron RFEA characteristic with two different temperatures is shown.
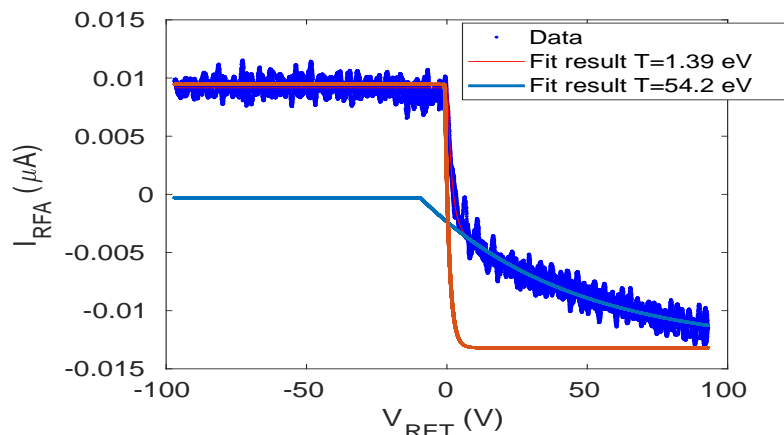
Figure 5.11: *Electron characteristic measured by the RFEA at low pressure.*

The data reported in figure 5.11 were collected with 31 mPa of vessel pressure, 0.55 Pa of source pressure, V_{AGPS}= 7 kV, V_{EGPS}=750 V, I_{PGF}=10 A, RF Power=1.2 kW, PG Bias=45 V, I_{BB}= 0.1 A, $V_{CFC} = V_{REP} = 60$ V. This high energy tail is dependent on the acceleration voltage, upon which the energy of the accelerated beam depends. A set of measurements take in the conditions described above and varying V_{AGPS} are shown in figure 5.12.
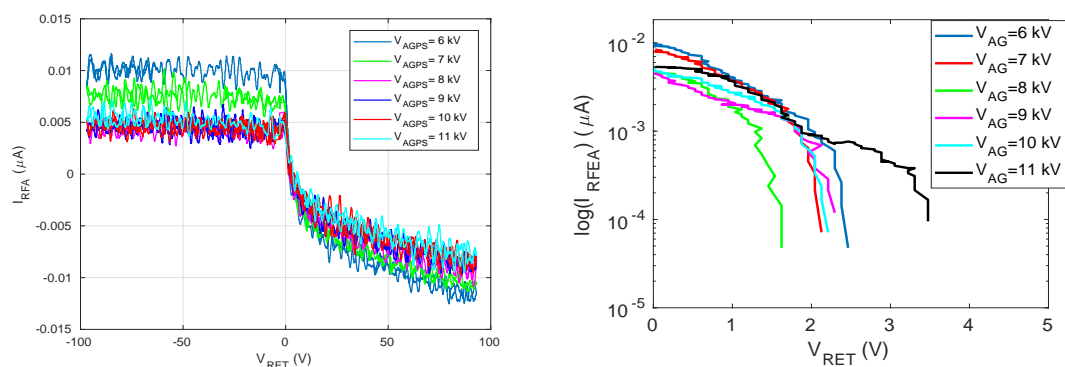
Figure 5.12: *Electron characteristic measured by the RFEA as a function of V_{AGPS} (left side) and in logarithmic scale (right side).*
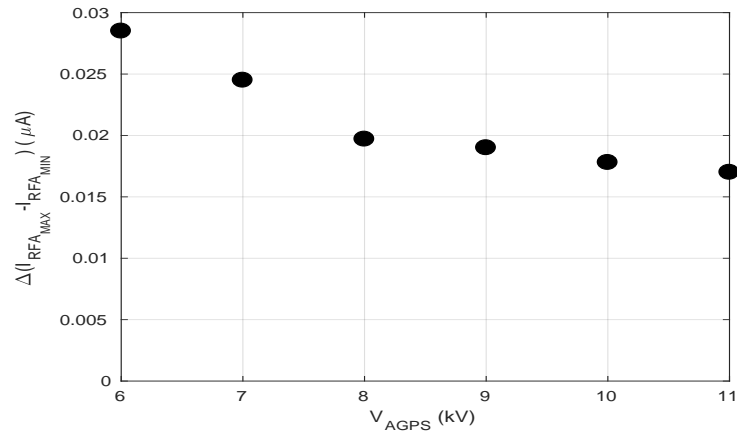
Figure 5.13: *Difference between the highest and lowest I_{RFA} collected as a function of V_{AGPS}.*

The difference between the highest and lowest I_{RFA} collected as a function of V_{AGPS} is reported in figure 5.13.

These high energy electrons which can be produced inside the acceleration column are not taken into account in the numerical simulation. This is confirmed by measuring the energy of the electrons with the vertical component of the velocity high enough to achieve the lateral wall of the selected region. The electron energy characteristic obtained from the model in fact does not show this high energy tile. The energy distribution of the electrons that escape from upper wall of the simulation is shown in figure 5.14.
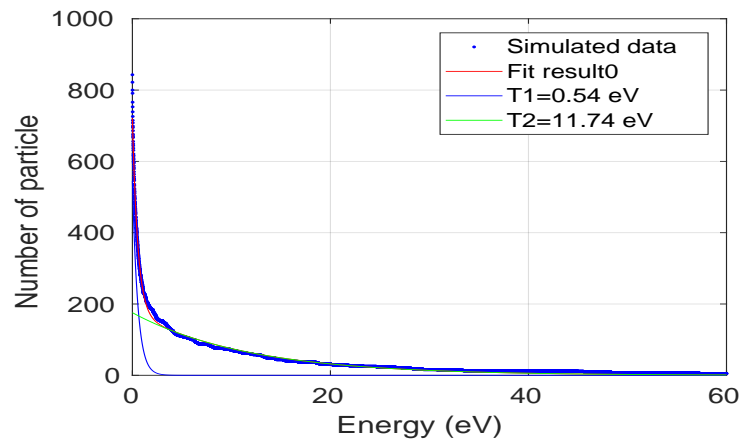
Figure 5.14: *Electron characteristic obtained from the numerical simulation.*

Here, the temperatures obtained are really different from the ones measured by the RFEA, as expected. However, if the higher energy tail of the measures obtained from the RFEA is not considered and only the thermalized population is compared, the two results are consistent, as shown in figure 5.15.
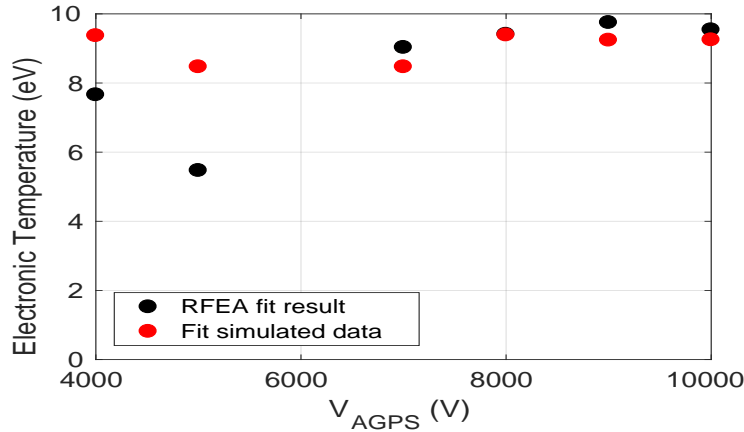
Figure 5.15: *Comparison between electronic temperature estimate from the RFEA data and from the model simulated.*

Ionic measurements

The main goal of the RFEA is to measure the positive ions in the plasma sheath. Qualitative information can therefore be obtained by comparing the RFEA ionic characteristics and the profile obtained from the simulation. In particular, the effect of the CFC Tile and the Repeller polarization play an important role. In fact, the number of positive ions reaching the RFEA probe or, analogously, the wall of the simulation domain, change significantly. When the cryogenic pumps are on, the number of ions measured by the RFEA probe is practically zero; hence in the following, only cases with high pressure will be discussed. The current collected by the RFEA probe can be expressed as

$$I(r) = \overrightarrow{j} \cdot \overrightarrow{A_{coll}} = \frac{n(r)ec_s A_{coll}}{\gamma^4} \qquad (5.10)$$

where $A_{coll} = 0.5 \times 10^{-2} \ m^2$ is the collector area, $\overrightarrow{A_{coll}}$ is its normal vector, c_s is the Bohm velocity defined as $c_s = \sqrt{\frac{k_B T_e}{m_i}}$ and γ is the single grid transparency which for the RFEA used it is equal to 0.356. A quantitative comparison between the data collected by the RFEA probe and the results of the simulation can be

achieved by comparing the density of current measured. The density of current of the numerical simulation is calculated by

$$j = \frac{NMPW}{Adt} \tag{5.11}$$

where N is the number of macroparticles exiting from the lateral wall of the domain, MPW is the weight of one macroparticle (0.5×10^5 particles), $A = 0.15 \times 1 \ m^2$ the area of the region selected. Considering first the data collected when the CFC tile and the Repeller are polarized at 60 V. The comparison between the two densities estimated is shown in figure 5.16.
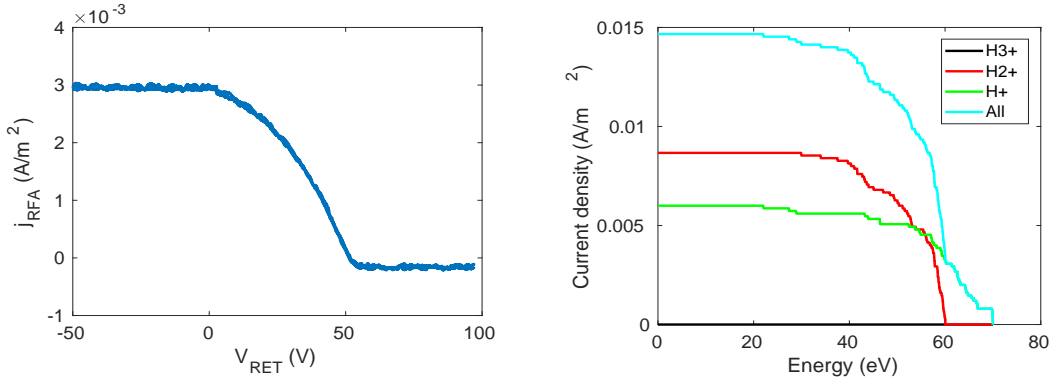
Figure 5.16: *Comparison between density of current collected by the RFEA (left side) and the data simulated (right side) in high pressure.*

The data were collected by the probe with 350 mPa of vessel pressure, 0.6 Pa of source pressure, V_{AGPS} =6 kV, V_{EGPS} =600 V, I_{PGF}=10 A, RF Power=1.2 kW, Bias PG=45 V, I_{BB}=0.2 A, $V_{CFC} = V_{REP}$ =60 V. The measure made by the RFEA is lower because of its smaller dimension with respect to the wall of the simulated domain. In addition, the potential imposed in between the grids filters the particles with respect to the angle in which they enter in the probe, while in the simulation this cut is not present. Also the data with the Langmuir probe at these conditions were collected. The two temperatures estimated are:

$$
\begin{aligned}
Fitted \ T_e &= 19 \ eV \\
Simul. \ T_e &= 11 \ eV
\end{aligned}
\tag{5.12}
$$

Even the measure of the density of positive ions can be compared. From the simulation it is possible to calculate all the ionic populations in the region considered. By comparing the results, an agreement is found:

$$
\begin{aligned}
Fitted \ n_i &= 1.43 \times 10^{13} \ 1/m^3 \\
Simul. \ n_i &= 1.3 \times 10^{13} \\
&\quad 1/m^3
\end{aligned}
\tag{5.13}
$$

It is now possible to compare the ionic characteristic in the case when the CFC tile and the Repeller voltage of polarization is low. In this condition, the secondary emission of electrons due to fast ion impact on the CFC tile is not reabsorbed by the high polarization voltage of the tile. Furthermore, the plasma electrons are not attracted by the CFC tile and the amount of electrons does not decrease. Hence, it is possible that the beam plasma potential is not positive with respect to the grounded walls, and the sheath layer is inverted. In such condition the positive ions reach the vessel walls (and the RFEA) without being accelerated by the plasma sheath. The data collected with high pressure and $V_{CFC} = V_{REP} = 2$ V are shown in figure 5.17 when varying of the source pressure. The vessel pressure varies proportionally with respect to the source pressure.
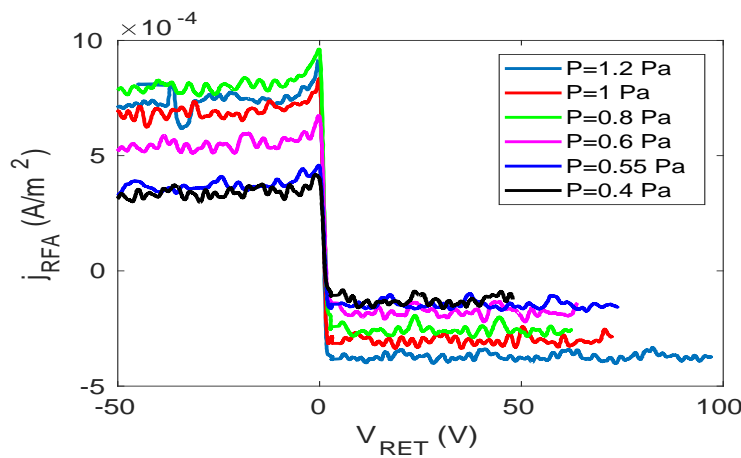
Figure 5.17: *Density of ionic current collected by the RFEA probe as a function of the source pressure.*

The data were collected with $V_{AGPS} = 5$ kV, $V_{EGPS} = 600$ V, RF Power=1.2 kW, $I_{PGF} = 10$ A, $I_{BB} = 0.2$ A, PG Bias=45 V, $V_{CFC} = V_{REP} = 0.8$ V and with vessel pressure ranging from 230 mPa to 880 mPa. In figure 5.17 an increase of the density current measured with the increase of the source pressure, and consequently of the vessel pressure, is evident. However, the ionic energy measured is almost zero, as it is shown by all the characteristic centered on 0 V of retarding voltage. This behavior is confirmed by the results obtained from the simulation.

In figure 5.18 the ionic and electronic density of current are reported. These charts confirmed what said before about the effect of the CFC tile polarization on the beam plasma. The data reported has been simulated at the same conditions as the data reported in figure 5.16; the only difference is the different voltage of polarization of the CFC tile (and Repeller). The ionic estimated density current is almost 3 orders lower than the density current measured with 60 V on the CFC
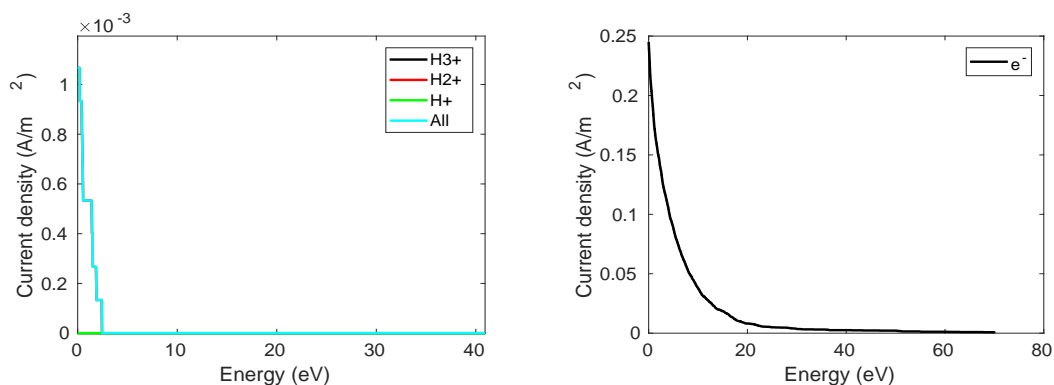
Figure 5.18: *Comparison between ionic and electronic density current measured through the lateral wall of the simulated domain.*

tile. The electronic density, instead, is not affected by this decrease, as expected. This difference can also be seen by comparing the potential map in these two different conditions. This comparison is shown in figure 5.19. It is evident that
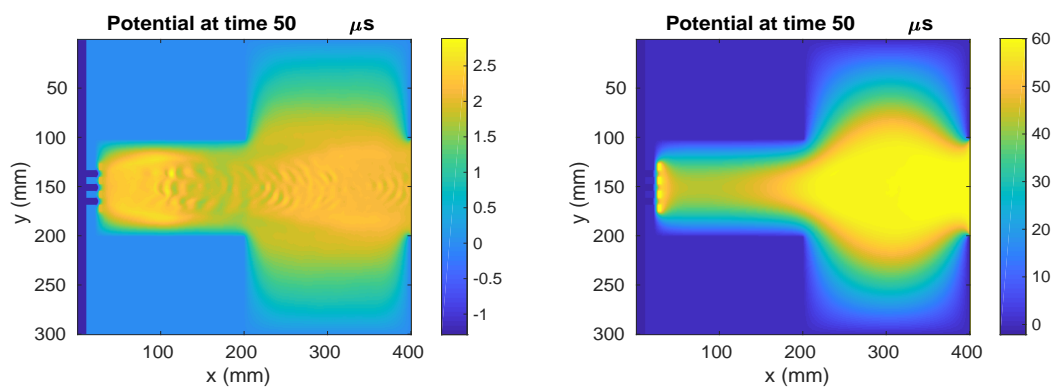
Figure 5.19: *Comparison between the potential map at the same time and conditions but with V_{CFC}=2 V (left side) and V_{CFC}=60 V (right side).*

the two potential maps are different, confirming what has been said before.

5.3.3   Diffusion estimation

A plasma density profile from the beamlets to NIO1 vessel can be estimated by comparing the results obtained with the model simulated and by analyzing the profile of the images collected by the two visible camera and by the RFEA probe. NIO1 vessel can be approximated to a cylindrical shaped wall which confines a low density plasma with an unknown density profile. The negative ion beam can be considered as a plasma source with radius $r_0 < r_{vessel}$. By assuming only radial dependency, the radial diffusion toward the vessel is described by

$$\frac{\partial n(r)}{\partial t} - D\nabla^2 n(r) = -D\nabla^2 n(r) = -G_0,$$
(5.14)

where n is the plasma density, D is the plasma diffusivity and G_0 is the source therm. The homogeneous solution is

$$n(r) = A ln\left(\frac{r}{R}\right) + B$$
(5.15)

where R represents the edge of the compensation plasma region. In the following, only the region between the beamlets and the plasma edge will be considered. In this region can be considered zero the source term, since the secondaries are mainly produced in the beamlets region. To determine the constants A and B, the boundary condition has to be defined. The relation between particle flux and particle density in the pre-sheath is

$$n(R) = B = \frac{\Gamma(R)}{c_s}$$
(5.16)

where c_s is the Bohm velocity, defined as $c_s = \sqrt{\frac{k_B T_e}{m_i}}$. Using the Fick's law $\Gamma = -D_a\nabla n$ evaluated in R, where D_a is the ambipolar diffusion coefficient, the term A can be obtained:

$$A = -\frac{\Gamma}{D_a}R$$
(5.17)

Hence the radial density profile, outside the beamlets region, is expected to be described by

$$n(r) = -\frac{R\Gamma(R)}{D_a}ln\left(\frac{r}{R}\right) + \frac{\Gamma(R)}{c_s}$$
(5.18)

By fitting the emissivity profile of the data collected from the cameras, outside the beam region, the ambipolar diffusion value can be estimated. By evaluating the

flux term at a distance R from the centre of the beam region, the radial density profile becomes

$$n(r) = \frac{I_B n_{bkg} \sigma_{iz}}{2\pi R q} \left[-\frac{R}{D_a} ln\left(\frac{r}{R}\right) + \frac{1}{c_s} \right] \tag{5.19}$$

where I_B is the total beam current, n_{bkg} the density of the background gas, σ_{iz} the H^-, H_2^+ scattering cross section and c_s the Bohm velocity.

In the actually NIO1 energetic performance, an ambipolar diffusion can be approximated only in the high pressure range. In the source pressure scan presented in chapter 3, from the images collected from the camera an increase of the amount of particle drifting toward the lateral wall from the beam region is evident. The image considered is reported in figure 5.20; the beam parameters are V_{AG} 5 kV, V_{EG}=600 V, P=0.6 Pa, I_{PGF}=10 A, RF power=1.2 kW, I_{BB}=0.2 A, Bias PG=45 V, cryo off, $V_{CFC} = V_{REP}$=60 V.
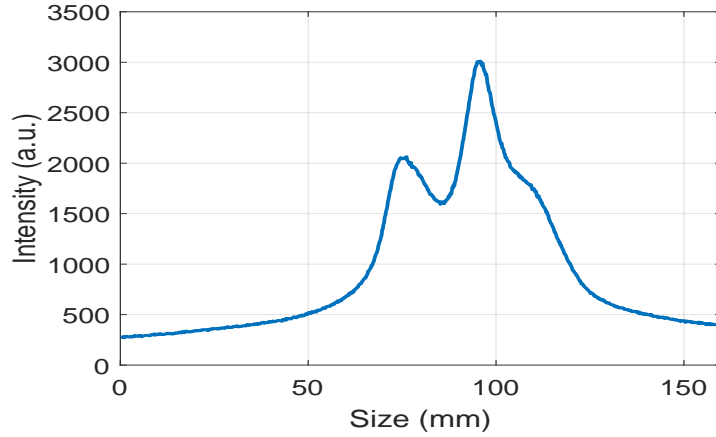
Figure 5.20: *Image considered.*

At this energy $\sigma_{iz} \sim 4 \times 10^{-20}$ m^2, the beam current used is the current measured by the CFC tile, on the order of some μA, the $T_e \sim 4$ eV estimated from the numerical simulation and the radius considered is $R \sim 51$ mm. By assuming that the emittance measured from the camera is directly proportional to the profile density, the profile of the data collected from the camera can be fitted with 5.19. The result obtained is shown in figure 5.21.

The ambipolar diffusion coefficient estimates is equal to $2.5 \times 10^4 m^2/s$. The assumption of ambipolar diffusivity is just an approximation. In fact, in the numerical simulation, the flux of electrons and ions along the y direction, representing the radial direction, is not compensated. The positive voltage applied to the CFC tile attracts the electrons while rejects the positive ions. An estimation of the diffusion coefficient can be achieved from the density profile obtained by the numerical
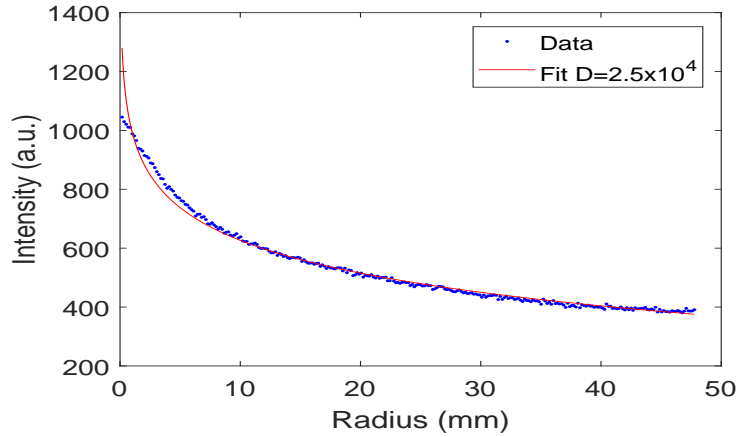
Figure 5.21: *Fit of the density profile collected by the camera.*

simulation. In particular, the data reported in figure 5.26 are simulated in similar conditions with respect the image used previously. From the axial (horizontal) and radial (vertical) density profiles an estimation of both the axial and radial diffusion coefficient for electrons and positive ions has been made. The diffusion coefficients estimated for both positive ions and electrons are:

$$
\begin{aligned}
D_{a,e,radial} &= 0.5 \times 10^4; \\
D_{a,e,axial} &= 1.02 \times 10^7; \\
D_{a,H_2^+,radial} &= 0.5 \times 10^4; \\
D_{a,H_2^+,axial} &= 1.02 \times 10^7;
\end{aligned}
\tag{5.20}
$$

The two diffusion coefficient are different, due to the non-ambipolarity of the system. In fact, the total flux of positive and negative charges through the domain walls is not compensated

$$
\int_S \Gamma_i - \Gamma_e \neq 0.
\tag{5.21}
$$

This has been confirmed also from the data collected by the RFEA probe. Indeed, when the CFC tile is polarized, the number of positive ions which reaches the probe is very higher with respect to the number of electrons; the opposite when the voltage of polarization of the CFC tile is low.

5.4   Numerical simulation as a predictive tool

Since it has been shown that the code well represents the experimental data, it can be used now to study plasma properties which can not be directly measured. Among these, the degree of beam self-potential compensation, the emittance profile, the effect of the Repeller on the quantity of positive ions backscattering, the beam plasma density and potential profile evolution.

Degree of beam self-potential compensation

A beam self-compensation degree ψ can be defined from the potential U at a given time and the potential U_0, generated by the beam charges only

$$\psi(t,y) = 1 - \frac{U(t,y)}{U_0(t_0,y)};$$
$$(5.22)$$

in the following U_0 potential is considered as the potential present at $t_0 = 4$ μs, which is such a fraction of the characteristic time for compensation $\tau_C = 1/(n_g \cdot \sigma_{ioniz} \cdot v_{beam})$. The beam self-potential compensation as a function of time and y position is computed at two different x coordinates: at x=150 mm in the drift tube and at x=350 mm close to the CFC tile. The numerical simulation was made with 31 mPa of vessel pressure, $V_{CFC} = V_{REP} = 2$ V or 60 V, $V_{AGPS} = 7$ kV. The self-potential compensation as a function of time and y is shown in figure 5.22 at low pressure.
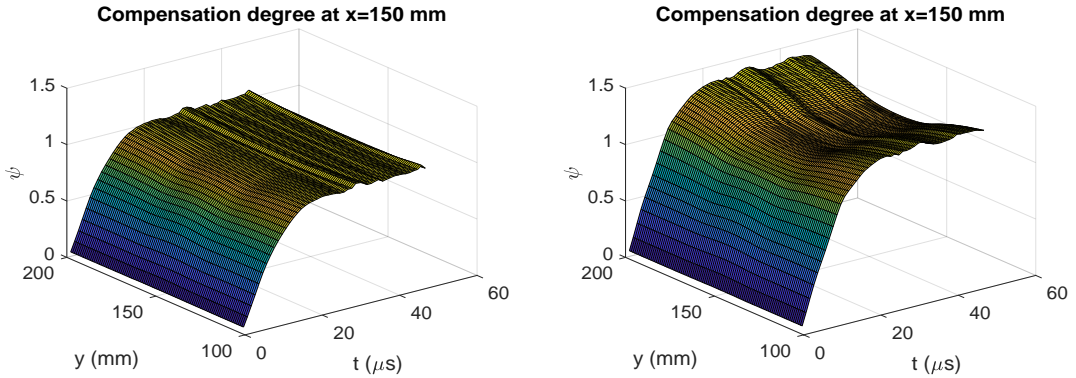
Figure 5.22: *The self-potential compensation as a function of time and y with $V_{CFC}=2$ V (left side) and $V_{CFC}=60$ V (right side).*

The self-potential compensation is estimated in the center of the drift tube. When the V_{CFC} is polarized, a higher degree of overcompensation in the correspondence of the central beamlets is present.

It is better shown by plotting ψ evolution as a function of time, as reported in figure 5.23 .
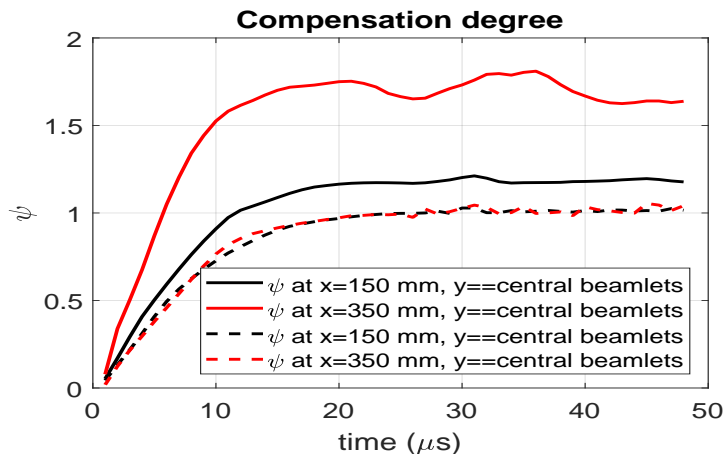
Figure 5.23: *The self-potential compensation as a function of time at two different y position with V_{CFC}=2 V (dashed line) and V_{CFC}=60 V (solid line) in the lower pressure regime.*

In figure 5.23 the self-potential compensation degree is shown for the two cases described and at two different position along the x direction. In both the cases shown, a higher ϕ is estimated when the CFC Tile and Repeller are polarized at the higher potential.

Emittance profile

As said in section 5.2.2, the emittance is a useful parameter which can be used to describe the quality of the beam. It is a measure for the average spread of particle coordinates in position-and-momentum phase space. In order to evaluate the average spread of the beam particles and of the ions produced by interaction with the background, different profiles of emittance are shown. In particular, the emittance of the H^- and H^0 are compared. The H^0 represents the final beam profile. The emittance shown in figure 5.24 is estimated at different time instants and at x=250 mm in the domain. In particular, the results shown refer to pressure vessel equals to 31 mPa and to an acceleration voltage equals to 2500 V.

The three results are shown at respectively time t=2.5, 5 and 50 μs. It can be noticed that the average spread of the neutrals along the central beamlets is lower than the in lateral two. After 50 μs, the spread in the central beamlet is almost zero and in the lateral two is clearly reduced. The upper and lower tails of the lateral two beamlets are due to the emittance profile expected when the beamlets exit from the accelerator. In fact, the radial profile is not expected to be uniform.
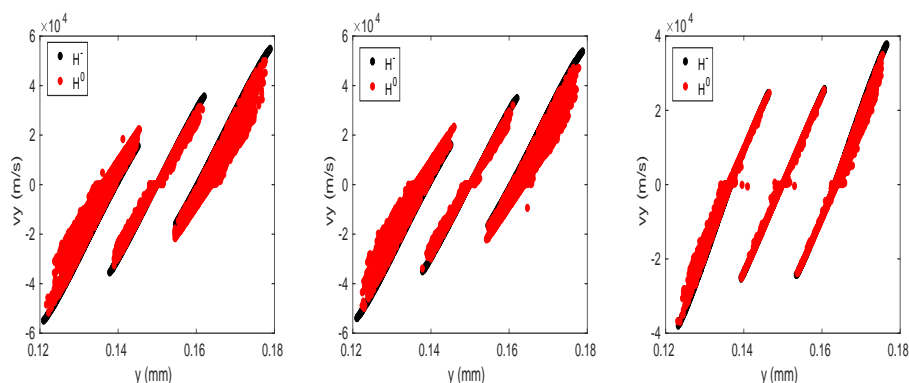
Figure 5.24: *Emittance profile at x=0.05 mm and at vessel pressure equals to 31 mPa at three different time (t=2.5, 5 and 50 μs).*

Hence, a major amount of particle with radial velocity lower or higher with respect the mean velocity is present. Since the intrinsic thermal velocity remains present in the beam at any distance from the source, this behavior is observed in the calculated emittance at any time.

Back streaming positive ions

It can be shown that the space charge compensation should be guaranteed within a short distance from the exit of the accelerator for ITER HNBs. Actually slight overcompensation is expected, as shown in the previous section in the case of V_{REP}= 60 V. This plasma might be severely affected by the fringe field of the accelerator column and a positive ion current towards the beam source could develop. For this reason, the Repeller is helpful in reducing these fringe fields and consequently in improving the space charge compensation level.

The quantity of positive ions entering in the GG at different vessel pressures and with or without the positive polarization of the Repeller are shown. The histograms show the velocity distribution of the positive ions created inside the domain, which have a negative velocity along the x direction high enough to enter in the GG. The velocity are shown with the reverse sign. The data compared have been simulated at different pressure and with V_{REP} equals to 2 and 60 V and with acceleration voltage equals to 7 kV.

As expected, the amount of positive ions entering in the PA increase when the V_{REP} is lower. A dependence with the pressure is also present. In table 5.4 are reported the density of current estimated for all the specie of positive ions at the different conditions shown in figure 5.25.
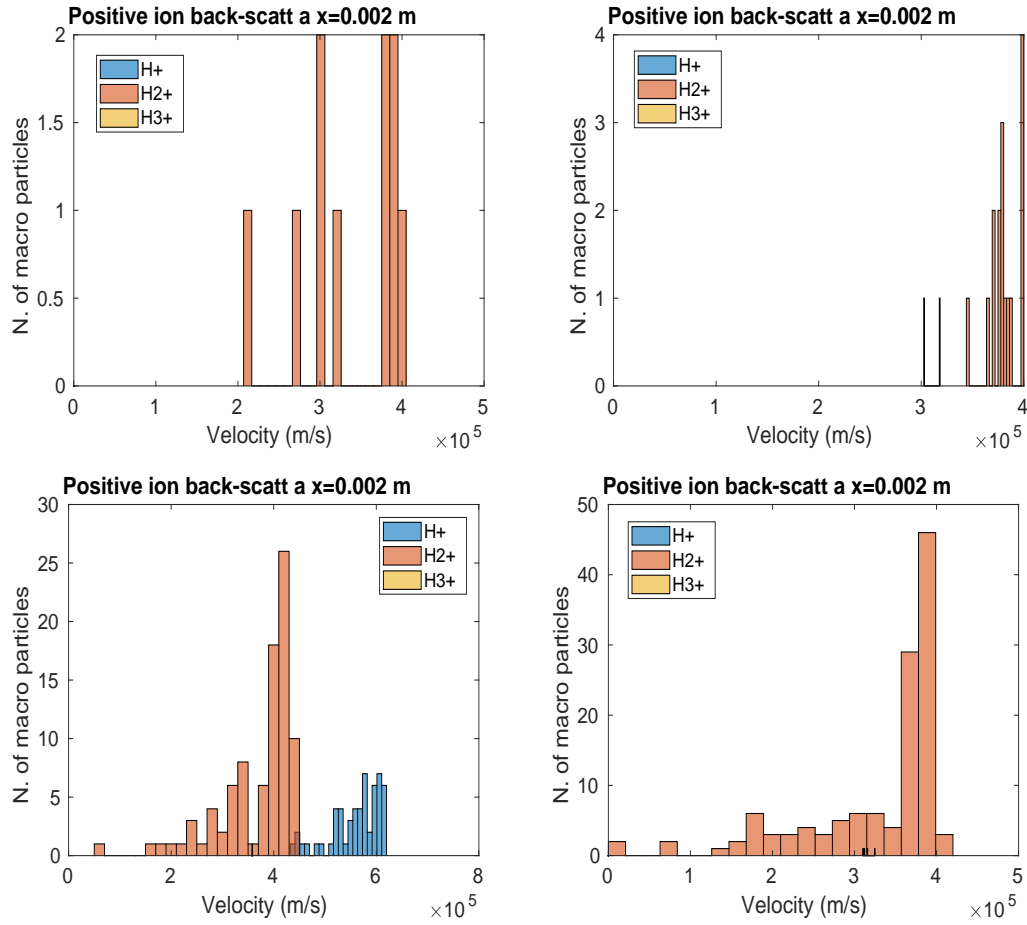
Figure 5.25: *Velocity distribution of positive ions back-scattered in the GG at V_{CFC}=60 V (left side) and V_{CFC}=2 V (right side) at two different pressures: P=31 mPa in the upper charts and P=500 mPa in the bottom charts.*

	$j_{H_2^+}$ (A/m^2)	$j_{H_3^+}$ (A/m^2) **(V)**	H_+ (A/m^2)
P=31 mPa, V_{CFC}=60 V	0.054	0	0
P=31 mPa, V_{CFC}=2 V	0.1	0.01	0
P=230 mPa, V_{CFC}=60 V	0.5	0	0.013
P=230 mPa, V_{CFC}=2 V	0.8	0.008	0.08

Table 5.4: *Comparison between the density of current measured at different conditions.*

Beam plasma density and potential profiles

The numerical simulation provides a complete characterization of the development of density and potential profiles. In particular, the dependence on the vessel pressure of the beam plasma can be seen. In figure 5.26 the horizontal and vertical profile of the densities of all the species in the regime of high pressure, namely 350 mPa, 3500 V of V_{AGPS} and 60 V applied on the CFC tile are reported.
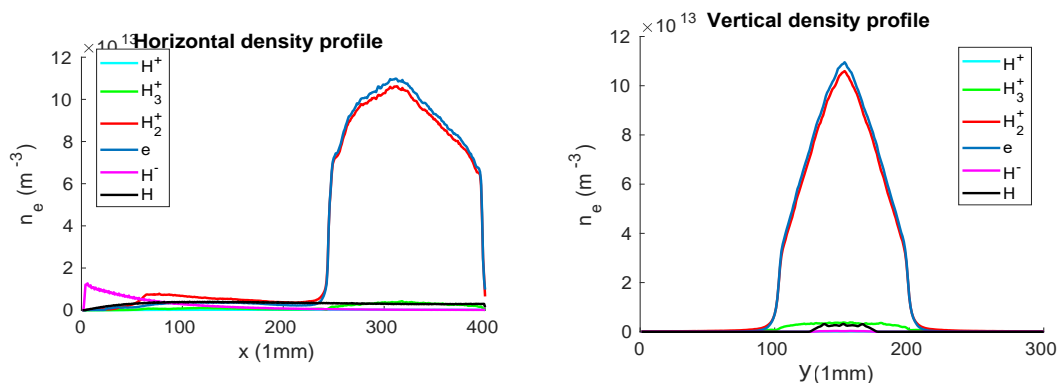
Figure 5.26: *Horizontal and vertical density profile of all the species simulated at high pressure. The horizontal profile is taken at y=150 mm (the position of the center beamlet) and the vertical one at x=305 mm.*

In the horizontal profile the presence of two different conditions is evident. Inside the drift tube, namely the first part of the domain, the beam plasma is some order of magnitude smaller with respect to the beam plasma formed in front of the CFC tile. There, the H_2^+ and electrons dominate on all the other species and they are present in almost the same amount. It is therefore visible the effect of the polarization of the CFC tile which attracts the electrons to the wall. Concerning the vertical profile instead, the beamlets are no more visible because of the beam plasma dominates. Totally different is the case with low pressure. The same profiles are shown in figure 5.27 with V_{CFC}=2 V.

The data refers to the optimum optics conditions, namely V_{AGPS}=2.5 kV, and the cryogenic pump are on. Here, the beam plasma is formed along the beamlets but they remain distinguishable. Also the beam plasma along the x direction described before is less prominent. The total density indeed is almost one order of magnitude lower with respect to the case at high pressure.

To summarize what has be seen before, the vertical and horizontal potential profiles as a function of the time will be compared for all the cases considered, namely at the two different values of vessel pressure and with two polarizations of the CFC tile. The vertical profiles are taken inside the drift tube (x=150 mm) and in the centre of the vessel (x=305 mm).
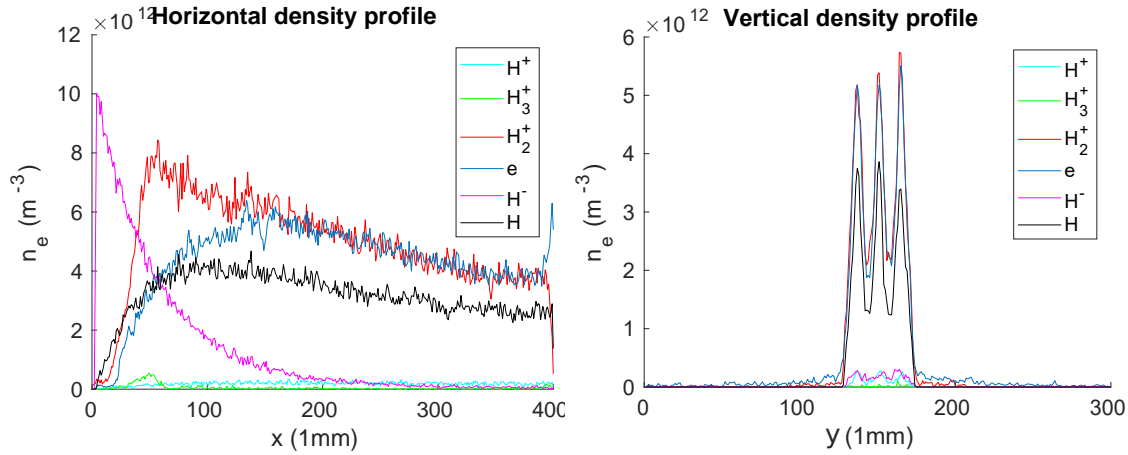
Figure 5.27: *Horizontal and vertical density profile of all the species simulated at low pressure. The horizontal profile is taken at y=150 mm (the position of the center beamlet) and the vertical one at x=225 mm.*

In figure 5.28 the vertical potential profile as a function of the time, taken at x=150 mm, are shown. When the pressure is low, the overcompensation is more difficult to achieve; in particular, only when the V_{CFC} voltage is high the potential inside the vessel becomes slightly positive.In the higher pressure range instead the potential profile becomes positive also when V_{CFC}=2 V.

In figure 5.29, the vertical density profiles taken in the same position inside the drift tube and at t=50 μs are shown. In particular, the effect of the optical correction applied to the beamlets (section 5.2.2) is clear. The first chart, referred to P=31 mPa and V_{CFC}=2, takes into account the thin lens correction while the others does not.

To conclude, in figure 5.30 the horizontal density profiles are shown. There, the amount of beam plasma formed when the beam propagates in the background gas is displayed. The same profiles are shown also at x=305 mm in figures 5.31 and 5.32.

.
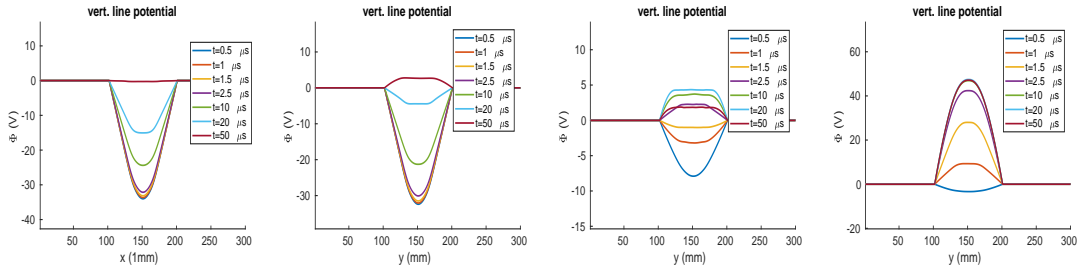
Figure 5.28: *Vertical potential profiles as a function of the time. In the order the data refers to: P=31 mPa, V_{CFC}=2 V; P=31 mPa, V_{CFC}=60 V; P=350 mPa, V_{CFC}=2 V; P=350 mPa, V_{CFC}=60 V. The data are taken at x=150 mm in the drift tube.*
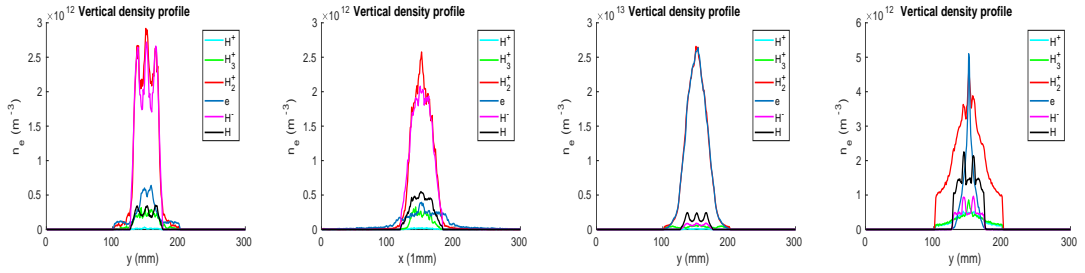
Figure 5.29: *Vertical density profiles taken at x=150 mm and t=50 μs. In the order, the data refers to: P=31 mPa, V_{CFC}=2 V; P=31 mPa, V_{CFC}=60 V; P=350 mPa, V_{CFC}=2 V; P=350 mPa, V_{CFC}=60 V.*
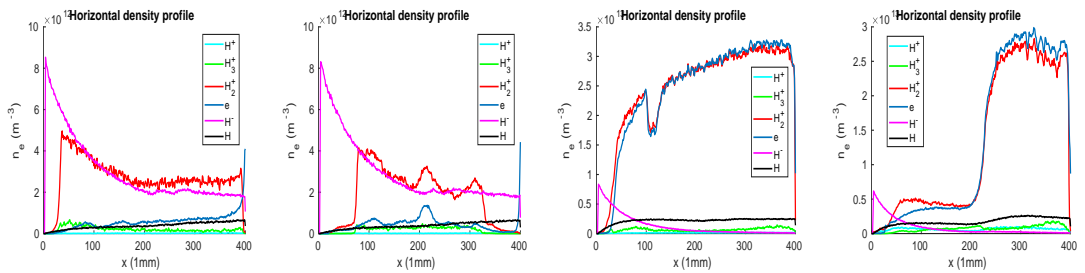
Figure 5.30: *Horizontal density profiles taken at y=150 mm and t=50 μs. In the order, the data refers to: P=31 mPa, V_{CFC}=2 V; P=31 mPa, V_{CFC}=60 V; P=350 mPa, V_{CFC}=2 V; P=350 mPa, V_{CFC}=60 V.*
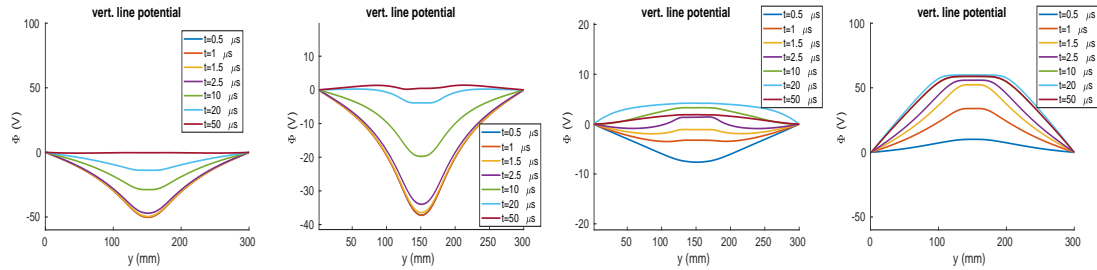
Figure 5.31: *Vertical potential profiles as a function of the time. In the order, the data refers in the order to: P=31 mPa, V_{CFC}=2 V; P=31 mPa, V_{CFC}=60 V; P=350 mPa, V_{CFC}=2 V; P=350 mPa, V_{CFC}=60 V. The profile are taken at x=305 mm in the drift tube.*
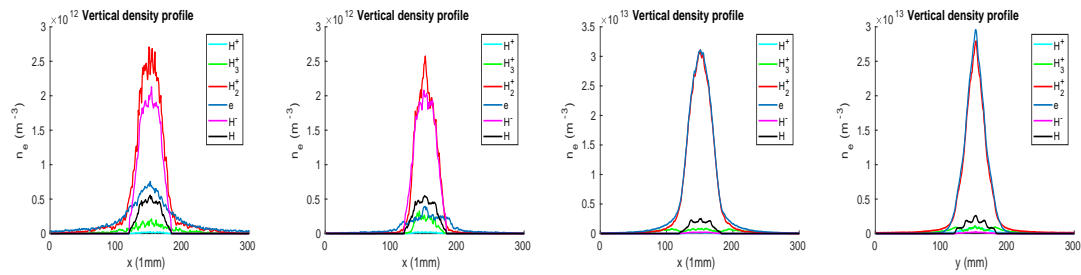
Figure 5.32: *Vertical density profiles taken at x=305 mm and t=50 μs. In the order, the data refers to: P=31 mPa, V_{CFC}=2 V; P=31 mPa, V_{CFC}=60 V; P=350 mPa, V_{CFC}=2 V; P=350 mPa, V_{CFC}=60 V.*

Conclusions

The research and the development of negative ion beam sources is nowadays one of the main fields of research, in view of the heating and the current drive of future nuclear fusion reactors.

In this work of thesis, a characterization complete as possible of the Negative Ion Beam NIO1 has been performed.

NIO1 is a small radio-frequency plasma driven source of negative ions. It was installed in 2013-2014 at Consorzio RFX, in collaboration with INFN (LNL). NIO1 target is the production of an extracted H^- beam of 130 mA, composed by 9 beamlets arranged in a 3x3 matrix and accelerated up to 60 keV by an electrostatic accelerator in the triode configuration.

In May 2017, a new Extraction Grid has been installed in order to improve the extracted beam. The modification involved the magnetic configuration and the radius of the extraction apertures. The investigation of the performance of this new configuration is the main topic of the present thesis.

Different diagnostics are available to characterize the NIO1 beam: Beam Emission Spectroscopy, two CMOS cameras, two electrostatic probes, a Retarding Field Analyzer and a LANGMUIR probe. In addition to these, more information is given from the current collected by the NIO1 grids and from the CFC tile, an invasive diagnostics on which the beam impinges.

A comprehensive description of the negative ion beam is given using the data collected by the BES, the currents measured on the various components and the images collected by the cameras.

From the measured currents, it is evident that the amount of co-extracted electrons is still high: the current impinging on the CFC tile, tightly related to the current carried by the beam, is more than one order of magnitude lower with respect to the EG current, due mainly to co-extracted electrons. Hence the magnetic configuration has to be investigated further in order to improve the NIO1 performance. With the present accelerator, an optimal optics value is identified by all the diagnostics. It corresponds to an acceleration voltage ranging between 2-3 kV and the extraction voltage ranging between 250-350 V.

The data collected by the cameras have been used to reconstruct by means of

computer tomography the beamlet configuration and evolution. By representing the 3x3 matrix of beamlets as 9 bi-dimensional Gaussians, the optimal parameters are estimated by minimizing the difference between the analytical reconstruction of the data and the experimental data themselves. With only two fans of lines-of-sight, a reliable reconstruction is difficult to achieve. Two different approaches have been studied and compared. The first approach leaves all the parameters of the minimization free while the second one uses one single width for all the beamlets.

The results are quite different. The first fit attributes always a bigger amplitude to the central beamlet, while the others are about one order of magnitude lower compared to the central one. The 3x3 matrix however remains visible and the symmetry of the apertures is respected. In the second approach instead the beamlet arrangement is less regular but all the beamlets are distinguishable and their intensities are comparable.

The reconstructions obtained from both the fit are then compared. In both cases the optimal optics value identified by the other diagnostic is confirmed; the displacement of the beamlets obtained was found in other accelerators, so it calls for further investigations.

Finally, a reconstruction of the beam plasma has been achieved by comparing the results measured from the two electrostatic probes and from a numerical simulation. The numerical simulation is a 2D-3V PIC-MCC model which includes the final part of the NIO1 accelerator column until the CFC tile. The main beam plasma parameters, such as electronic and ionic densities and temperatures, are obtained both from the two electrostatic probes and from the numerical simulation. Different configurations have been studied. The main parameters that have been changed and compared are the vessel pressure and the voltage of polarization of the CFC tile. Since the experimental data and the numerical simulation have shown a good agreement, the model has been used to further characterize the beam plasma.

To conclude, different results are obtained:

- The NIO1 diagnostic system is one of the more complete in the international scene of negative ion beam sources allowing a full characterization of the extracted beam.

- A complete beam reconstruction by means of computer tomography will be possible if an additional fan of lines-of-sight will be juxtapose to the present ones.

- The numerical code is able to correctly reproduce the property and the development of the beam plasma. It can be exploit in order to simulate the beam plasma in future new configurations of NIO1.

On the basis of the results obtained, the magnetic configuration of NIO1 will be changed shortly. Thanks to the complete diagnostic system any eventual change will be investigated and compared with the past configurations.

Furthermore, from the numerical simulation a quasi-complete beam compensation has be found even in the lower pressure range. A new cryogenic pump might be introduce to reduce further the vessel pressure, allowing NIO1 to range towards higher acceleration voltages.

Appendix A

Other scans

A.1 Scan in V_{AGPS}

Regarding a scan in V_{AGPS} with different pressure and without cryogenics, one can see in figure A.1 the measured currents. As shown before, the main difference is due to the change in the pressure. For the PA current, the amount of current measured increases appears proportionally to the pressure rising while for the CFC it is not. The CFC current measured from 0.45 Pa to 0.75 Pa is more than doubled, in a non-linear way with the pressure rising.

In figure A.2 some BES results are shown. The ratio between the stripping integral and the Doppler intensity with the increase in pressure rises because of the background growth. The beam divergence shows almost no dependence on pressure, with a minimum for V_{AGPS} close to 2.5 kV.
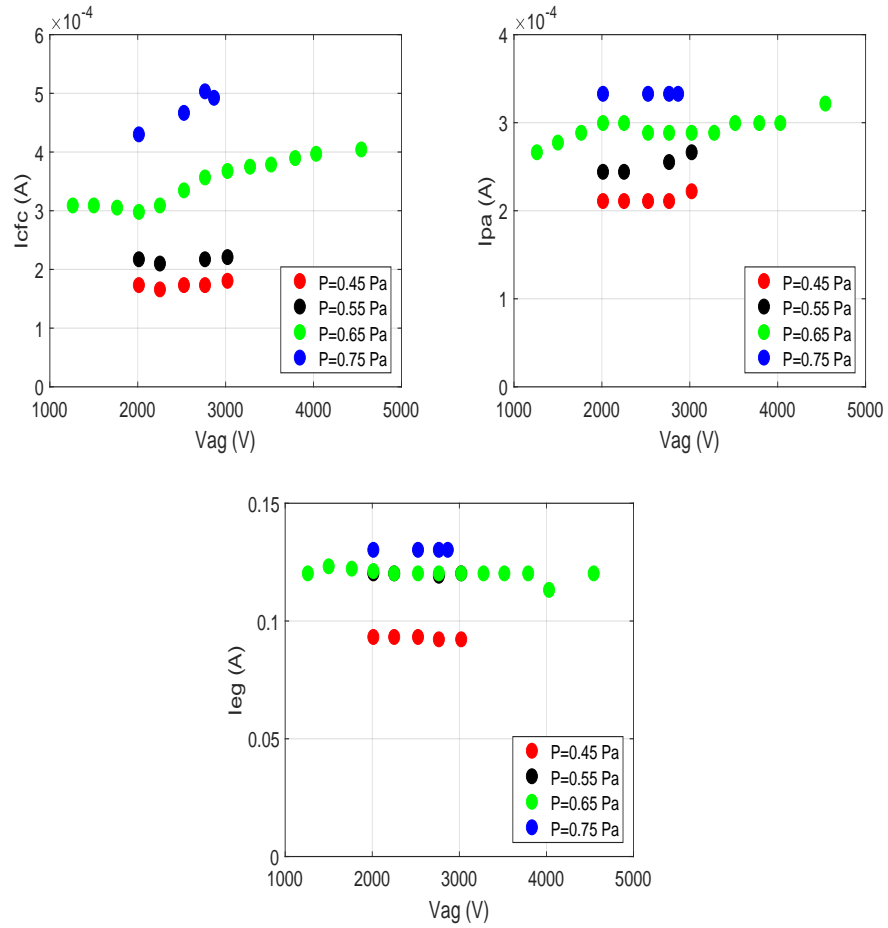
Figure A.1: *CFC, PA and EG currents as a function of V_{AGPS} for different pressure. The data refer to experimental day: 2017/09/28 with P=0.65 Pa and 2017/10/24 with P=0.45,0.55,0.75 Pa. All other parameters are fixed at V_{EGPS}=300 V, I_{PGF}=0 A, RF=1.2 kW, I_{BB}=0.2 A, Bias PG=45 V.*
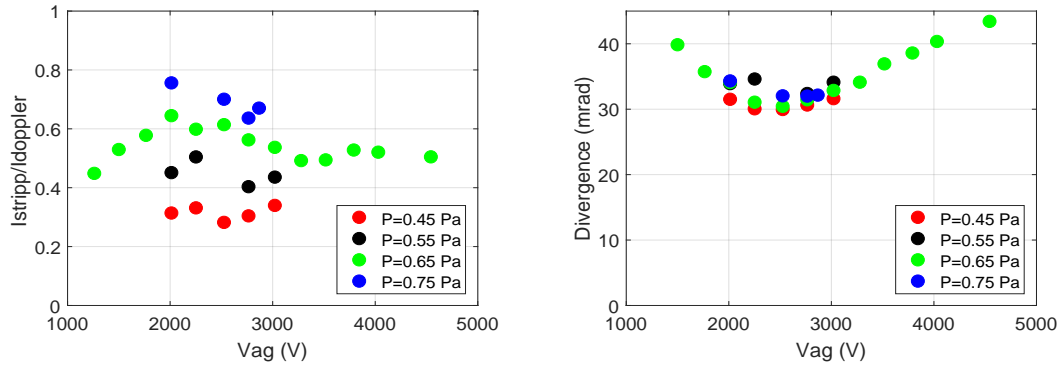
Figure A.2: $I_{STRIPP}/I_{DOPPLER}$ and beam divergence as a function of V_{AGPS} for different pressure. The data refer to experimental day: 2017/09/28 with P=0.65 Pa and 2017/10/24 with P=0.45,0.55,0.75 Pa. All other parameters are fixed at V_{EGPS}=300 V, I_{PGF}=0 A, RF=1.2 kW, I_{BB}=0.2 A, Bias PG=45 V.

A.2 Scan in V_{EGPS}

In figure A.3 the currents measured as functions of the extraction voltage are reported. The data were collected with different I_{BB} and bias plate voltage. This is the most probable reason of difference in the currents. It is more evident in the increasing EG current for data relative to the higher value of PG bias voltage. For all the currents the increase with V_{EGPS} is evident, as expected.

In figure A.4 it is evident the increase of the ratio between the integral of electron stripping and the intensity of Doppler peak with the increase of the extraction voltage when the cryogenics is off; the opposite happens when the cryogenic pumps are in use. On the other hand, the beam divergence decreases until a minimum value is obtained for V_{EGPS} near 700 V. Furthermore its independence from the effects of the cryogenics and from the Bias of the PG is shown.

Scans in extraction voltage at different acceleration voltages are considered in the following.

In figure A.5) the effect of the PG bias voltage appears more evident. The CFC current measured for the lower acceleration voltage (11/08 data with V_{AGPS}=2 kV) in fact is higher than the others, effect due to the higher bias voltage. As before, this effect is more evident in the CFC and EG currents and almost negligible for the PA current.

Concerning the BES results (Figure A.6), the difference in the ratio between the stripping integral and the Doppler peak intensity is obvious, due to the different acceleration voltage.
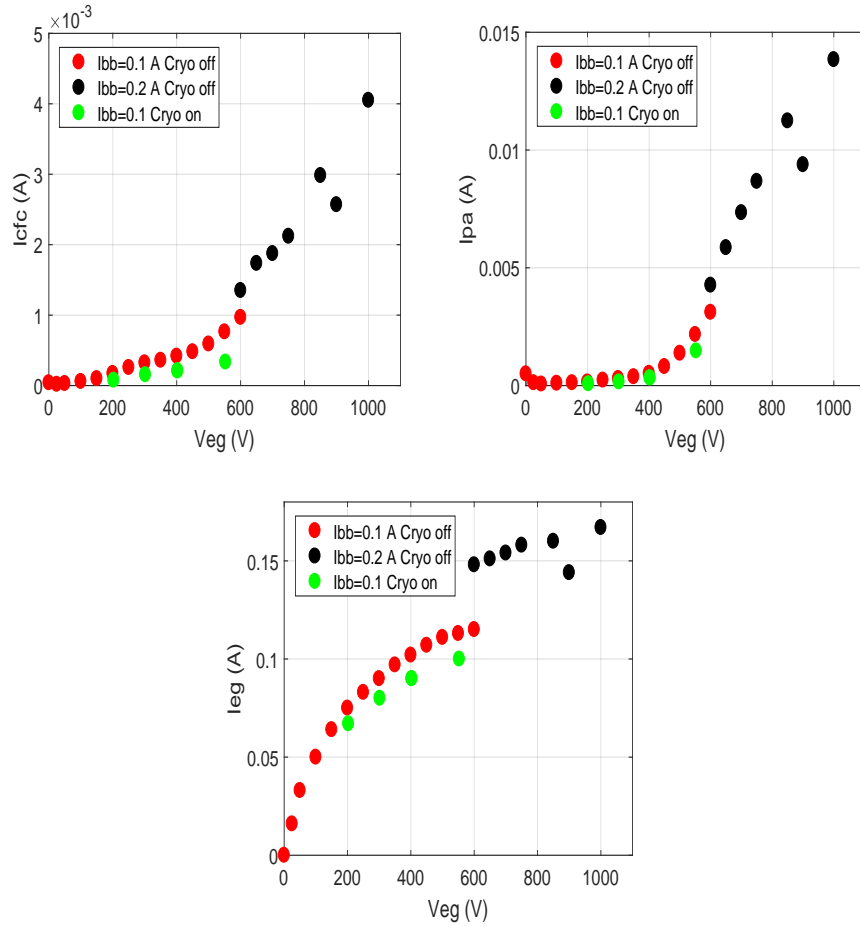
Figure A.3: *CFC, PA and EG currents as a function of V_{EGPS} with and without cryo. 2017/09/21 V_{AGPS}=6 kV, P=0.65 Pa, I_{PGF}=0 A, RF=1.2 kW, I_{BB}=0.1 A, Bias PG=20 V without cryo, Bias PG=-15 V with cryo on; 2017/09/26 V_{AGPS}=6 kV, P=0.65 Pa, I_{PGF}=0 A, RF=1.2 kW, I_{BB}=0.2 A, Bias PG=45 V, without cryo.*
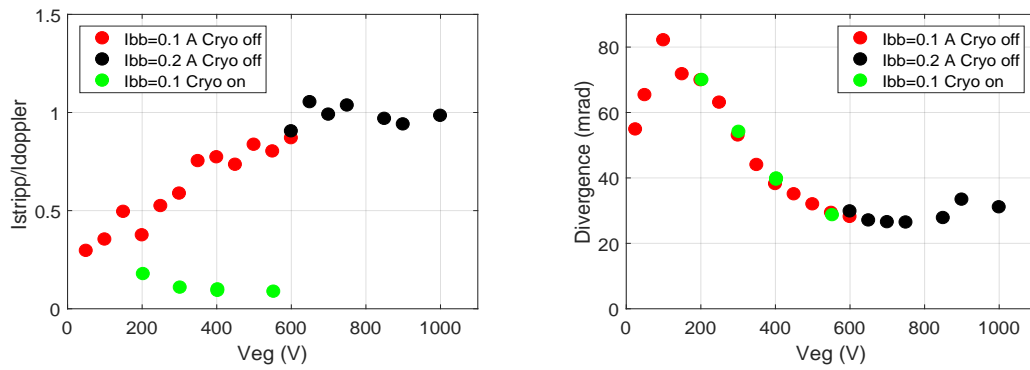
Figure A.4: $I_{STRIPP}/I_{DOPPLER}$ and beam divergence as a function of V_{EGPS} with and without cryo. 2017/09/21 V_{AGPS}=6 kV, P=0.65 Pa, I_{PGF}=0 A, RF=1.2 kW, I_{BB}=0.1 A, Bias PG=20 V without cryo, Bias PG=-15 V with cryo on; 2017/09/26 V_{AGPS}=6 kV, P=0.65 Pa, I_{PGF}=0 A, RF=1.2 kW, I_{BB}=0.2 A, Bias PG=45 V, without cryo.
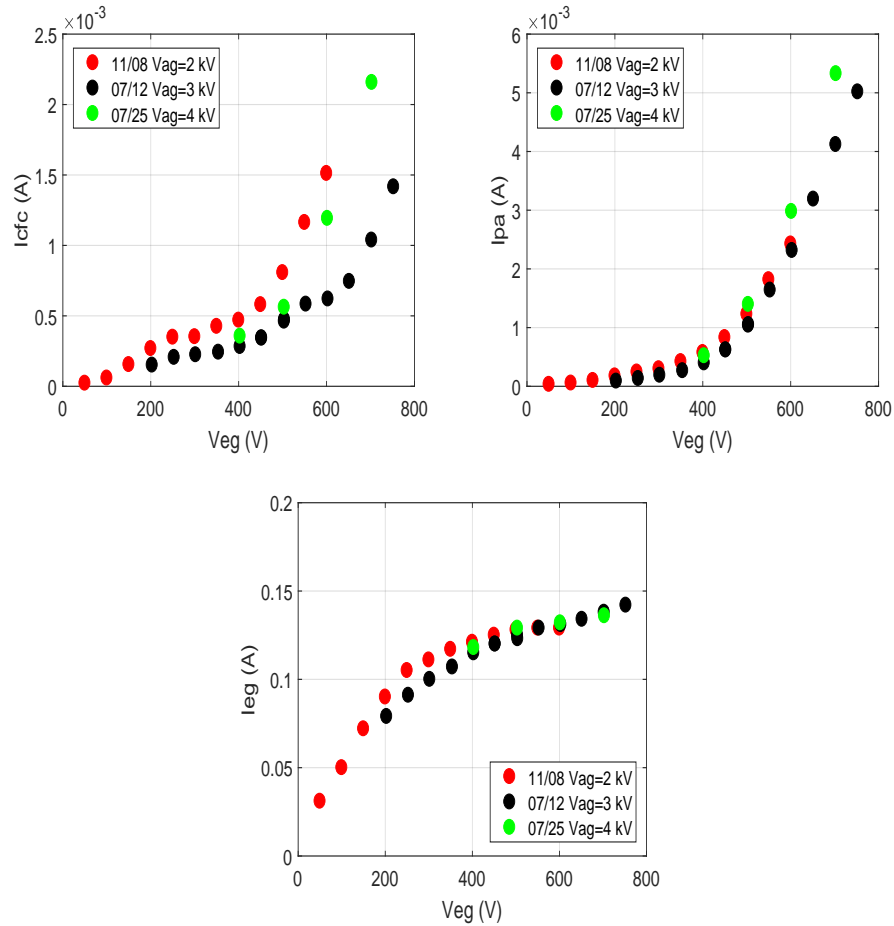
Figure A.5: *CFC, PA and EG currents as a function of V_{EGPS} with different V_{AGPS}. 2017/11/08 V_{AGPS}=2 kV, P=0.75 Pa, I_{PGF}=10 A, RF=1.1 kW, I_{BB}=0.1 A, Bias PG=45 V without cryo; 2017/07/12 V_{AGPS}=3 kV, P=0.65 Pa, I_{PGF}=200 A, RF=1.1 kW, I_{BB}=0.1 A, Bias PG=21.5 V, without cryo; 2017/07/25 V_{AGPS}=4 kV, P=0.75 Pa, I_{PGF}=10 A, RF=1.1 kW, I_{BB}=0.4 A, Bias PG=30 V without cryo.*
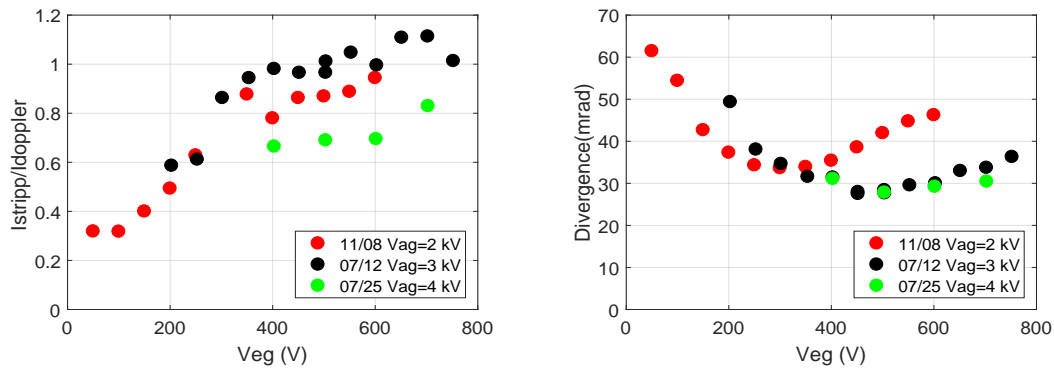
Figure A.6: $I_{STRIPP}/I_{DOPPLER}$ *and beam divergence as a function of* V_{EGPS} *with different* V_{AGPS}. *2017/11/08* V_{AGPS}=*2 kV, P=0.75 Pa,* I_{PGF}=*10 A, RF=1.1 kW,* I_{BB}=*0.1 A, Bias PG=45 V without cryo; 2017/07/12* V_{AGPS}=*3 kV, P=0.65 Pa,* I_{PGF}=*200 A, RF=1.1 kW,* I_{BB}=*0.1 A, Bias PG=21.5 V, without cryo; 2017/07/25* V_{AGPS}=*4 kV, P=0.75 Pa,* I_{PGF}=*10 A, RF=1.1 kW,* I_{BB}=*0.4 A, Bias PG=30 V without cryo.*

Bibliography

[1] E. Sartori *et al.* , *Simulation of space charge compensation in a multibeam-let negative ion beam*, Review of Scientific Instruments **87**, 02B917, doi: 10.1063/1.4933252 (2016).

[2] M. Spurio, *Particles and Astrophysics. A Multi-Messenger Approach*, Springer, DOI 10.1007/978-3-319-08051-2 (2014).

[3] R. Rhodes, *The Making of the Atomic Bomb*, New York: Simon & Schuster. ISBN 0-671-44133-7. OCLC 137943436 (1986).

[4] National Ignition Facility & Photon Science, Lawrence Livermore National Laboratory, https://lasers.llnl.gov/.

[5] ITER Organization, https://www.iter.org/.

[6] K.S. Krane, *Introductory Nuclear Physics*, John Wiley & Sons, 2nd Edition (1955).

[7] K.O. Hintermann and R. Wideröe, *Tritium Production and Cycling in a Fusion Reactor with Lithium Blanket*, A/CONF.15/P/1471, IAEA (1959).

[8] B.F. McMillan, *The physics of fusion power*, $https://warwick.ac.uk/fac/sci/physics//current/teach/module/$ $/home/px438/$ $lecture\_distributed\_2014.pdf$ (2014).

[9] S. Atzeni and J. Meyer-Ter-Vehn, *The Physics of Inertial Fusion* in International Series of Monographs on Physics, Clarendon Press-Oxford, ISBN: 9780198562641 (2004).

[10] D. Keefe, *Inertial Confinement Fusion*, Lawrence Berkeley National Laboratory, Annual Review of Nuclear and Particle Science, Vol. **32**, 391 (1982).

[11] J.D. Lawson, *Some Criteria for a Useful Thermonuclear Reactor*, A.E.R.E. report GP/R 1807 (1955).

[12] J. Mlynar, *Focus On: JET*, European Centre of Fusion Research, EFD-R(07)01 (2007).

[13] ITER Ita Newsletter, *International Atomic Energy Agency, Vienna, Austria*, ISSN 1727-9852 (2006).

[14] V.P. Smirnov, *Tokamak foundation in USSR/Russia 1950-1990*, IOP Publishing and International Atomic Energy Agency, Nucl. Fusion **50** 01 4003, doi:10.1088/0029-5515/50/1/014003 (2010).

[15] A.A. Harms *et al.*, *Principles of Fusion Energy. An Introduction to Fusion Energy for Students of Science and Engineering*, World Scientific Copyrighted Material, ISBN: 978-981-02-4335-7 (2000).

[16] R. Aymar *et al.*, *The ITER design*, Plasma Phys. Control Fusion **44** 519 (2002).

[17] J.P. Freidberg, *Plasma Physics and Fusion Energy*, Massachusetts Institute of Technology, Cambridge University Press, ISBN-13 978-0-511-27375-9, (2007).

[18] C. Gormenzano *et al.*, *Hybrid advanced scenarios: perspectives for ITER and new experiments with dominant RF heating*, Plasma Phys. Control Fusion **46** B435-B447 (2004).

[19] A.C. Riviere, *Penetrations of fast Hydrogen atoms into a fusion reactor plasma*, Nuclear Fusion **11** 363 (1971).

[20] M. Kikuchi *et al.*, *Fusion Physics*, International Atomic Energy Agency, Vienna, STI/PUB–1562; ISBN 978-92-0-130410-0, (2012).

[21] J. Maglica, *Plasma heating with neutral beam injection*, University of Ljubljana, Seminar (2005).

[22] D.C. Faircloth, *Negative Ion Sources: Magnetron and Penning*, Rutherford Appleton Laboratory, UK, https://arxiv.org/ftp/arxiv/papers/1404/1404.0944.pdf.

[23] R.S. Hemsworth, *Overview of the design od the ITER heating neutral beam injectors*, New J. Phys. **19** 025005, https://doi.org/10.1088/1367-2630/19/2/025005 (2017).

[24] U. Fantz *et al.*, *Negative ion RF sources for ITER NBI: status of the development and recent achievements*, Plasma Phys. Control Fusion **49** B563-B580, doi:10.1088/0741-3335/49/12B/S53 (2007).

[25] R. Pasqualotto *et al.*, *Progress on development of SPIDER diagnostics*, AIP Conference Proceedings **1869**, 030020, doi: 10.1063/1.4995740 (2017).

[26] P. Agostinetti *et al.*, *Detailed design optimization of the MITICA negative ion accelerator in view of the ITER NBI*, Nucl. Fusion **56** 016015, doi:10.1088/0029-5515/56/1/016015 (2016).

[27] I. Milch, *ELISE investigating from today new type of heating for ITER*, $https://www.ipp.mpg.de/ippcms/eng/presse/pi/14\_12\_pi$ (2012).

[28] M. Cavenago *et al.*, *Improvements of the versatile multiaperture negative ion source NIO1*, AIP Conference Proceedings **1869**, 030007, https://doi.org/10.1063/1.4995727 (2017).

[29] B. Zaniol *et al.*, *NIO1 diagnostics*, AIP Conference Proceedings **1655**, 060010, https://doi.org/10.1063/1.4916479 (2015).

[30] U. Fantz, *Atomic and molecular emission spectroscopy in low temperature plasmas containing hydrogen and deuterium*, (IPP 10/21), Max-Planck-Institut fÃ¼r Plasmaphysik, http://hdl.handle.net/11858/00-001M-0000-0027-4527-C (2002).

[31] D. Wunderlich *et al.*, *Application of a collisional radiative model to atomic Hydrogen for diagnostic purpose*, Journal of Quantitative Spectroscopy and Radiative Transfer, Vol **110**, https://doi.org/10.1016/j.jqsrt.2008.09.015 (2009).

[32] B. Zaniol *et al.*, *First Hydrogen operation of NIO1: Characterization of the source plasma by means of an optical emission spectroscopy diagnostic*, Review of Scientific Instruments **87**, 02B319, doi.org/10.1063/1.4936084 (2016).

[33] C. Baltador *et al.*, *Finite elements numerical codes as primary tool to improve beam optics in NIO1*, AIP Conference Proceedings **1869**, 030029, https://doi.org/10.1063/1.4995749 (2017).

[34] M. Barbisan *et al.*, *Modelling and design of a beam emission spectroscopy diagnostic for the negative ion source NIO1*, Review of Scientific Instruments **85**, 02A708, https://doi.org/10.1063/1.4826325 (2014).

[35] A. Pimazzoni *et al.*, *A first characterization of the NIO1 particle beam by means of diagnostic calorimeter*, AIP Conference Proceedings **1869**, 030028, https://doi.org/10.1063/1.4995748 (2017).

[36] B. Wolf, *Handbook of ion sources*, Edited by Bernhard Wolf, PH.D., GSI Center for Heavy Ion Research, CRC Press, Germany (1995).

[37] E. Sartori *et al.*, *Development of an energy analyzer as diagnostic of beam-generated plasma in negative ion beam systems*, AIP Conference Proceedings **1869**, 060005, https://doi.org/10.1063/1.4995792 (2017).

[38] F.F. Chen, *Introduction to plasma physics and controlled fusion*, Third Edition, Springer, ISBN 978-3-319-22308-7, DOI 10.1007/978-3-319-22309-4 (2015).

[39] G. Serianni *et al.*, *Negative Ion Sources: Concepts, Development, Testing and Optimization in NIO1*, Final report of deliverable activities on the NIO1 experiment, Eurofusion, HCD-3.2.1-T011-D011 (2016).

[40] G. Serianni *et al.*, *Acquisition, data retrieval, interlock and control systems for the negative ion source NIO1*, AIP Conference Proceedings **1869**, 060006, https://doi.org/10.1063/1.4995793 (2017).

[41] G. Manduchi *et al.*, *A new LabVIEW interface for MDSplus*, Fusion Engineering and Design, Vol **88**, https://doi.org/10.1016/j.fusengdes.2012.12.013 (2013).

[42] https://www.postgresql.org/docs/.

[43] I. Langmuir and K.T. Compton, *Electrical discharge in gases Part II. Fundamental phenomena in Electrical Discharges*, Review of Modern Physics, **3** (1931), https://doi.org/10.1103/RevModPhys.3.191 (2013).

[44] P. Veltri, *Ion beam transport: modelling and experimental measurements on a large negative ion source in view of the ITER heating neutral beam*, Nuclear Fusion **57** 016025, doi:10.1088/0029-5515/57/1/016025 (2017).

[45] G. A. Cottrel, *Doppler-shift emission tomography of intense neutral beams*, Journal of Physics, **15** 432, https://doi.org/10.1088/0022-3735/15/4/012 (1982).

[46] N. Fonnesu *et al.* , *Tomographic reconstruction of the beam emissivity profile in the negative ion source NIO1*, Nuclear Fusion, **56** 126018, doi:10.1088/0029-5515/56/12/126018 (2016).

[47] I.A. Soloshenko *et al.*, *Space charge compensation of technological ion beams*, IEEE Transactions on Plasma Scienze, V. 27 **4**, 10.1109/27.782288 (1999).

[48] G. Chitarin *et al.*, *Cancellation of the ion deflection due to electron-suppression magnetic field in a negative-ion accelerator*, Review of Scientific Instruments, V. 85 **2** 02B317 (2014).

[49] J. P. Boris, *Proceedings of the 4th Conference on Numerical Simulation of Plasmas*, Naval Research Laboratory, Washington, pp 3-67 (1970).

[50] K. Koura, *Null-collision technique in the direct-simulation Monte Carlo method*, Physics of Fluids **29**,https://doi.org/10.1063/1.865826 (1986).

[51] C. F. Barnett *et al.*, *Atomic data for fusion*, The ORNL Redbooks, http://www-cfadc.phy.ornl.gov/redbooks/one/1.html.

[52] N. Bell and M. Garland, *Generic Parallel algorithms for Spare Matrix and Graph Computations*, http://cusp-library.googlecode.com (2012).

[53] M. Reiser, *Theory and Design of Charged Particle Beams*, Second Edition, WILEY-VCH, ISBN: 978-3-527-40741-5 (2008).

Ringraziamenti

Doverosi sono i ringraziamenti alla fine di questo percorso di tesi.

Senza dubbio, un ringraziamento va al professor Bruno, il quale ha preso a cuore la mia richiesta di voler fare una tesi sulla fusione nucleare e mi ha aiutato a far si che ciò fosse possibile. Naturalmente, un grande ringraziamento va anche a tutte le persone che ho conosciuto al Consorzio RFX e che mi hanno accolto fin da subito. Al Dr. Serianni, che mi ha guidata fin dall'inizio e mi ha insegnato veramente qualsiasi cosa. Al Dr. Cavenago, il quale ha condiviso con me le peripezie burocratiche per far si che questa tesi diventasse realtà. Ai Dr. Veltri, Barbisan, Agostini e Sartori che mi hanno supportato (e sopportato) nel completamento di questa tesi. E infine i doverosi ringraziamenti a Bologna e all'infinita vita che mi ha dato. A chi mi è stato vicino da casa e a chi l'ha vissuta con me. E si, un grazie va anche a Valerio che mi ha aiutato a sopravvivere in questi anni.